COSMIC RAY OBSERVATIONS AT HIGH ZENITH ANGLES

by

A. Vrana, B.Elec.Eng. (Zurich)

submitted in fulfilment of the

requirements for the degree of

Master of Science

UNIVERSITY OF TASMANIA

HOBART

July 1976

This thesis contains no material which has been accepted for the award of any degree or diploma in any university.

To the best of my knowledge and belief, the thesis contains no material previously published or written by another person except where due reference is made in the text.

A. Vrana

CONTENTS

PREFACE

The thesis is the description of the design and construction of a high zenith angle telescope for the Mawson observatory, together with some discussion of results obtained. Because the new Mawson observatory installed in 1972 is a logical extension complementing the high zenith angle experiment, it was felt that inclusion of a brief description of the new observatory complex would not be out of place.

I joined the Australian National Antarctic Research Expedition in 1964 as an expedition physicist. During my stay at Mawson in 1965 I became aware of the shortcomings of mains operated electronic equipment at remote stations and designed some battery operated solid state circuits to replace the former circuitry. Upon my return from Mawson I was commissioned to finalise the design of the transistorised circuitry and develop modular circuit units for the use with counter telescopes.

In 1966 a joint project was proposed by the Antarctic Division and the University of Tasmania for a high zenith angle ground based experiment. Given the basic requirements for the desired geometry I was to undertake the design, construction and installation of the new telescopes at Mawson. During the course of the work I realized that for a successful design an understanding of the principles of cosmic ray recording was necessary. Whilst the design of the experiment rested primarily on Dr. R.M. Jacklyn, I undertook the initial investigation of the air shower component influencing the observed intensity under the guidance of Dr. A.G. Fenton and Dr. R.M. Jacklyn.

I sailed for Mawson in early 1968 to install and supervise the performance of the new telescope during the first year of operation. After my return to Hobart I carried out further tests regarding the air shower component as described in sec. 3.4, based on the original idea of Mr. G.C. Cooper, the Mawson physicist in 1969.

In 1970 the Antarctic Division undertook to establish an underground observatory based on the proposal of Dr. R.M. Jacklyn. The design of the experiment originated from Dr. R.M. Jacklyn based on the detailed calculations of asymptotic directions by Dr. D.J. Cooke and I had the responsibility of the design and construction of the detectors, electronic circuitry, specification of the new observatory building and selection of the site for the observatory. In late 1971 I again sailed for Mawson to supervise the installation of the new observatory and initiate the operation of the equipment.

The thesis is also aimed to give assistance to the operator of the observatory in the maintenance of the equipment; therefore the function of some of the electronics are described in more detail than otherwise might seem necessary. Although some of the electronic circuits appear to be cumbersome and unnecessarily complicated at today's standard of component development, at the time of design they represented the optimum in cost, complexity and component availability.

ACKNOWLEDGEMENTS

The completion of the present project necessarily involved many people and depended on the co-operation of several organisations.

The supervision and constant interest of Dr. A.G. Fenton throughout this work is gratefully acknowledged. Special thanks are due to Dr. R.M. Jacklyn whose contributions, support and encouragement made the project possible.

Many helpful discussions relating to the present work have been held with the members of the Physics Department of this University. Dr. D.J. Cooke supplied the computer programs for the radiation sensitivity calculation, the coupling coefficient function and the asymptotic direction of viewing of the telescopes. Harmonic analysis and the four-fold regression analysis has been carried out using the computer program of Dr. J.E. Humble.

The race against time for the completion of the equipment for shipment to Mawson put pressure on many people involved. Mr. G. Wagner and Mr. D. Harding of the Physics Department workshop constructed all telescope frameworks. Mr. D.E. Millwood designed and constructed the crystal oscillator for the chronometer circuit. Mrs. L. Jackson and Miss K. Haynes assembled most of the printed circuit boards, Mr. M. Mason constructed the large number of counters required.

The construction of the new observatory had been carried out most enthusiastically by the members of the 1971 and 1972 Mawson expeditions. The expedition physicists responsible for the maintenance of the observatory since 1968 were Mr. G.C. Cooper,

Mr. D.D. Parer, Mr. R.A. Buckland, Mr. A.D. Bennet, Mr. W. Butler and Mr. H. Nissink, who all contributed to the improvement of the observatory. Mr. D.D. Parer was actively involved in the construction of the underground telescopes and was second in charge of the installation work in 1972.

The staff of the Antarctic Division fully co-operated in the logistic organisation of the project. Detailed design of the new observatory was the responsibility of the Senior Engineer Mr. A. Brown and the technical officers Mr. G. Smith and Mr. W. Young.

The co-operation of all these people is greatly appreciated.

I acknowledge the continuing support of my employers, the Antarctic Division of the Department of Science, under whose auspices this research work is being conducted.

Finally, I wish to thank Mrs. L. Harbeck for the typing of this thesis and Hilary for her moral support.

CHAPTER 1

COSMIC RAY OBSERVATIONS AT MAWSON

1.1 Introduction

Cosmic ray observations at Mawson, Antarctica (geographic co-ordinates $67^{\circ}36'$ S, $62^{\circ}53'$ E, geomagnetic co-ordinates 73° S, 103° E) commenced in 1955 with the installation of two muon telescopes of cubical geometry recommended for the IGY network of cosmic ray recording stations throughout the world. The primary research objective of the experiment was the solar diurnal variation, the verification of the east-west asymmetry at high latitudes e.g. above the latitude knee, the study of the atmospheric effects on secondary cosmic rays at polar latitudes and experimental confirmation of theoretical studies of the range of muons in air as a function of momentum as manifested in the E/W asymmetry.

For this purpose two rotatable inclined cubical telescopes of (1x 1)x 1.5m geometry were installed and the muon flux from the two directions east and west were continuously recorded.

An important part of the IGY cosmic ray program was the elucidation of the sun's influence on the cosmic ray intensity. A 12 counter-pile neutron monitor was installed in 1957 to study the nucleonic component of the cosmic radiation. As neutron monitors respond mainly to the low energy primary proton flux, they are the most suitable instruments to study solar related phenomena such as Forbush-decrease, solar flare proton events, etc.

Because of incomplete knowledge of the influence of both the geomagnetic field and the atmospheric variation on the observed cosmic ray flux, study of the primary cosmic ray flux outside

the geomagnetic field could only be undertaken effectively with an extended network of recording stations operating over a long time. The cosmic ray observatory at Mawson was to become one of the worldwide network of recording stations.

Due to the small size and associated poor statistical resolution of early cosmic ray detectors it was not clear that there were anisotropies in the cosmic ray flux beyond the magnetosphere and atmospheric influence. The improved countrate of the IGY detectors, the establishment of a world-wide network of recording stations and proper understanding of atmospheric effects and the influence of the geomagnetic field resulted in the recognition of daily periodicities in the primary cosmic ray flux. The availability of cosmic ray data from detectors at diverse geographic locations and computerized data analysis enabled the establishment of the asymptotic cone of response of any particular detector in relation to the energy spectrum observed. Analysis of observed periodicities of the primary cosmic ray flux thus has become possible.

A major aspect of the study of the cosmic ray intensity variation concerns the solar diurnal variation. It has been found that after eliminating the meteorological contributions to the solar daily variation a net variation in the cosmic ray flux results due to a directional anisotropy of the primary radiation approaching the earth's magnetic field region. Similarly, intensity variations with respect to a fixed direction in space may be due to anisotropies of extraplanetary or galactic origin.

The purpose of the present work was to design a cosmic ray

telescope installation for the experimental study of anisotropies and by virtue of its location enable the separation of the various components of the solar and sidereal daily variation, and secondly, to establish the direction and magnitude of the sidereal anisotropy.

1.2 Anisotropies

In general, studies of cosmic ray intensity variations are carried out with detectors set at a fixed direction. Both temporal and spatial intensity variations are recorded as variations of the detected flux with time, the latter being the result of the relative motion of the detector to the chosen reference.

Typical temporal intensity variations are atmospheric effects whereby the secondary cosmic ray intensity is modulated by the time-varying effects of atmospheric pressure, temperature, etc.

Spatial intensity variations are referred to as anisotropies. Different types of anisotropies can be investigated by appropriate selection of time intervals and searches for any periodicity in that time interval. For anisotropic flux no periodicity exists for any time interval.

In the investigation of the solar anisotropy the time interval is one solar day. At any two times 24 hours apart the detector will have the same relative direction to the sun.

The solar anisotropy will give rise to a combination of diurnal and semi-diurnal intensity variations depending on the asymptotic viewing of the detector and the type of modulating mechanism. The orbital movement of the detector around the sun in the isotropic

cosmic ray gas will indicate an intensity maximum in the direction of the orbital movement, referred to as a Compton-Getting effect (Compton 1935). In a further instance of the Compton-Getting effect, the bulk motion of the cosmic ray gas caused by the azimuthal co-rotation of the interplanetary magnetic field with the sun will cause an intensity maximum to be observed in the direction of the local magnetic field, the magnitude of the co-rotation itself being subject to modification by transverse diffusion and gradient currents (Parker 1964). The model for the solar magnetic field suggested by Parker (1958) is represented by an Archimedes spiral in the sun's equatorial plane. For an estimated solar wind velocity of 400 km/s and heliocentric distance of 1 AU the resulting free space diurnal anisotropy is 90° east of the earth-sun line and the amplitude of the anisotropy is of the order of 0.5%.

Interpretations of the early measurements of the solar diurnal anisotropy suffered from the lack of knowledge of the accurate direction and field strength of the solar magnetic field. It was generally found that the solar diurnal variation had a time of maximum and amplitude in accordance with the model of the steady state solar magnetic field. Large departures, however, in both the phase and amplitude have been observed from time to time. The discovery of the sector structure of the interplanetary magnetic field based on space-probe data necessitated the modification of existing modulation theories.

The concept of the diurnal anisotropy as a resultant vector of the radial convection of C.R. particles in the outward

direction from the sun and inward diffusion along the magnetic field lines as proposed by McCracken et al. (1968) has been theoretically formulated by Forman and Gleeson (1970). In the case of equilibrium between radial convection and field aligned diffusion a co-rotational diurnal vector results. Imbalance caused by the fluctuation of the interplanetary parameters such as the solar wind and the magnetic field can result in large day to day variations of the diurnal variation (Rao et al. 1972).

A further possible cause for solar anisotropy is the uneven distribution of primaries with small pitch angles guided along the interplanetary magnetic field. These particles will be scattered by magnetic irregularities close to the sun giving an excess of particles with steep pitch angles in the vicinity of the earth. As a result, a maximum intensity will be observed in the direction perpendicular to the direction of the IMF. The pitch-angle anisotropy will be observed as a combination of the diurnal and semi-diurnal component of the solar daily variation.

It can be said that all proposed explanations of the solar daily variation, some of which are briefly mentioned above, are open to further discussion. The exact nature of the solar anisotropy is not clear yet. Further studies, both experimental and theoretical, will be necessary to establish a satisfactory model for the modulating process of the cosmic ray flux in the interplanetary magnetic field.

If the cosmic ray data are analysed in sidereal time, any periodicity observed will indicate an apparent intensity change with respect to a fixed direction in the celestial frame of

reference or an apparent sidereal anisotropy. Several possible sources for such an anisotropy have been predicted. For instance, an excess of particles with small pitch angles due to trapping of the flux between constrictions in the galactic magnetic field as proposed by Davis (1954) would result in an observed first and second harmonics of the sidereal daily variation of the charged primary particle flux.

Early cosmic ray measurements indicated a very small degree of apparent sidereal anisotropy (Elliott and Dolbear 1951, Simpson and Conforto 1957). The difficulty in observing the sidereal anisotropy at sea level is due to the presence of the solar daily variation and additional atmospheric contributions. Improved counting statistics and the establishment of underground observatories with high threshold energies in more recent years have partly overcome the difficulties encountered by early experimenters.

Experimental results over a number of years from the Hobart underground detectors indicated an apparent sidereal anisotropy (Jacklyn 1965, 1966). Together with underground observations in the northern hemisphere the following conclusions have been reached regarding the nature of the sidereal anisotropy (Jacklyn 1970):

i. existence of a bi-directional sidereal anisotropy with symmetrical intensity maxima in opposite directions,

ii. a superimposed uni-directional component,

iii. the approximate south pointing direction of the observed anisotropy is RA $\approx$ 0600, dec. $\approx 35^{o}$.

CHAPTER 2

THE SIDEREAL ANISOTROPY

2.1 Terrestrial Reference of the Anisotropy

On the basis of observational evidence from underground detectors a simple empirical model has been devised to describe the essential features of an intensity anisotropy observed at a given point O in space in the direction OP (Jacklyn 1970). The direction OP makes an angle β with the plane normal to the axis of the unequal and oppositely directed intensity maxima of primaries of rigidity R. The differential intensity in the direction OP is then given by

$$I_{R,\beta} = I_{oR} \{ 1 + R^{\gamma}(m \sin\beta + n(\sin^2\beta - 1/3))\} \quad (2\text{-}1)$$

where I_{oR} is the isotropic flux and γ the index of the variation spectrum of the anisotropy. m and n are amplitude constants. Referred to the celestial system the direction OP is specified by declination δ and Right Ascension Φ':

$$\sin\beta = \cos d \cos\delta \cos(\Phi' - \alpha_s) + \sin d \sin\delta \quad (2\text{-}2)$$

where α_s is the Right Ascension of the intensity maximum and d its declination.

The intensity anisotropy therefore can be written in the general form

$$I_R + I_{oR}(1 + T(\Phi') + T(\delta)) \quad (2\text{-}3)$$

I_{oR} represents the average intensity term, $I_{oR}T(\Phi')$ the daily variation term and $I_{oR}T(\delta)$ is the latitude dependent daily average term.

The daily average term can be written as the sum of harmonic

components. The first and second harmonics for given rigidity R are:

$$V_{1R} = R^{\gamma}(m + 2n \sin d \sin\delta) \cos d \cos\delta \cos(\Phi'-\alpha_s) \qquad (2\text{-}3)$$

and $$V_{2R} = R^{\gamma} \frac{n}{2} \cos^2 d \cos^2\delta \cos 2(\Phi'-\alpha_s) \qquad (2\text{-}4)$$

2-3 and 2-4 are the differential free space harmonics. The total free space harmonics are obtained by integrating the differential free space harmonics between the energy range of the upper and lower cut-off rigidity R_c and R_m of the observation of the anisotropy. We have:

$$V_1 = \kappa_c M \cos(\Phi'-\alpha_s) \qquad (2\text{-}5)$$

$$V_2 = \kappa_c N \cos 2(\Phi'-\alpha_s) \qquad (2\text{-}6)$$

In the expressions above κ_c is the rigidity dependent amplitude response constant, M and N are rigidity independent free space constants. It should be noted, that any change in the cut-off rigidity such as caused by solar activity will modify the amplitude constant κ_c even if the anisotropy is not of solar origin.

So far all considerations have taken place under the assumption of free space conditions. To calculate the expected daily variation observed at the telescope the deflecting influence of the terrestrial magnetic field on charged primary particles, the influence of the atmosphere and the coupling between the primary and secondary particles must be taken into account. The asymptotic constants of response will take these factors into consideration. The expression for the first and second free space harmonics will then be modified to the form:

$$v_1 = K_1 M \cos(\Phi'-\alpha_s+\Phi_1) \qquad (2\text{-}7)$$

$$v_2 = K_2 N \cos 2(\Phi'-\alpha_s+\Phi_2) \qquad (2\text{-}8)$$

The aymptotic constants K_1 K_2 Φ_1 and Φ_2 contain the influence of the terrestrial magnetic field, the atmosphere and the coupling coefficient on the free space harmonics. By replacing δ with $\overline{\delta}$, the mean asymptotic latitude of response in the rigidity independent terms M and N, the above equations represent the observed harmonics. It is assumed, that both harmonics have the same mean asymptotic latitude of viewing $\overline{\delta}$.

To obtain useful information about anisotropies from any given detector, the response constants K_1 K_2 Φ_1 Φ_2 κ_c and $\overline{\delta}$ of the detector must be established. The method of calculation of response constants is fully described by Jacklyn (1970). The response constants of any given detector are a function of the detector's geometry, geographic location, directionof viewing and the amount of absorber used as well as the threshold rigidity of the observed primaries R_c.

In full knowledge of the response constants of the detectors it is possible to estimate the direction of the sidereal anisotropy in free space in terms of declination d and Right Ascension α_s on the basis of observed data.

The declination can be calculated as a function of threshold rigidity R_c and the index of the variation spectrum γ from annual averaged observations of two detectors located at the same depth. To test for spurious components in the sidereal anisotropy a third detector scanning a different latitude strip is employed.

The expression for.the declination in terms of the observed harmonics at detectors A and B for the symmetrical bidirectional component is:

$$\tan d = \frac{\frac{K_{2A}\cos^2\delta_A}{K_{1B}\cos^2\delta_B} v_{1Bmax} - \frac{K_{2A}}{K_{1A}}\cos\delta_A\, v_{1Amax}}{4v_{2Amax}(\sin\delta_B - \sin\delta_A)} \qquad (2\text{-}9)$$

The estimated declination calculated using two underground detectors, one in the northern hemisphere and one in the southern hemisphere for spectral index $\gamma = 0$ gives $d = 37.6 \pm 7^{\circ}$.

The Right Ascension of the anisotropy is calculated from the time of maximum of the sidereal daily variation and the phase displacements Φ_1 and Φ_2 of the diurnal and semi-diurnal components respectively. For threshold rigidities over 100 GeV and $\gamma = 0$ the estimated RA in the southern hemisphere is found to be approx. 0640 $\pm$ 0115 hours. The corresponding galactic co-ordinates are $l^{II} = 245^{\circ}$, $b^{II} = -15^{\circ}$.

In his analytical treatment of three-dimensional cosmic ray anisotropy Nagashima (1971) presents a general formulation of the daily variation produced by axis-symmetric anisotropies. The variational intensity distribution observed from a direction JO with polar co-ordinates χ and Λ and rigidity P is expressed as the superposition of axis-symmetric distributions

$$\delta J(P,\chi,\Lambda)/J(P) = \sum_{k=1}^{\infty} F(\chi_k)^k G(P)^k \qquad (2\text{-}10)$$

where G(P) is the rigidity spectrum normalized to unity at the rigidity P_o and $F(\chi)$ is called the space distribution.

The space distribution $F(\chi)$ can be expanded into a series of Legendre function

$$F(\chi) = \sum_{n=o}^{\infty} \eta_n P_n^o(\cos\chi) \qquad (2\text{-}11)$$

Co-efficient η_n is the magnitude of the n-th space distribution. It is important to note that the reference axis of the anisotropy OR ($\chi=0$) is not necessarily the direction of the anisotropy, in certain cases the distribution has its maxima in a plane perpendicular to the reference axis.

The space distribution is transformed into the equatorial co-ordinate system as

$$F(\chi) = \sum_{n=o}^{\infty} F_n(\chi) = \sum_{n=o}^{\infty} \{ \sum_{m=o}^{\infty} f_n^m(\chi)\} \qquad (2\text{-}12)$$

where $$f_n^m(\chi) = \eta P_n^m(\cos\Theta_R)\ P_n^m(\cos\Theta_J)\cos m(\alpha_J-\alpha_R) \qquad (2\text{-}13)$$

in which α_R and Θ_R are the Right Ascension and co-declination of the reference axis, α_J and Θ_J are those of the direction JO.

Function f_n^m is the projected component of the space distribution $F(\chi)$. In considering a sidereal anisotropy stationary throughout the year, the magnitude η_n and the direction of the reference axis Θ_R, α_R of the space distribution should be constant. The projected component is the representation of the sidereal anisotropy. For the solar anisotropy however, the direction of the reference axis is specified by the ecliptic longitude and co-latitude of the reference axis and the ecliptic longitude of the sun.

2.2 The Origin of the Sidereal Anisotropy

Since the discovery of the cosmic ray intensity variation in sidereal time much effort has been devoted to find a satisfactory explanation of the observed anisotropy. Some of the early theories have been briefly mentioned in Chapter 1. In more recent years on the basis of further observational evidence several theo-

ries have been put forward to explain the apparent sidereal anisotropy as a direct result of solar related phenomena and the influence of the interplanetary magnetic field, thus casting doubts on the existence of a genuine sidereal anisotropy of galactic origin. In the following a short examination is undertaken of the several proposed modulating models which can give rise to an observed sidereal anisotropy.

It is common to express the daily variation of the cosmic ray intensity in terms of its harmonic components. The solar diurnal variation is regarded as a carrier wave with a frequency of 365 cycles per year. In analogy with the modulation theory of radio waves any superimposed variation of amplitude for example will appear as a modulation of the carrier frequency responsible for the production of sidebands symmetrically displaced in amplitude and frequency around the carrier frequency. The annual variation of the amplitude of the solar diurnal variation therefore will result in symmetrical sidebands with frequencies of 364 and 366 cycles per year, the annual modulation of the SDV will appear as an apparent sidereal variation (Farley and Storey, 1954). The anti-sidereal technique should enable us to distinguish between the spurious sideband and the genuine sidereal component by simple combination of the solar, sidereal and anti-sidereal diurnal variations. However, the anti-sidereal vector will not necessarily indicate a seasonal modulation of the solar component (Jacklyn 1962, Nagashima 1972).

In the absence of an anti-sidereal component the sidereal component can be regarded as unrelated to the solar variation by

seasonal modulation of amplitude. The same consideration will apply to semi-annual variation of amplitude with sidebands at 368 cycles/year and 364 cycles/year.

In his treatment of the effect of radial heliocentric cosmic ray density on the observed flux Swinson (1969) proposes a model producing an apparent sidereal variation in the vicinity of the earth. In the proposed model a spurious sidereal anisotropy will be produced as a result of the alternating IMF's effect on the heliocentric density gradient. The outward pointing magnetic field (90^{o} east of the earth-sun line) acting upon the cosmic ray flux with a density increasing with distance from the sun will result a net upward flux perpendicular to the ecliptic plane. The inward pointing magnetic field will have the reversed effect. A detector rotating with the earth will look at a given time during the day closest to the direction perpendicular to the plane of ecliptic and hence record a maximum or minimum intensity as the case may be. The similtaneous 12 hours phase difference between the northern and southern hemisphere intensity maximum is explained by the weakening of the IMF outside the earth's orbit, i.e. the gyro-radius of particles of the same energy arriving from the anti-sun direction will be greater.

Although some observational evidence supports the theory of field dependent anisotropies, space probe experiments, such as Pioneer 10 (Van Allen, 1973) failed to observe a radial density gradient of significant magnitude. Furthermore, the model does not account for the presence of the consistently observed second harmonic of the observed sidereal daily variation. Data

collected from a number of stations in recent years are in disagreement with the model based on the radial density gradient for the production of apparent sidereal anisotropy (Castagnoli 1973, Humble et al. 1973). Although observational evidence does not entirely exclude the possibility of a density gradient type of anisotropy, it is more likely that some other phenomena such as those mentioned in chapter 1 are responsible for at least the anisotropy observed at higher energies. Swinson (1971) estimates the upper cut-off rigidity of the radial gradient anisotropy in the vicinity of 75 GV. Observations at higher energies, however, still exhibit a residual sidereal vector (Fenton et al. 1975, Nagashima et al. 1975).

A similar effect to the radial gradient anisotropy will be the vector sum of the co-rotational flux and the anisotropy due to the perpendicular gradient, its direction again dependent on the direction of the IMF (Swinson, 1971), but will always be in the plane of the ecliptic. The resultant anisotropy is a solar anisotropy, and if a seasonal modulation of any of the parameters takes place a solar sideband effect will occur giving rise to a possible spurious sidereal variation as discussed earlier.

Extensive analysis of the space distribution theory by Nagashima et al. (1972) proves the possibility of an observed sidereal vector without corresponding anti-sidereal vector as a result of annual modulation of the solar anisotropy during the active period of the solar cycle. Experimental evidence appears to support the predominance of a pitch-angle type of anisotropy, such as the "loss cone" model described by Sarabhai et al. (1965)

over the density gradient hypothesis. For the quiet solar period, however, the annual modulation of the pitch-angle type of anisotropy cannot explain the existence of the still observed sidereal variations.

A further remarkable result reported more recently by Castagnoli (1975) is the phase change of the sidereal diurnal vector in the northern hemisphere, apparently concurrent with the reversal of the polar field of the sun. Similar phase change has not been observed in the southern hemisphere. No satisfactory explanation has been found to date for this phenomenon.

Although the present survey is most incomplete, the number of contradictions and the conflicting nature of experimental evidences are clear. An alternative way to obtain more information about the origin of the anisotropies is to learn more about the energy dependence of the observed variations. Such an experimental proposal will be discussed in the next section.

2.3 Purpose of the High Zenith Angle Experiment

Despite the large amount of work expended in the field the origin of the apparent sidereal anisotropy still remains unclear. To help to decide whether the observed anisotropies are of galactic, interplanetary or solar origin, an experiment has been proposed for Mawson using high zenith angle detectors. The aim was to observe the cosmic ray intensity variation in two opposing azimuth directions, e.g. north and south. The north pointing detector would scan equatorially; the south pointing would be directed at mid-latitudes but in the conjugate longitude across the south pole. Based on the comparison of the observed sidereal diurnal variation

together with the associated anti-sidereal component, conclusions could be reached regarding the nature of the apparent sidereal anisotropies. In a simplified manner the expected results can be summarized as follows:

Both the north and south sidereal diurnal vectors in the same phase and the presence of an anti-sidereal vector of equal amplitude would indicate an atmospheric seasonal modulation of the cosmic ray flux. The two vectors in opposite phase and the absence of the anti-sidereal vector would infer a genuine high energy sidereal variation of galactic origin. Out of phase north and south vectors combined with an anti-sidereal vector would result from seasonal modulation of the solar anisotropy. Finally the above case could occur if a low energy (interplanetary origin) genuine sidereal anisotropy is responsible for the modulation. The energy range through which the anisotropy is effective could be deduced from the phase angles of the two vectors. For very high energies the vectors will be of opposite phase, the telescopes looking asymptotically in the opposite longitude; for lower energies the asymptotic direction of viewing will be correspondingly modified reducing the phase angle between the two vectors.

It is expected that more than one phenomena will be observed simultaneously. The semi-diurnal component will then make identification possible under certain circumstances. The relation of the phase angle of the semi-diurnal component to that of the diurnal vector will enable the estimation of parameters decisive to the nature of the anisotropies.

Time variation of the phase and amplitude of the observed

sidereal vectors over a number of years, particularly in relation to the time variation of the solar daily variation, will yield information about the energy region through which solar modulation of the cosmic ray flux occurs.

CHAPTER 3

THE HIGH ZENITH ANGLE EXPERIMENT AT MAWSON

3.1 Geometry of the High Zenith Angle Telescope

In search for further evidence of the two-way and the unidirectional sidereal anisotropies it was essential to establish a high energy sea level muon detector array with suitable directional sensitivity to obtain quantitative information on the directions, amplitudes and energy dependences of the anisotropies. Optimal use has been made of the directional properties of geiger counter telescopes. The properties of the proposed muon detectors follow from the considerations regarding the particular experiment, i.e. the direction and angular resolution of the telescope should be such as to give the maximum response to the anisotropy under investigation and the mean energy of response should be comparable to that of the Hobart underground vertical telescope system. The latter has been achieved by recording at high zenith angles, thus using the earth's atmosphere as an effective shield to filter out a large portion of low energy mesons subject to solar modulation. The recorder should be as far as practicable free of the disturbing influence of air showers, both local and high energy ones originating in nuclear collisions in the atmosphere. Furthermore, it is necessary to be able to distinguish between intensity variations due to atmospheric origin and the genuine sidereal effect. Seasonal modulation of the daily variation of atmospheric conditions including, for instance, the height of the mean muon production layer will affect the daily variation of the total intensity recorded at sea level. If data are analysed in sidereal time, unwanted sideband

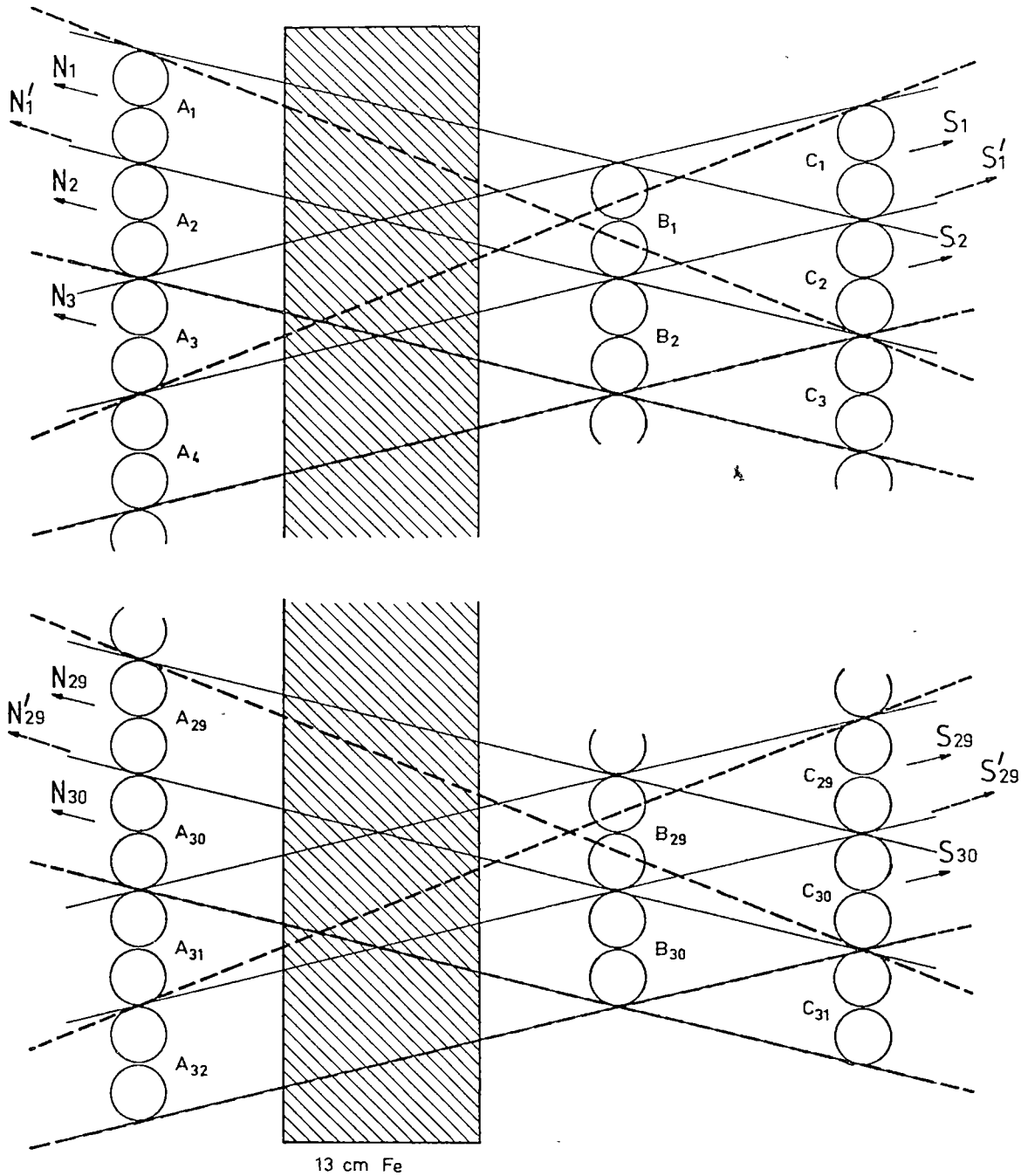

FIG 3-1 GEOMETRY OF THE HIGH ZENITH ANGLE TELESCOPE. NARROW ANGLE AND WIDE ANGLE CONFIGURATION.

effects will result.

Following considerations outlined above a compound telescope has been designed consisting of three walls of conventional geiger counters of dimensions 1m x 4cm. Suitable gating of the output pulses of the geiger counters provides a telescope element geometry of (1m x 0.08m) x 0.5m with a zenith angle of 76.5°(fig.3-1). The output pulses of all sub-units are added together electronically before being recorded as NORTH and SOUTH coincidences respectively, the mean azimuth directions being geographic north and south.

The principle of operation of the high zenith angle telescope is similar to the conventional cubical muon telescope. There is however a vital difference which will be mentioned here.

The telescope will record the muon intensity from two opposite azimuth direction at the same zenith angle simultaneously, i.e. the effective use of the geiger counters is doubled. Each direction of azimuth viewing supplies relevant information about different properties of the anisotropy. The north pointing part of the telescope looks equatorially, giving maximum response to the semidiurnal component of the bidirectional anisotropy, also maximum response in the diurnal component of the unidirectional anisotropy. The south pointing telescope on the other hand should respond primarily to the diurnal component of the bidirectional anisotropy. In addition, the south pointing telescope, looking transverse to the terrestrial magnetic field where deflection of charged particles is greatest, carries valuable information relating to the energy range of the anisotropy.

A further advantage of the conjugate azimuth geometry is the possibility of elimination of spurious atmospheric effects. It has been shown (Jacklyn 1970) that seasonal modulation of the daily atmospheric temperature variation can cause an apparent sidereal intensity variation if data are analysed for a full year period. On the assumption that both azimuth directions of the telescope will be equally affected, the common modulating effect can be easily determined by finding the vector common to both azimuth directions.

Another important property of the telescope is the relatively high energy of response achieved by its high zenith angle of viewing. In the given configuration the mean (geometric) zenith angle of each telescope element is 76.5^{o}. The total air mass in the direction of viewing can be calculated by integrating the air density over the path of the incoming cosmic ray particle. If the total air mass in the vertical direction in given by

$$m_o = \int_{r_o}^{\infty} \rho(r-r_e)dr \qquad (3\text{-}1)$$

where $\rho(r - r_e)$ gives the atmospheric density at radius r and r_e is the radius of the earth

then the air mass seen from any given level r_o at zenith angle θ will be

$$m = \int_{r_o}^{\infty} \frac{\rho(r-r_e)r\,dr}{(r^2-r_o^2\sin^2\theta)^{\frac{1}{2}}} \qquad (3\text{-}2)$$

Assuming for ρ the function

$$\rho = \rho_o \exp\{-\alpha(r-r_e)\} \qquad (3\text{-}3)$$

where $\alpha = 0.12$ for r and r_e in kilometres for the earth atmosphere, and making the substitution $\delta = r - r_e$

then the ratio of the vertical to oblique air mass will be

$$m/m_o = 0.12(r_o/2)^{\frac{1}{2}} \int_o^\infty \frac{e^{-0.12\delta}\, d\delta}{\{(r_o/2)\cos^2\theta+\delta\}^{\frac{1}{2}}} \qquad (3\text{-}4)$$

Equation 3-4 takes into account the curvature of the earth's surface. Tabulated values of 3-4 are given by Winckler et al.(1949) For zenith angle $\theta = 76.5^o$ the ratio m/m_o is equal 4.25. Therefore the effective air mass in the viewing direction of the telescope will be 41.7 metres water equivalent (m.w.e.). The total absorber used in the Hobart underground experiment is 45 m.w.e. The cut-off energies of the telescopes at the two stations are similar, thus the observations should be intercomparable.

The desired statistical accuracy ($\sim$20000 par/hr) requires a minimum number of sub-units of 90. Three full scale telescopes, each consisting of 30 sub-units, had been constructed for the total high zenith angle installation at Mawson. The count ratios of the three telescopes give a day to day indication of the efficiency of each telescope unit.

3.2 Prototype Telescope Experiment at Hobart

Prior to the construction of the full scale high zenith angle telescope units a prototype telescope was built in Hobart. The purpose of the trial experiment was threefold, e.g. to test the transistorized electronic circuitry, to gain an experimental value of the expected countrate with and without absorber material placed between counter trays and to devise a method of eliminating harmful air shower effects present in the total countrate.

The air shower component of the measured countrate originates from the following sources:

a) local air showers produced within or in the immediate vicinity of the detector, e.g. in the local absorber or in nearby objects,

b) air showers of atmospheric origin resulting from nuclear interactions, consisting of both hard and soft components (electron showers), whose parent-particle direction of incidence is outside the cone of acceptance of the telescope, and

c) the narrow based air showers or jets commonly accompanying genuine high zenith angle particles.

Clearly, the type c) air showers represent a valuable and acceptable part of the true high zenith angle particle flux and the rejection of the air shower event would unduly reduce the narrow angle countrate.

The experimental setup for the investigation of type b) shower events consisted of three converted set C counter trays set vertically and containing 10 narrow angle sub-units. Initially a $1m^2$ guard tray was placed on top of the telescope, the output of which was connected in anticoincidence with the NORTH output. This configuration effectively rejected all NORTH coincidences occuring simultaneously with vertically incident particles. The SOUTH output recorded all relevant threefold coincidences, including events caused by vertical air showers. In this configuration, both geometries being equal, the S-N difference represents the vertical air shower component recorded as apparent high zenith angle coincidence. The observed difference in the S-N countrate was found to be 8.3% of the SOUTH countrate.

Several methods were investigated in an attempt to eliminate

the vertical air shower component from the total countrate without the use of the guard tray. This was desirable on account of counter economy and simplified electronic circuitry.

It appears to be a reasonable assumption that each vertical or near vertical air shower event will cause a discharge in several counters in each of the vertical trays. Vertical displacement of the centre tray counter pairs will have negligible effect on the coincidence rate caused by air showers. Genuine high zenith angle muons, on the other hand, will not be recorded if the displacement is such, that no straight line can be drawn through the three counter pair in coincidence. This arrangement has been realized through suitable gating of the output pulses. The coincidence configuration for the air shower recording will be then:

$$N_{\text{air shower}} = A_1 \cdot B_2 \cdot C_2 + A_2 \cdot B_3 \cdot C_3 + \cdots \qquad \text{(c.f. fig.3-1)}$$

The measured 3-fold coincidence rate for the given out-of-line configuration was 12% of the in-line countrate, and the rate of the common events between the guard tray and the out-of-line coincidence obtained via a further coincidence gate yielded 7% of the NORTH countrate. Comparing the above result with the S-N difference of 8.3% obtained from the guard tray experiment it is apparent that the out-of-line method of air shower rejection will identify approximately 80% of the vertical air shower events coinciding with the arrival of true high zenith angle particles and therefore is a feasible proposition as an air shower detecting system. The remaining 5% difference in the out-of-line coincidence and its coincidence with the guard tray is attributed to inclined air showers of zenithal distribution outside the shielding influence

of the guard tray above the telescope.

A further possible method of air shower rejection consists of the recording of the coincidences between the NORTH and SOUTH coincidence events. The measured rate was 3.25% of the NORTH coincidence and the coincidence rate between the N-S coincidence and guard tray was 2.5%. The N-S coincidence method is thus less effective than the out-of-line method for air shower detection.

In the light of these experiments it has been cautiously concluded that the out-of-line coincidence method will give some indication of the air shower component of the measured threefold high zenith angle countrate. Independent recording and analysis of the out-of-line coincidences will enable us to relate the diurnal variation and atmospheric effects of the air shower component to that of the genuine high zenith angle muons.

In the above experiments the accidental coincidence rate of statistical origin has been discounted. It will be shown in Ch. [illegible] (Parsons, 1957) that in the given circuit configuration the accidental [illegible] rate is of the order of 0.01% and therefore can be neglected in the present discussion.

Owing to the OR-gating of the individual sub-unit coincidence pulses (ref. Ch.5) vertical stacking of sub-units of the compound telescope will reduce the air shower to high zenith angle count ratio and therefore enhances the efficiency of the telescope in recording high zenith angle particles. An air shower event will be recorded as a single coincidence event only, irrespective of the number of sub-units recording simultaneous coincidence pulses. To illustrate the case the total count rate will be considered

consisting of the sum of the genuine high zenith angle count rate and the count rate due to air showers. The accidental count rate due to background radiation of the counters and the concurrent high zenith angle and air shower events will again be disregarded.

The angular distribution of air showers has been studied experimentally by several workers (e.g. Kraybill (1954), Bassi et al. (1953)). It was found that the zenith angle dependence of air showers can be approximated to a power of $\cos\theta$. The exponent will be a function of both the integral density spectrum and the geometry of the detector. A value of 8.5 for the exponent gives a good agreement with the zenith angle distribution curve for extensive air showers at sea level given by Sandström (1965) and will be used here.

For the purpose of considering shower events the uppermost sub-unit of the telescope can be regarded as an uniformly sensitive horizontal area of length l corresponding to the length of the counter and width d representing the extreme counter separation.

The total countrate of the compound telescope will be

$$N'_{tot} = n.N_h + m_n.N_{as} \qquad (3\text{-}5)$$

where n is the number of sub-units, N_h and N_{as} are the high zenith angle and air shower count rates of a single sub-unit respectively. m_n is the ratio of the compound telescope to single sub-unit air shower rate, i.e.

$$m_n = \frac{N'_{tot} - nN_h}{N_{tot} - N_h} \qquad (3\text{-}6)$$

The total air shower component detected by the telescope is the sum of shower events $N_{as\ vert}$ recorded by the uppermost sub-unit

and the air showers incident on the vertical surface of the telescope $N_{as\ incl}$. The ratio m_n will be then

$$m_n = \frac{N_{as\ vert} + N_{as\ incl}}{N_{as\ vert}} = 1 + \frac{N_{as\ incl}}{N_{as\ vert}} = 1 + \frac{h\,l \int_0^{\pi/2} \cos^{8.5}\theta \sin\theta\, d\theta}{d\,l \int_0^{\pi/2} \cos^{8.5}\theta \cos\theta\, d\theta}$$

or $$m_n = 1 + 0.2658\ h/d \qquad (3\text{-}7)$$

where h is the height of the vertical counter wall, i.e. for a compound telescope consisting of 30 sub-units h = 240 cm.

For the given geometry of the high zenith angle telescope for a 30-fold increase of the high zenith angle count-rate the air shower rate will increase by a factor of 2.43 only.

Since the soft component of the sea-level cosmic radiation is largely unrelated to the high energy muons, it is desirable to eliminate it from the total count rate of the muon telescope by introducing local absorber between any two trays of geiger counters. In the prototype telescope 10 cm of lead between the vertical counter trays A and B reduced the 3-fold coincidence count rate by 27%. For reasons of economy and mechanical stability the use of lead absorber for the high zenith angle telescope proved to be impractical. A total absorber material of 13 cm of steel, the approximate equivalent of 10 cm of lead, has been placed between the vertical counter trays A and B in the full scale telescope.

Introduction of absorber material between counter trays will produce cascade showers of type a).

Charged particles traversing matter lose energy by collision

and radiation. Low energy electrons and heavy nuclei passing through an appreciable amount of matter, e.g. lead or steel absorber plate of a muon telescope, will dissipate their energy in exciting atoms or ejecting further low energy electrons from the atoms and will thus be dissipated within the absorber. Electrons of high energy originating from the decay of negative muons, ionisation processes or other nuclear interactions on the other hand will dissipate their energy mostly by producing high energy photons. The photons, in turn, will produce Compton electrons or materialize into electron-position pairs. As the process continues a cascade shower is developed.

When successive interactions in the absorber medium reduce the electrons kinetic energy to the critical energy E_c, the electron will lose as much energy by ionisation as by radiation and will come to rest without further photon emission. E_c is a characteristic of the absorbing medium. Calculated values for iron and lead are $E_{cFe} = 20.7$ MeV and $E_{cPb} = 7.4$ MeV respectively. The minimum energy of electrons capable of producing showers is greater for iron than for lead, therefore the effective number of shower producing particles is correspondingly smaller.

The distance X_0 covered by an electron while emitting one photon is given by the relation

$$\frac{1}{X_0} = \frac{4}{137}\frac{N}{A}\left\{\frac{Ze^2}{m_o c^2}\right\}^2 \ln\frac{183}{Z^{1/3}} \qquad (3\text{-}8)$$

where Z is the atomic number of the absorbing medium, N/A the number of atoms per unit mass and mc^2 the rest energy of the electron. The radiation length is expressed in g/cm^2. Radiation lengths

for iron and lead are $X_{oFe} = 13.9$ g/cm^2 abd $X_{oPb} = 6.4$ g/cm^2. 13 cm of iron absorber represents therefore 7.34 radiation lengths.

The number of cascade showers as a function of the absorber thickness has been measured using different absorber materials (e.g. Rossi (1933)). The obtained plot is referred to as the transition curve. Characteristically, the initial part of the transition curve shows a rapid increase in the number of showers with increasing absorber thickness. For iron or lead a maximum value is reached at a thickness of some 2 to 3 radiation lengths. Further increase of the absorber thickness will gradually reduce the number of showers until an asymptotic value is reached, presumably caused by penetrating muon showers. The exact shape of the transition curve is a function of the geometric arrangement of the detectors, the spectrum of the incident radiation and the absorber material.

The observed coincidence count-rate of the high zenith angle telescope will include coincidence events due to cascade showers. Unlike extensive air showers with large longitudinal spread and small cone, cascade showers will be localized but will extend over a large solid angle. Some 3-fold coincidence events therefore will be caused by particles arriving outside the acceptance angle of the absorber material initiated by the same parent particle. Calculation of the shower contribution to the coincidence count rate would be rather difficult due to the number of parameters involved. An experiment, however, has been carried out to demonstrate the presence of cascade showers. For this purpose the coincidence circuit of the telescope has been modified as follows:

The individual pulse circuits of each counter tray have been OR-gated. A presettable summing circuit, connected to each OR-gate output, enabled the selection of tray events where only one, two or more than two counter pairs have been discharged simultaneously. The output of the summing circuit was then connected in coincidence with the NORTH and SOUTH outputs. Then by appropriate presetting of each trays summing circuit various degrees of constriction have been applied to the recording of 3-fold coincidences. For example, setting all summing circuits for "one only" will reject all 3-fold coincidence events if more than one counter-pair is discharged in each tray, i.e. in all probability the recorded event is due to a genuine high zenith angle particle. The total NORTH and SOUTH count rate has been then measured by various combinations of the summing circuit settings. Hourly count totals have been accumulated for at least one day for each run to obtain a statistically significant count rate. The result is pictured in Fig. 3-2. The hourly count rates are not pressure corrected, therefore quantitative conclusions can only be drawn with regard to the N/S count ratios or the approximate counting levels.

Under certain assumptions regarding the air shower and the cascade shower component, the observed 3-fold coincidence rate can be attributed to one of the following types of events:

(i) genuine high zenith angle particle (genuine = arrival direction within the angle of acceptance of the telescope)

(ii) genuine high zenith angle particle with cascade shower production

(iii) virtual high zenith angle particle with cascade shower

production (virtual = arrival direction outside the angle of acceptance of the telescope)

(iv) air showers with axis within the acceptance angle

(v) air showers with axis outside the acceptance angle

(vi) types (iv) and (v) combined with cascade showers

(vii) soft (electron) showers from the vertical direction

(viii) accidental coincidences due to cosmic rays

(ix) accidental coincidences due to counter background radiation

(x) any combination of cases (i) to (ix)

In the present discussion the "air shower component" will include the penetrating showers (muon showers) and electron showers with sufficiently high energy to penetrate through the absorber plates. Furthermore, air showers are assumed to have a small solid angle and a lateral spread extending over more than one counter pair. Under cascade showers we define electron showers produced within the absorber. It will be assumed that these showers have an angular distribution of approximately 180°. (This is a coarse approximation only; scattering will occur in all directions, i.e. albedo radiation, although with a much reduced distribution in the opposite direction to that of the shower producing particle.)

We shall now endeavour to evaluate the six comparative measurments of the NORTH and SOUTH coincidence count rate in the light of the above considerations. The subscript of Σ represents the maximum allowable number of simultaneous counter pair discharges in the counter tray, i.e. $\Sigma_2 A$ indicates that "two or less" counter

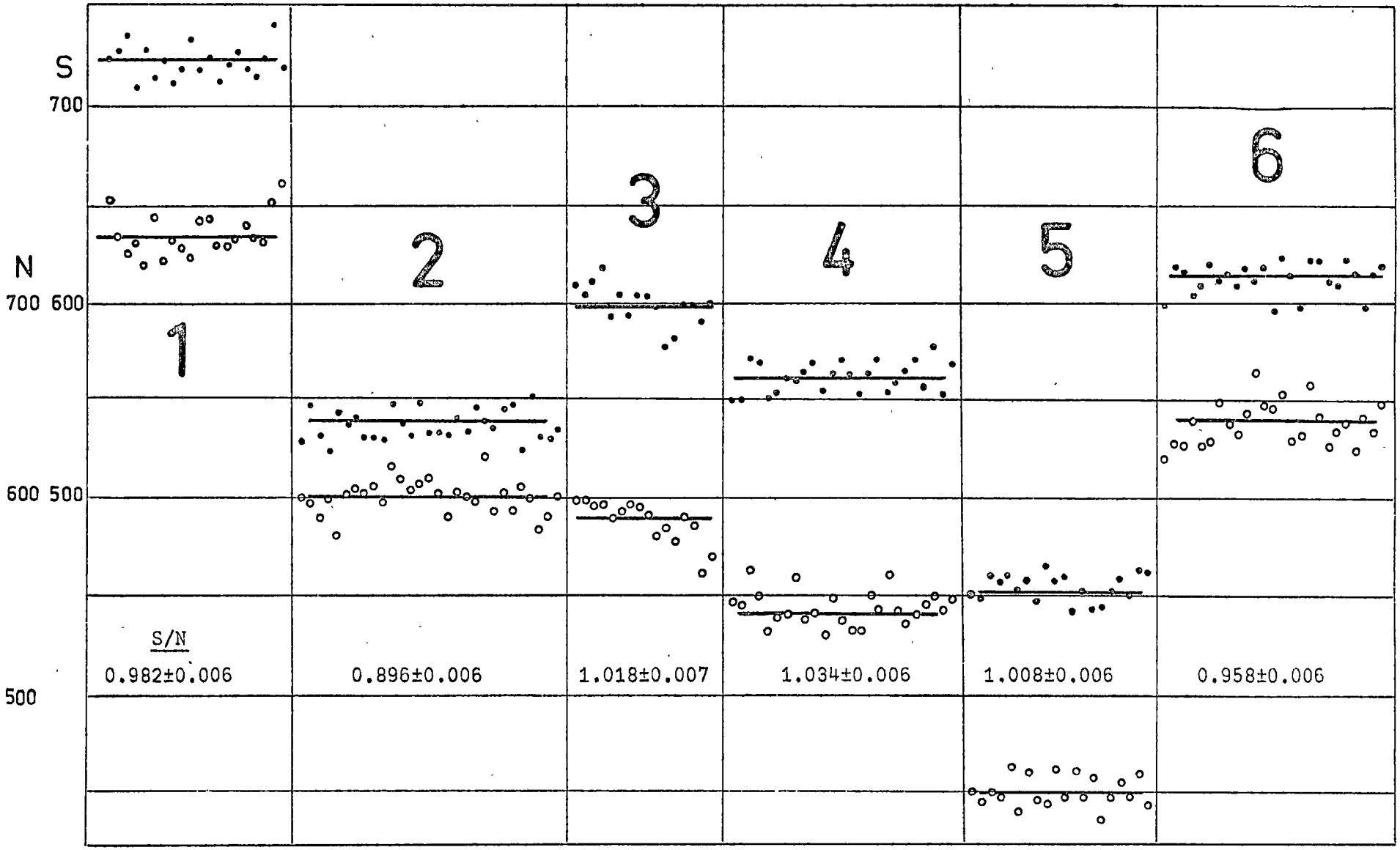

Fig.3-2 Effect of cascade showers on the 3-fold coincidence rates. (See text)
Open circles: NORTH coincidence; full circles: SOUTH coincidence.

pairs have been discharged in tray A in the case of a recorded coincidence event (see also fig.3-1). The six intervals of measurements of fig. 3-2 represent the following summing circuit settings:

1 $\Sigma_{32}A$; $\Sigma_{30}B$; $\Sigma_{31}C$ (no coincidence restriction)

2 $\Sigma_{1}A$; $\Sigma_{30}B$; $\Sigma_{31}C$

3 $\Sigma_{32}A$; $\Sigma_{1}B$; $\Sigma_{31}C$

4 $\Sigma_{32}A$; $\Sigma_{30}B$; $\Sigma_{1}C$

5 $\Sigma_{1}A$; $\Sigma_{1}B$; $\Sigma_{1}C$ (highest degree of restriction)

6 $\Sigma_{2}A$; $\Sigma_{2}B$; $\Sigma_{2}C$

To each of the six measurements in the two azimuth directions one can now assign the types of possible coincidence events. Indices $_N$ and $_S$ indicate the azimuth direction of the events and that of the observed coincidence. The observed count rates $1_N \ldots 6_S$ are the composition of the following types of events:

$$1_N = \sum (i)_N\ (ii)_N\ (iii)_N\ (iii)_S\ (iv)_S\ (v)\ (vi)_N\ (vi)_S\ (vii)\ (viii)\ (ix)\ (x)$$

$$1_S = \sum (i)_S\ (ii)_S\ (ii)_N\ (iii)_S\ (iii)_N\ (iv)_S\ (iv)_N\ (v)\ (vi)_S\ (vi)_N\ (vii)\ (viii)\ (ix)\ (x)$$

$$2_N = \sum (i)_N\ (ii)_N\ (iii)_N\ (vii)^*\ (viii)\ (ix)$$

$$2_S = \sum (i)_S\ (ii)_N\ (iii)_N\ (viii)\ (ix)$$

$$3_N = \sum (i)_N\ (iii)_S\ (vii)^*\ (viii)\ (ix)$$

$$3_S = \sum (i)_S\ (ii)_S\ (iii)_S\ (vii)^*\ (viii)\ (ix)$$

$$4_N = \sum (i)_N\ (ii)_S\ (iii)_S\ (viii)\ (ix)$$

$$4_S = \sum (i)_S\ (ii)_S\ (iii)_S\ (viii)\ (ix)$$

$$5_N = \sum (i)_N\ (ix)$$

$$5_S = \sum (i)_S\ (ix)$$

* within restricted zenith angle region

$$6_N = \sum (i)_N \; (ii)_N \; (ii)_S \; (iii)_N \; (iii)_S \; (iv)_N \; (viii) \; (ix)$$

$$6_S = \sum (i)_S \; (ii)_S \; (ii)_N \; (iii)_S \; (iii)_N \; (iv)_S \; (viii) \; (ix)$$

Events of very low probability, e.g. boundary conditions, have been excluded in the above listing. The horizontal cosmic ray intensity and the flux of albedo particles ($\theta > 90^{\circ}$) has been assumed to be negilgible.

Calculation of the contribution of the various types of events to each of the observed coincidence rates is a formidable task and beyond the scope of the present work. The number of measurements is too restrictive to obtain experimental estimations for the individual contributions by successive elimination of events of common origin. A possible way to overcome this problem would be to record each event in detail. Subsequent analysis of the recorded events for a given time interval would then enable the estimation of the frequency of occurrences of each type of coincidence events.

A circuit to enable the visual inspection of each coincidence event had, in fact, been constructed. A pulse storage circuit, consisting of a pair of cross-coupled DTL NAND-gates had been attached to the pulse shaping circuit of each counter pair. The output of each flip-flop was connected to a neon indicator light through suitable driving circuit. The geometrical arrangement of the neon lights corresponded to that of the counter pairs in the telescope. The coincidence pulse was then used to trigger each flip-flop into the appropriate "on" or "off" position, corresponding to the state of the counter pairs at the instant of the coincidence event. With this circuit the occurrence of all types of events (i) to (vii)

have been visually verified. Unfortunately, lack of suitable high speed data storage medium at the time of the experiment prevented the permanent recording and analysis of events. It is proposed, that such an experiment is to be carried out in the future.

Despite the shortcomings of the experiment carried out with the use of the summing circuits, inspection of the observed count rates in the six different configurations reveals some characteristics of the telescope with respect to cascade showers. Because of the non-symmetrical absorber geometry, coincidences involving cascade shower events are expected to have different contributions to the NORTH and SOUTH coincidence count rate. The S/N ratio will give a partial measure of this asymmetry.

Contrary to the expectation on the basis of the number of possible types of events in interval 1 (1_S containing $(ii)_N$ type events, but no $(ii)_S$ events possible in 1_N), a S/N ratio of 0.98 has been observed. The excess in the NORTH coincidence rate can be explained as the unequal contribution of the shower producing events to the NORTH and SOUTH coincidence rate. "Virtual" high zenith angle particles incident on tray A and producing cascade showers with a resulting NORTH coincidence have a larger possible zenith angle opening for the direction of arrival than similar particles arriving from the opposite azimuth. The excess in the NORTH count rate is therefore due predominantly to type (iii) events. This is further illustrated in interval 3, where cascade shower events from the north are effectively rejected, but events of the same type from the south will still be recorded. An excess

of the SOUTH coincidence rate is now recorded. In addition to the cascade events, by definition events of the types (iv) and (v) are also rejected in interval 3.

Intervals 2 and 4 give a further example of shower rejection from the two azimuth directions. The relatively large reduction of the SOUTH count rate in interval 2 is due to the fact that all shower events, including those of types (ii) and (iv), are rejected. (This is undesirable from the point of maximum obtainable high zenith angle count rate.) A slightly less reduction of the NORTH count rate in interval 4 is probably due to the greater distance of counter tray C from the absorber plates and the absorbing effect of the intervening counter tray B on shower particles of marginal energy. (See also Ch. 3.4).

Interval 5 imposes the most severe restriction on the coincidence count rate. Practically all recorded events will be of type (i), the probability of accidental coincidences being extremely small. The count rates for the two directions are identical within the statistical limits. It would appear that the coincidence arrangement of 5 represents the ultimate precaution against air shower contamination of the high zenith angle count rate. Unfortunately, together with undesirable air showers, a large number of otherwise acceptable coincidence events of the types (ii) (iv) (vi) and (x) would also be rejected, resulting in the reduction of the efficiency of the telescope in the observation of the high zenith angle muon flux.

Finally, interval 6 represents a case of coincidence restriction between that of 1 and 5. Air showers with extensive lateral spread, also cascade showers with large angular distribution are rejected.

Again, because of the wider zenith angle distribution of $(iii)_N$ events, the NORTH count rate is predominant. Due to the cosine power law of the zenith angle dependence of cosmic rays, the effect of the absorber will be a small reduction of the effective zenith angle of the telescope.

3.3 Response Characteristics of the High Zenith Angle Telescope

To observe spatial cosmic ray intensity variations a detector with directional sensitivity is required. A practical telescope geometry is an optimum compromise between angular resolution and the statistically required count rate taking into account the observational features of interest of the particular experiment and the asymptotic direction of viewing of the telescope.

Two important quantities characterise any given telescope geometry, independent of location, the geometric sensitivity and the radiation sensitivity. The former gives the directional response of the telescope in the presence of isotropic radiation and is purely a function of the geometric arrangement of the geiger counters. The radiation sensitivity on the other hand is calculated by taking into account the zenith angle dependence of the cosmic ray flux.

The zenith angle distribution of muons at sea level is a function of the integral energy E_μ and can be calculated by means of the diffusion equation of cosmic ray muons in the atmosphere. Such calculations have been carried out by Kasten (1962), Maeda (1964) and others. The results indicate a peaking of the calculated inclined to vertical intensity ratio I_θ/I_o for high integral muon energies at high zenith angles and a gradual drop off of the

ratio with increasing zenith angles for lower cut-off energies $E_\mu < 40$ GeV.

For the quantitative assessment of the zenith angle distribution of cosmic rays the empirical formula derived by Nash (1965) will yield satisfactory results. The cosmic ray intensity as a function of zenith angle is given by

$$I_\theta = I_o(\cos^{2.2}\theta + k) \qquad (3\text{-}9)$$

where I_θ represents the intensity at zenith angle θ and I_o is the intensity in the vertical direction. k is a constant, approximately $I_o/300$ for high zenith angles.

To calculate the radiation sensitivity of the high zenith angle telescope, the sensitive area has been subdivided into small elements and the radiation sensitivity has been calculated for each element. A computer program devised by Cooke (1971) enabled the rapid calculation of the element sensitivities for different zenith angles. The sum of the contributions of the telescope elements for each of the selected zenith angle intervals enables the plotting of the radiation sensitivity curve of the high zenith angle telescope as in fig. 3-3.

In the presence of the geomagnetic field charged primary cosmic ray particles are deflected. The curvature of the particle orbit in the magnetosphere is dependent on the energy of the primary particle and the field vector of the terrestrial magnetic field relative to the direction of the arrival of the primary. The asymptotic direction of viewing of a detector therefore will be a function of the primary energy and the geomagnetic location of the telescope in addition to the direction of viewing and the

given geometry. The asymptotic cones of the high zenith angle telescope together with those of the other surface and underground muon detectors in the Mawson cosmic ray observatory are given in the Appendix for a range of primary rigidities. The diagrams have been obtained using the 'asymptotic cone' program developed and described in detail by Cooke (1971).

The momentum spectrum observed with the high zenith angle telescope is similar to that measured by Kasha et al. (1967) in fig. 3-4. The range of the accepted zenith angles of the spectograph (66.5° - 84.5°) bears close resemblance to that of the high zenith angle telescope (67° - 85°). The measured momentum spectrum is at sea level, at the detector. The question arises: how does the spectrum of fig. 3-4 relate to the primary cosmic ray spectrum?

The observed momentum spectrum at sea level is different from the rigidity spectrum of the primary cosmic ray flux. The relationship between the primary and secondary cosmic radiation is represented by the coupling co-efficients, a concept already introduced in Chapter 2. To appreciate the importance of the primary-secondary relationship it will be sufficient here to define the coupling co-efficient.

The coupling co-efficient is the differential contribution of the primaries of given momentum E to the observed secondary count rate and can be expressed as a zenith angle dependent function of the form.

$$W(E,\theta,h) = J(E)\ S(E,\theta,h)/N(\theta,h) \qquad (3\text{-}10)$$

where $J(E)$ is the primary energy spectrum, $S(E,\theta,h)$ the corresponding

yield function at the atmospheric depth h and zenith angle θ, and $N(\theta,h)$ is the integrated directional intensity of the secondary component.

Coupling co-efficient functions for various zenith angles and atmospheric depths have been given by many authors on the basis of both theoretical calculations and experimental measurements. The divergence of the results is due to the incomplete knowledge of the production mechanism of secondaries in the atmosphere.

As an example, the coupling co-efficient for the high zenith angle telescope has been plotted in fig. 3-5 based on the calculations of Cooke (1971).

Only in the full knowledge of the radiation sensitivity, the asymptotic direction of viewing and the appropriate coupling co-efficient is it possible to determine the response of a detector at a particular location and depth to any given type of anisotropy of the primary cosmic ray flux.

3.4 Construction and Installation of the Telescope

Having proven the feasibility of the high zenith angle telescope with the trial experiment, work proceeded on the construction of two full scale telescopes. After functional testing, one unit was to be shipped to Mawson in late 1967, the second unit was to operate in Hobart for a period of one year to enable data comparison of two identical telescopes at different locations. Delay in the construction prevented the completion of the second unit until 1969. A third unit had been constructed in 1970, and the two remaining units were despatched to Mawson at the end of 1971 to be installed together with the other detectors in the new observatory.

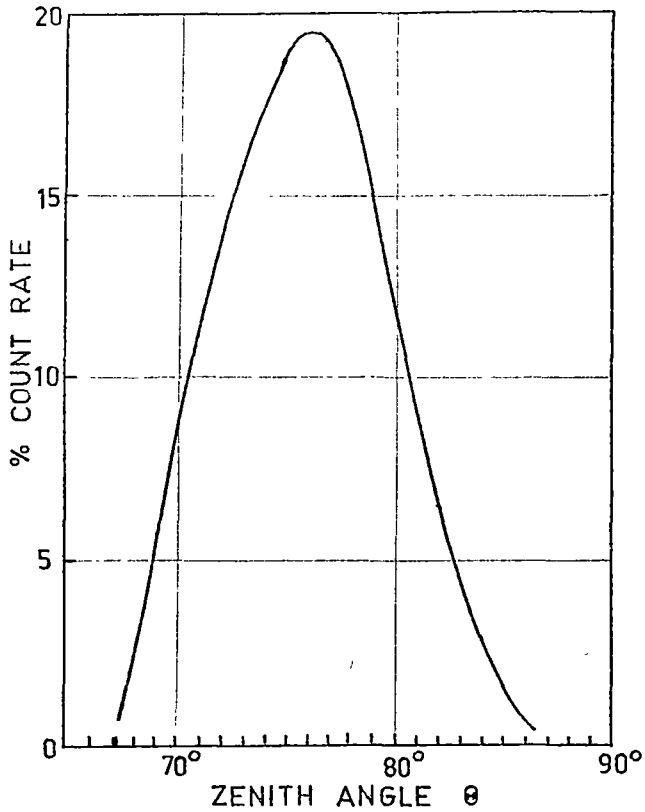

Fig.3-3. Zenith angle dependence of radiation sensitivity of high zenith angle telescope (Cooke 1971).

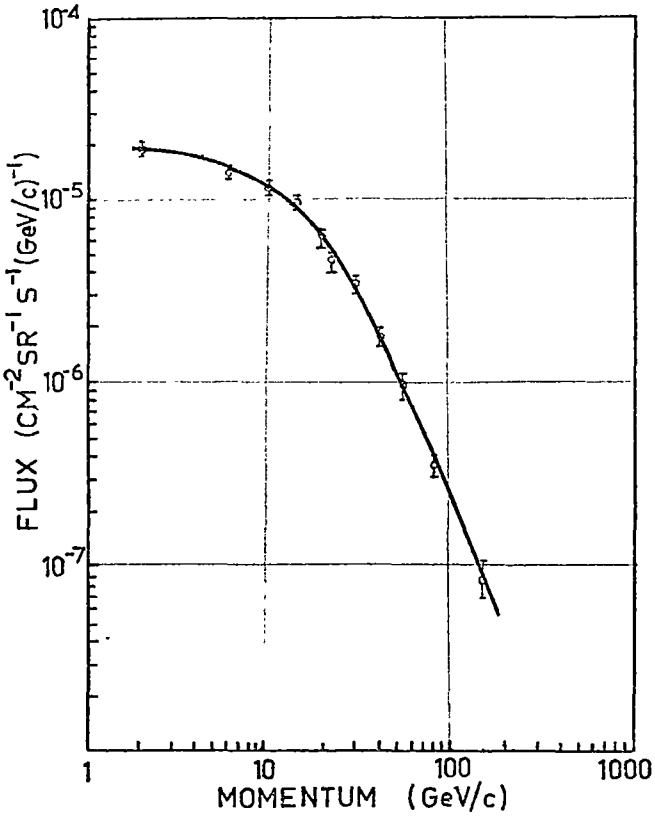

Fig.3-4. The measured momentum spectrum of muons at $\theta = 76^{\circ}$ (Kasha et al. 1967)

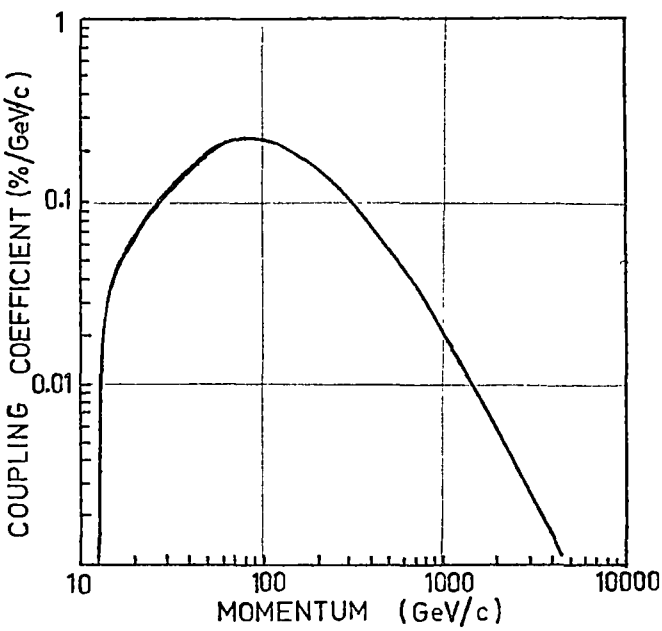

Fig.3-5. Coupling coefficient function for the high zenith angle telescope. The mean effective atmospheric cut-off is P_{at} = 12.82 GeV/c. (Cooke,1971)

The high zenith angle of viewing coupled with the narrow aperture makes the count rate of the telescope very sensitive to change in the zenith angle setting. A steel framework of adequate strength had been designed to carry the steel absorber plates and the counter trays without deformation (fig. 3-6). The counter support strips are made of 12 mm thick PVC material. Sufficient clearance is provided between the counters and tray covers to eliminate the possibility of electrical break-down between counter cathode and the telescope framework. After installation of the counters, a test voltage of 3000 V has been applied between each counter cathode and the framework to test for high voltage break-down.

In the final installation the telescope has been levelled by means of four levelling screws to a zenith angle accuracy better than 2 minutes of arc.

Great attention has been given to obtain a stable temperature environment for the operation of the telescope. During the winter months the laboratory temperature has been held at a constant value of $18^{o}C$ with a thermostatically controlled oil heater. In the summer months, however, large diurnal temperature variation of the laboratory occurred due to the solar radiation absorbed by the roof and wall panels of the building.

In the study of diurnal variations any spurious daily variation of the detectors count rate associated with the diurnal temperature variation of the observatory (e.g. counter end effect) will have serious repercussions. A reliable temperature control had to be therefore devised to overcome the temperature problem in the

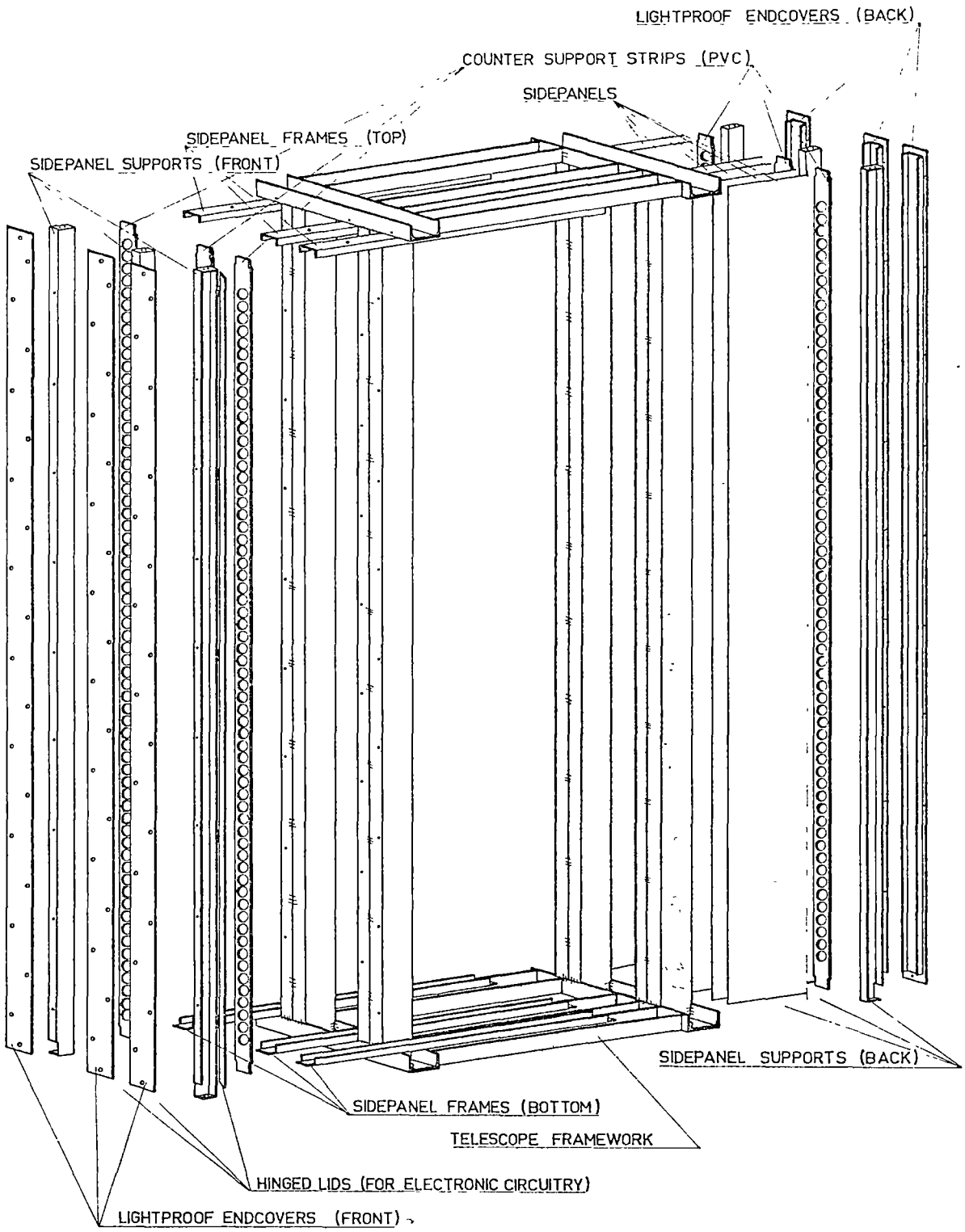

FIG3-6 HIGH ZENITH ANGLE MESON TELESCOPE — ASSEMBLY DIAGRAM.

summer. A small air intake fan with thermostatic control was installed in the west wall of the observatory. When the room temperature exceeded the preset limit, the air inlet fan draw cold air from the outside into the air stream of the internal air circulating fans. Careful setting of both the heater and inlet fan thermostats ensured a constant and uniform temperature distribution throughout the building.

It is felt to be worth-while to recount here an incident relating to cascade showers, encountered during the installation of the high zenith angle telescope:

After completion of the installation, extensive tests were carried out to ensure the proper operation of the telescope. During the routine testing of the back-ground count rate of the individual counters it was found, that some counters in tray C had a back-ground rate well in excess of expectation. Replacement of all questionable counters with bench-tested ones failed to cure the problem; counter failure therefore had to be excluded. Next, cross-talk between the twisted pair signal lines was suspected to be the cause of trouble. Extensive testing of scores of combinations of the signal lines in simulated conditions with facsimile geiger pulses failed to produce extra counter pulses at the coincidence circuit. Finally, a counter pair with independent power supply, amplifier and counting unit duplicating those of the telescope was improvised to discover the location of any possible local radioactive material.

Moving the counter pair in the vertical direction alongside of counter tray C, a peak back-ground, some 30% over the normal rate,

was observed at some point, about 1 m above the base of the telescope. Further tests had proved that the cause of the high back-ground rate was the lead absorber of the vertical telescope, in close proximity to the newly installed high zenith angle telescope. Although the extreme tray was markedly affected, only slight increase of the back-ground rate of the counters in tray B was observed, supporting an earlier conjecture in chapter 3-2 regarding cascade showers.

(It would have been better to think of the physical principles before suspecting the electronics.)

3.5 Results of Observation

3.5.1 Harmonic Analysis

The accepted method for the calculation of both the solar and sidereal diurnal variation is the evaluation of the Fourier co-efficients by the least squares method by Whittaker and Robinson (1944). In general form, the deviation of intensity ΔI at the time t from the mean value over the period T is represented by the Fourier series

$$\Delta I = \sum_{i=o}^{\infty} \left(a_i \cos\frac{2k\pi it}{T} + b_i \sin\frac{2k\pi it}{T}\right) \qquad (3\text{-}11)$$

Sufficient accuracy can be achieved in replacing the daily variation with the best estimate of the first and second terms of the series. Equation 3-11 will then reduce to

$$\Delta I = a_1\cos\phi + b_1\sin\phi + a_2\cos 2\phi + b_2\sin 2\phi \qquad (3\text{-}12)$$

where $\phi = \frac{2k\pi}{m}$, m being the number of experimental values in the interval T.

The coefficients a_1, b_1, a_2, b_2 are then evaluated by minimizing

the mean square deviation of the above expression from the experimental figures U_k. For bi-hourly experimental values $U_k = U_o, U_1 \ldots U_{11}$ harmonic coefficients of the diurnal variation are calculated on a 12 ordinate scheme. The values U_k are the percentage deviations from the mean intensity, i.e.

$$U_k = \frac{I_k - \bar{I}}{\bar{I}} .100 \qquad (3\text{-}13)$$

The requirement of minimum deviation is fulfilled by the expression for the coefficients:

$$a_1 = \frac{1}{6}\sum_{k=o}^{11} U_k \cos\frac{k\pi}{6} \qquad a_2 = \frac{1}{6}\sum_{k=o}^{11} U_k \cos\frac{k\pi}{3}$$

$$b_1 = \frac{1}{6}\sum_{k=o}^{11} U_k \sin\frac{k\pi}{6} \qquad b_2 = \frac{1}{6}\sum_{k=o}^{11} U_k \sin\frac{k\pi}{3} \qquad (3\text{-}14)$$

The significant quantities for the study of the diurnal variation of the cosmic ray intensity are the amplitude and the phase of the first and second harmonics of the diurnal wave. Their physical significance is explained in Chapter 2.

The amplitude of the first harmonic is given by

$$R_1 = (a_1^2 + b_1^2)^{\frac{1}{2}} \qquad (3\text{-}15)$$

and the phase angle is determined as

$$f_1 = \arctan\frac{a_1}{b_1} \qquad (3\text{-}16)$$

and similarly for the second harmonic:

$$R_2 = (a_2^2 + b_2^2)^{\frac{1}{2}} \qquad (3\text{-}17)$$

$$f_2 = \arctan\frac{a_2}{b_2} \qquad (3\text{-}18)$$

To calculate the time of maximum intensity the phase angle must

be shifted forward by a constant Φ . The value of Φ depends on the centering of the time interval and the number of experimental points m. For a 12 ordinate scheme centered on the odd hours $\Phi = 15^{\circ}$. The time of maximum will be then

$$T_{max} = \frac{f_1 + \Phi}{15} \text{ hours.} \qquad (3\text{-}19)$$

The amplitude is adjusted for smoothing error introduced by the finite number of data points employed. The multiplying factors for R_1 and R_2 are 1.012 and 1.047 respectively (Parsons, 1959).

The standard error of the calculated amplitude is estimated from the mean counting rate under the assumption that the number of particles detected is a Poisson variable:

$$\sigma(R) = 100 \left(\frac{2}{m.n.\bar{N}} \right)^{\frac{1}{2}} \qquad (3\text{-}20)$$

where $\bar{N}$ is the mean hourly count rate derived from n hourly values.

Tabulated values of the annual running means of the first and second harmonics of both the solar and sidereal daily variations are given in Table 3-1 for the north and south azimuth of the high zenith angle telescope. The data were obtained between March 1968 and December 1971. In January 1972 observations were interrupted because of transfer of the telescope to the new observatory. When observation resumed at the new site, the geometry had been changed, as outlined in Chapter 4.

The data used in the present harmonic analysis are uncorrected for atmospheric effects. Fourier analysis of the surface pressure at Mawson exhibited insignificant diurnal variation. Consequently, the results obtained can be assumed to be of primary origin.

T_1, T_2 are the calculated standard errors of times of maxima of the first and second harmonics respectively.

R_{meas} is the observed standard error of the amplitudes.

R_{est} is the theoretical standard error of the amplitudes.

R_1, R_2 are the amplitudes of the first and second harmonics.

T_{max1}, T_{max2} are the times of maxima of the first and second harmonics.

TABLE 3-1(A) HARMONIC ANALYSIS

TELESCOPE: MAWSON HIGH ZENITH ANGLE NORTH

SOLAR ANNUAL RUNNING MEANS (TIME IN GMT HOURS)

		STANDARD ERROR				DIURNAL		SEMI-DIURNAL	
		T_1	T_2	R_{meas}	R_{est}	R_1	T_{max1}	R_2	T_{max2}
1969	FEB	0.73	0.61	.019	.021	.101	16.15	.061	01.24
	MAR	0.64	0.95	.019	.021	.113	15.63	.040	01.25
	APR	0.53	0.88	.018	.021	.130	15.15	.040	01.52
	MAY	0.47	1.33	.017	.021	.139	15.07	.026	00.69
	JUN	0.43	2.04	.016	.021	.141	14.76	.018	10.99
	JUL	0.43	6.00	.016	.021	.145	14.44	.008	11.45
	AUG	0.40	1.14	.015	.021	.142	14.63	.027	10.64
	SEP	0.65	1.44	.020	.021	.121	15.31	.030	10.80
	OCT	0.58	1.26	.022	.021	.143	15.21	.035	00.04
	NOV	0.58	6.00	.021	.020	.141	15.37	.013	11.34
	DEC	0.61	1.57	.025	.020	.158	15.34	.035	00.38
1970	JAN	0.56	1.08	.024	.020	.166	15.02	.045	00.39
	FEB	0.60	1.14	.025	.020	.163	15.31	.045	00.49
	MAR	0.64	0.92	.025	.020	.149	14.70	.053	11.87
	APR	0.61	0.67	.024	.020	.150	14.66	.069	11.75
	MAY	0.67	0.77	.026	.020	.147	14.95	.066	00.15
	JUN	0.67	0.87	.026	.020	.151	14.83	.060	00.41
	JUL	0.62	0.65	.024	.021	.148	14.84	.072	00.39
	AUG	0.50	0.65	.021	.021	.162	14.20	.063	00.67
	SEP	0.50	0.82	.024	.021	.181	13.71	.057	00.41
	OCT	0.48	1.10	.022	.021	.173	13.77	.040	11.80
	NOV	0.49	0.68	.021	.021	.166	13.27	.062	11.76
	DEC	0.48	1.00	.020	.021	.155	12.63	.039	11.66
1971	JAN	0.59	0.95	.022	.021	.142	12.51	.046	11.46
	FEB	0.51	1.23	.023	.021	.173	12.22	.038	11.72
	MAR	0.64	1.36	.027	.021	.161	12.34	.041	11.95
	APR	0.68	1.85	.027	.021	.152	12.09	.032	11.86
	MAY	0.61	6.00	.024	.020	.153	11.39	.023	11.54
	JUN	0.59	1.50	.022	.020	.145	11.44	.032	11.58
	JUL	0.68	6.00	.023	.020	.131	11.30	.021	00.22
	AUG	0.95	2.21	.024	.020	.097	11.21	.026	11.16
	SEP	0.74	1.84	.021	.020	.111	11.13	.026	10.31
	OCT	0.63	2.29	.021	.020	.130	11.78	.023	00.16
	NOV	0.55	6.00	.022	.021	.153	12.43	.014	09.47
	DEC	0.44	1.12	.019	.021	.168	12.91	.035	10.26

TABLE 3-1(B) HARMONIC ANALYSIS

TELESCOPE: MAWSON HIGH ZENITH ANGLE NORTH

SIDEREAL ANNUAL RUNNING MEANS (TIME IN LOCAL SIDEREAL HOURS)

		STANDARD ERROR				DIURNAL		SEMI-DIURNAL	
		T_1	T_2	R_{meas}	R_{est}	R_1 %	T_{max1}	R_2 %	T_{max2}
1969	FEB	4.01	0.78	.024	.021	.028	21.43	.061	06.90
	MAR	3.41	0.86	.023	.021	.030	23.97	.054	07.56
	APR	2.77	0.84	.024	.021	.036	02.55	.056	07.74
	MAY	2.69	0.80	.023	.021	.035	03.53	.056	07.06
	JUN	2.12	0.60	.022	.021	.043	04.38	.073	06.73
	JUL	1.86	0.55	.022	.021	.047	05.43	.077	06.49
	AUG	1.94	0.78	.023	.021	.048	04.79	.058	06.65
	SEP	1.16	0.79	.023	.021	.078	04.27	.058	06.52
	OCT	1.24	0.56	.022	.021	.070	03.20	.077	06.82
	NOV	1.10	0.69	.021	.020	.075	03.42	.060	06.34
	DEC	0.93	0.86	.021	.020	.089	02.96	.049	07.11
1970	JAN	0.74	0.92	.019	.020	.097	02.42	.041	07.36
	FEB	0.85	0.92	.019	.020	.088	02.76	.042	07.25
	MAR	0.68	1.60	.018	.020	.104	01.85	.025	06.91
	APR	0.65	0.97	.018	.020	.106	01.90	.037	06.18
	MAY	0.72	1.51	.018	.020	.099	01.56	.026	06.76
	JUN	0.69	2.12	.017	.020	.097	01.76	.019	06.08
	JUL	0.90	6.00	.023	.021	.100	01.78	.008	06.29
	AUG	1.21	6.00	.023	.021	.074	02.44	.021	06.48
	SEP	2.49	6.00	.028	.021	.045	02.50	.012	06.86
	OCT	2.31	6.00	.029	.021	.051	02.97	.012	01.56
	NOV	12.0	6.00	.031	.021	.029	03.72	.010	07.16
	DEC	12.0	6.00	.033	.021	.004	09.60	.022	04.51
1971	JAN	12.0	6.00	.030	.021	.017	12.81	.014	04.75
	FEB	12.0	6.00	.032	.021	.017	00.59	.022	05.26
	MAR	12.0	6.00	.031	.021	.008	21.00	.028	05.34
	APR	12.0	6.00	.027	.021	.021	21.18	.020	05.06
	MAY	2.86	6.00	.028	.020	.041	23.70	.024	04.21
	JUN	2.37	6.00	.027	.020	.047	23.19	.016	04.62
	JUL	1.83	2.38	.028	.020	.062	23.46	.030	04.46
	AUG	1.08	6.00	.026	.020	.093	00.10	.017	03.95
	SEP	1.16	6.00	.024	.020	.081	23.74	.012	02.58
	OCT	0.95	6.00	.025	.020	.101	22.92	.012	07.74
	NOV	0.74	6.00	.026	.021	.134	22.91	.017	03.83
	DEC	0.70	6.00	.028	.021	.153	23.36	.015	06.78

TABLE 3-1(C) HARMONIC ANALYSIS

TELESCOPE: MAWSON HIGH ZENITH ANGLE NORTH

ANTI-SIDEREAL ANNUAL RUNNING MEANS (TIME IN LOCAL ANTI-SIDEREAL HOURS)

		STANDARD ERROR				DIURNAL		SEMI-DIURNAL	
		T_1	T_2	R_{meas}	R_{est}	R_1 %	T_{max1}	R_2 %	T_{max2}
1969	FEB	0.84	6.00	.015	.021	.069	13.51	.010	03.44
	MAR	0.83	1.30	.013	.021	.061	12.50	.021	00.86
	APR	1.22	2.46	.015	.021	.047	11.25	.015	00.88
	MAY	1.34	1.37	.014	.021	.041	10.60	.021	10.78
	JUN	1.69	1.37	.014	.021	.033	11.40	.021	08.86
	JUL	2.17	6.00	.017	.021	.031	12.95	.016	09.76
	AUG	2.20	6.00	.015	.021	.027	12.01	.011	06.89
	SEP	2.14	6.00	.017	.021	.033	07.81	.014	06.35
	OCT	4.60	1.21	.019	.021	.020	10.61	.032	05.30
	NOV	12.0	0.65	.016	.020	.014	10.40	.049	06.06
	DEC	2.82	1.53	.019	.020	.028	12.28	.026	06.48
1970	JAN	1.84	1.16	.017	.020	.037	10.77	.030	07.15
	FEB	1.92	1.27	.019	.020	.039	12.03	.030	07.31
	MAR	12.0	1.84	.017	.020	.011	12.84	.021	06.15
	APR	12.0	2.00	.016	.020	.009	12.71	.019	04.50
	MAY	3.30	0.88	.015	.020	.019	11.35	.033	04.32
	JUN	12.0	0.72	.016	.020	.014	11.79	.042	04.05
	JUL	12.0	1.10	.018	.021	.017	11.71	.033	04.41
	AUG	1.61	1.30	.015	.021	.036	15.22	.024	03.78
	SEP	1.09	1.44	.018	.021	.065	15.28	.027	03.07
	OCT	1.32	6.00	.019	.021	.057	15.32	.015	01.08
	NOV	1.58	1.07	.019	.021	.048	13.77	.036	00.66
	DEC	2.74	1.26	.020	.021	.030	11.45	.032	01.91
1971	JAN	12.0	1.75	.020	.021	.016	12.21	.025	02.16
	FEB	2.26	1.58	.020	.021	.035	07.53	.027	01.47
	MAR	2.83	2.42	.021	.021	.031	09.03	.022	01.67
	APR	3.89	6.00	.019	.021	.023	10.56	.016	01.04
	MAY	2.97	6.00	.018	.020	.025	15.25	.006	00.61
	JUN	2.88	6.00	.018	.020	.027	14.08	.012	11.35
	JUL	2.48	2.20	.021	.020	.035	12.44	.023	00.37
	AUG	1.72	2.32	.021	.020	.047	09.40	.022	01.57
	SEP	1.55	1.26	.020	.020	.050	10.49	.032	01.17
	OCT	1.49	1.44	.020	.020	.051	12.60	.029	02.63
	NOV	1.09	6.00	.022	.021	.077	13.86	.009	04.56
	DEC	0.94	6.00	.025	.021	.102	14.12	.016	08.82

TABLE 3-1(D) HARMONIC ANALYSIS

TELESCOPE: MAWSON HIGH ZENITH ANGLE SOUTH

SOLAR ANNUAL RUNNING MEANS (TIME IN GMT HOURS)

		STANDARD ERROR				DIURNAL		SEMI-DIURNAL	
		T_1	T_2	R_{meas}	R_{est}	R_1 %	T_{max1}	R_2 %	$T_{max\ 2}$
1969	FEB	2.72	1.30	.028	.021	.042	05.85	.044	06.46
	MAR	2.55	1.27	.030	.021	.048	06.87	.048	05.85
	APR	2.24	2.19	.030	.021	.055	06.61	.033	05.71
	MAY	2.49	2.08	.030	.021	.049	06.42	.034	06.42
	JUN	1.76	2.49	.029	.021	.064	05.74	.030	07.38
	JUL	2.14	6.00	.027	.021	.051	06.51	.023	07.09
	AUG	1.66	6.00	.025	.020	.060	06.34	.012	06.53
	SEP	2.19	6.00	.027	.021	.050	05.95	.014	03.53
	OCT	2.34	2.66	.024	.021	.042	06.39	.025	00.77
	NOV	3.12	6.00	.025	.021	.034	05.84	.021	01.89
	DEC	12.0	0.85	.024	.021	.021	07.25	.056	01.55
1970	JAN	12.0	1.06	.024	.021	.019	08.83	.045	01.75
	FEB	12.0	1.09	.024	.020	.010	18.56	.044	01.69
	MAR	12.0	0.90	.020	.020	.016	14.30	.045	01.65
	APR	2.07	0.74	.020	.021	.039	15.64	.053	01.79
	MAY	2.19	0.76	.022	.021	.041	14.42	.057	02.37
	JUN	1.60	0.79	.023	.021	.056	14.82	.056	02.85
	JUL	1.35	0.81	.018	.021	.053	14.44	.044	03.21
	AUG	1.49	1.18	.020	.021	.052	13.72	.034	03.19
	SEP	1.85	1.82	.020	.021	.043	12.26	.025	03.18
	OCT	1.55	1.50	.020	.021	.050	11.85	.028	04.65
	NOV	1.35	1.49	.018	.021	.053	11.29	.026	04.67
	DEC	2.41	1.27	.021	.021	.036	11.53	.035	06.33
1971	JAN	2.92	1.71	.023	.021	.033	10.11	.029	06.19
	FEB	1.63	6.00	.025	.021	.060	10.50	.012	06.62
	MAR	1.76	6.00	.025	.021	.055	09.44	.002	10.60
	APR	1.65	6.00	.024	.020	.056	09.04	.003	01.08
	MAY	1.80	6.00	.022	.020	.048	08.37	.010	00.86
	JUN	1.84	6.00	.024	.020	.051	08.10	.015	11.75
	JUL	1.93	2.39	.023	.020	.048	07.52	.025	01.04
	AUG	2.72	2.15	.024	.020	.037	05.49	.027	00.90
	SEP	1.99	6.00	.022	.020	.045	06.02	.021	01.79
	OCT	2.75	1.64	.022	.020	.034	08.20	.029	02.02
	NOV	1.80	1.94	.023	.021	.051	08.72	.027	02.82
	DEC	1.46	6.00	.022	.021	.059	10.02	.022	02.41

TABLE 3-1(E) HARMONIC ANALYSIS

TELESCOPE: MAWSON HIGH ZENITH ANGLE SOUTH

SIDEREAL ANNUAL RUNNING MEANS (TIME IN LOCAL SIDEREAL HOURS)

		STANDARD ERROR				DIURNAL		SEMI-DIURNAL	
		T_1	T_2	R_{meas}	R_{est}	R_1 %	T_{max1}	R_2 %	T_{max2}
1969	FEB	1.98	6.00	.024	.021	.048	18.74	.011	11.59
	MAR	2.25	6.00	.024	.021	.044	19.79	.012	08.93
	APR	2.10	6.00	.026	.021	.050	20.20	.019	07.19
	MAY	2.00	6.00	.026	.021	.053	19.80	.025	06.25
	JUN	1.78	1.46	.026	.021	.057	21.01	.037	06.95
	JUL	1.55	1.67	.024	.021	.060	19.90	.031	06.70
	AUG	1.72	1.56	.022	.020	.051	20.04	.031	05.93
	SEP	1.51	0.91	.022	.021	.058	20.66	.049	05.93
	OCT	1.41	0.62	.024	.021	.068	20.79	.076	05.75
	NOV	1.38	0.70	.023	.021	.065	21.30	.063	05.58
	DEC	1.28	1.67	.024	.021	.073	22.10	.031	06.18
1970	JAN	1.24	1.14	.025	.021	.077	22.48	.044	06.27
	FEB	2.09	1.25	.026	.020	.049	22.90	.042	06.30
	MAR	1.75	1.21	.025	.020	.057	23.86	.042	06.25
	APR	2.43	0.89	.021	.021	.036	00.92	.047	06.55
	MAY	2.21	1.67	.024	.021	.043	01.96	.031	06.67
	JUN	3.51	1.44	.022	.021	.027	02.21	.031	05.80
	JUL	3.35	1.10	.024	.021	.031	02.91	.043	06.32
	AUG	3.13	1.27	.022	.021	.031	04.15	.036	06.66
	SEP	2.48	2.31	.025	.021	.041	05.98	.027	06.57
	OCT	3.10	6.00	.026	.021	.035	06.57	.007	07.26
	NOV	3.68	6.00	.026	.021	.032	07.43	.009	07.01
	DEC	2.06	1.57	.025	.021	.048	07.79	.034	05.96
1971	JAN	2.42	2.18	.026	.021	.044	08.81	.029	05.80
	FEB	2.36	2.29	.022	.021	.037	06.27	.023	04.50
	MAR	12.0	1.33	.023	.021	.021	06.03	.036	04.36
	APR	12.0	1.15	.020	.020	.018	05.01	.035	04.51
	MAY	12.0	1.03	.017	.020	.012	02.23	.032	04.88
	JUN	12.0	1.10	.018	.020	.016	02.23	.032	05.38
	JUL	2.89	0.98	.016	.020	.023	01.56	.032	04.42
	AUG	1.22	0.92	.015	.020	.047	00.99	.032	04.26
	SEP	1.71	1.41	.017	.020	.038	01.29	.025	04.91
	OCT	1.63	2.07	.021	.020	.052	23.51	.024	05.56
	NOV	1.71	6.00	.024	.021	.054	22.21	.020	04.59
	DEC	1.23	6.00	.023	.021	.074	22.54	.021	05.28

TABLE 3-1(F) HARMONIC ANALYSIS

TELESCOPE: MAWSON HIGH ZENITH ANGLE SOUTH

ANTI-SIDEREAL ANNUAL RUNNING MEANS (TIME IN LOCAL ANTI-SIDEREAL HOURS)

		STANDARD ERROR				DIURNAL		SEMI-DIURNAL	
		T_1	T_2	R_{meas}	R_{est}	R_1 %	T_{max1}	R_2 %	$T_{max\,2}$
1969	FEB	12.0	1.06	.028	.021	.015	23.56	.053	00.99
	MAR	12.0	1.41	.029	.021	.024	01.37	.043	00.54
	APR	12.0	1.14	.029	.021	.026	00.22	.051	01.08
	MAY	12.0	1.12	.028	.021	.023	01.02	.050	00.61
	JUN	12.0	1.27	.030	.021	.009	21.87	.048	11.97
	JUL	12.0	1.06	.029	.021	.025	23.26	.055	11.83
	AUG	12.0	0.96	.025	.020	.017	22.90	.053	11.40
	SEP	4.99	1.30	.026	.021	.027	23.64	.042	10.79
	OCT	4.09	1.36	.027	.021	.031	22.51	.042	00.07
	NOV	2.91	2.47	.028	.021	.040	22.21	.029	00.32
	DEC	3.20	0.85	.028	.021	.037	20.60	.064	00.17
1970	JAN	3.86	0.84	.027	.021	.031	19.89	.063	00.54
	FEB	2.17	0.80	.025	.020	.047	17.47	.062	00.58
	MAR	3.23	0.78	.024	.020	.033	17.92	.061	00.61
	APR	12.0	0.72	.020	.021	.013	15.29	.055	00.82
	MAY	12.0	0.99	.022	.021	.016	18.77	.044	01.34
	JUN	12.0	0.84	.020	.021	.017	22.72	.047	01.92
	JUL	12.0	0.77	.021	.021	.016	21.24	.053	02.47
	AUG	12.0	0.79	.024	.021	.017	18.89	.060	02.69
	SEP	12.0	0.74	.026	.021	.015	13.68	.069	02.59
	OCT	12.0	1.13	.028	.021	.023	13.19	.051	02.31
	NOV	12.0	1.15	.029	.021	.025	11.94	.051	02.24
	DEC	12.0	1.88	.032	.021	.016	14.72	.039	03.27
1971	JAN	12.0	2.63	.032	.021	.008	18.57	.033	03.19
	FEB	12.0	1.92	.029	.021	.019	05.29	.034	04.23
	MAR	12.0	1.21	.027	.021	.011	01.39	.046	04.46
	APR	12.0	0.98	.024	.020	.011	23.34	.049	04.48
	MAY	12.0	0.87	.022	.020	.004	17.34	.049	04.20
	JUN	12.0	1.15	.024	.020	.008	16.24	.042	04.41
	JUL	12.0	1.59	.020	.020	.010	12.77	.027	04.12
	AUG	3.58	1.38	.019	.020	.023	06.99	.028	04.30
	SEP	3.21	6.00	.019	.020	.026	08.48	.017	04.62
	OCT	12.0	1.82	.020	.020	.019	12.77	.025	04.85
	NOV	2.67	1.40	.023	.021	.035	11.62	.034	05.35
	DEC	1.49	1.34	.021	.021	.055	11.91	.033	05.76

3.5.2 Atmospheric Effects

All cosmic ray particles detected at sea level are decay products of the primary radiation. Consequently, the atmospheric conditions will have a strong influence on the observed secondary radiation intensity. The effect of the meteorological factors on the muon intensity can be described in the accepted general form by the relationship given by Duperier (1949)

$$\frac{dI}{I} = \beta_1 \delta B + \beta_2 \delta H + \beta_3 \delta T \qquad (3\text{-}21)$$

where I is the muson intensity, B the sea level pressure, H the height of the mean production level for musons and T the temperature in the neighbourhood of the mean production level. The coefficients β_1, β_2 and β_3 are the partial regression coefficients and are referred to as the partial pressure coefficient, the negative temperature coefficient and the positive temperature coefficient respectively.

To understand the physical significance of the atmospheric correction coefficients, a brief discussion of the interaction of cosmic rays with the atmospheric nuclei is necessary.

The primary cosmic ray particle will interact with atmospheric nuclei and this interaction will release secondary particles. Considering the muon component of the cosmic radiation, the effect of the atmospheric conditions on the muon intensity is related to the atmospheric pressure, the altitude of production and the temperature structure throughout the atmosphere. For a muon to be recorded at sea level, it must penetrate the air mass between the production level and the recorder. The intensity therefore will

vary with atmospheric pressure. Increased pressure will enhance the chance of absorption of the particle between production and detection. The pressure coefficient β_1 is therefore expected to be negative.

A second effect concerns the height of the mean production level of secondaries above sea level. The interactions responsible for the muon production takes place around the same mean atmospheric depth measured in g/cm^2, near the Pfotzer maximum. This depth will depend on the atmospheric temperature distribution. The dependence of any isobar layer on temperature follows from the thermodynamics of the atmosphere:

$$\delta H = \frac{1}{g} R_o \ln \frac{B_1}{B_2} \delta T \qquad (3\text{-}22)$$

where H is the height and T the mean temperature of the region between pressure layers B_1 and B_2 when $B_1 > B_2$, R_o is the specific gas constant of air and g the acceleration due to gravity.

The inference of 3-22 is clear; increase of the temperature of the atmosphere up to the production layer will also increase the height of same. Due to the longer path length of muons there will be an enhanced probability of decay and therefore a lower count rate at sea level. Hence $\beta_2 < 0$ and is called the negative temperature coefficient.

A third possibility for an atmospheric effect follows from the π-μ decay. The production of the muons must compete with nuclear capture of the pions ; the outcome depends on the density of the air. The total cross section per unit volume for the capture of the pions decreases with increasing temperature,

resulting in increased muon intensity. The coefficient β_3 is (mostly) positive and called the positive temperature coefficient.

In the following (Table 3-2) a comparison is made of the 4-fold regression coefficients obtained from various muon detectors. To ensure the validity of the obtained coefficients, careful selection of data is necessary. Periods of enhanced primary intensity variations (e.g. Forbush decrease, solar flare increase etc.) and periods of abrupt changes in the detector efficiencies have been excluded. Meteorological data for the correlation analysis of the Mawson muon data were obtained from the Mawson Weather Station, the upper air data being taken from the H 00Z synoptic radiosonde flights. The heights used are the 125 mb isobar levels in geopotential meters and the temperature is the mean temperature between the 100 and 200 mb levels.

TABLE 3-2. 4-FOLD REGRESSION COEFFICIENTS

Telescope and zenith angle	Number of days	Partial bar. coeff. %/mb	Neg. temp. coeff. %/km	Pos. temp. coeff. %/°C
Mawson 0°	1047	-0.133±0.007	-4.41±0.29	0.021±0.014
Mawson 45°	924	-0.127±0.005	-4.97±0.25	0.019±0.009
Mawson 76°	476	-0.109±0.037	-3.46±0.67	0.022±0.021
Hobart UG 0°	432	-0.044±0.002	-0.46±0.13	0.020±0.005

From the results obtained from the sea level detectors at three different zenith angles (Table 3-2) it is apparent that the total barometer coefficient measured over the integrated spectrum of the secondary flux is zenith angle dependent. Although a $\sec\theta$ dependence of the total barometer coefficient of the differential spectrum has been theoretically predicted, a strong variation of the coefficient

of the observed integral spectrum with zenith angle is not expected. The increase of the cut-off rigidity with increasing zenith angle will reduce the pressure dependency of the observed flux at sea level; on the other hand the longer path length at higher zenith angles enhances the probability of decay of secondaries.

Now, considering the partial barometer coefficient, variation of the sea level pressure will have a greater effect on the effective cross section of the atmospheric absorber at obliquely incident radiation than at the vertical direction. Consequently, the zenith angle dependence of the partial barometer coefficient will be a result of the combination of the opposing effects of atmospheric absorption and the increase of the cut-off rigidity. The expected result based on the theoretical calculation of Wada (1960) will be an increase of the partial barometer coefficient for higher zenith angles. In evidence of the present data the net result of the two effects is a slight decrease of the partial barometer coefficient at 76° zenith angle. The statistical accuracy of the calculated coefficients does not permit quantitative conclusions to be drawn. It is interesting to note that the pressure coefficient obtained from the Hobart underground vertical telescope is only about 40% of that of the Mawson high zenith angle pressure coefficient, the cut-off rigidity at production for the two detectors being approximately the same ($\sim$15 GV), the equivalent total absorber being $\sim$40 m.w.e.

Similar discrepancy exists for the negative temperature coefficients of the two detectors, the same being a magnitude smaller

at Hobart underground than the coefficient obtained from the high zenith angle telescope data. This is to be expected, however, as muons recorded underground lose most of their energy in the material absorber above the detector. As the survival probability of muons is a function of energy and of the geometrical length of their path through the absorbing medium, the change of the height of the mean production layer will have little effect on the underground intensity, the path length through which most of the energy loss occurs being very short. Muons recorded at high zenith angles on the other hand will undergo continuous decay in flight, their mean free path and survival probability ever decreasing with increasing atmospheric depth until recorded at sea level.

To prove the validity of the assumption in Chapter 3-2 regarding the off-line coincidences, the total barometer coefficient $\beta = dI/dB$ of the off-line data has been calculated. If the off-line coincidences are composed predominantly of air showers as stated, the total barometer coefficient is expected to be significantly higher than that of the high zenith angle coincidences.

Two time intervals have been selected and the total barometer coefficients calculated for the north, south, vertical and off-line coincidences. The result shows a total barometer coefficient for the off-line coincidence twice that of the high zenith angle coincidences. A large air shower content of the off-line coincidences can thus be assumed. Table 3-3 gives the comparison

of the total barometer coefficients of the various detectors. The probable errors are the $\pm 2\sigma$ limits.

TABLE 3-3. TOTAL BAROMETER COEFFICIENTS (%/mb)

Date	Vertical	North 76°	South 76°	Off-line
29.3-31.5 1968	-0.146±0.002	-0.129±0.003	-0.132±0.004	-0.274±0.011
19.8-22.9 1968	-0.139±0.048	-0.099±0.006	-0.093±0.006	-0.241±0.015

CHAPTER 4

THE HIGH ENERGY COSMIC RAY INSTALLATION AT MAWSON

4.1 The Design of the Experiment

Having established sufficient evidence for the existence of the unidirectional and bidirectional sidereal anisotropies by means of the high zenith angle telescope and other detectors, it became important to obtain more information on the composition, origin, energy dependence etc. of the anisotropies. It has been concluded in chapter 2 that the nature of the modulating mechanism responsible for the anisotropies is very much open to debate. To help in the identification of the number of anisotropies, both solar and sidereal, a co-ordinated experiment has been planned by the Antarctic Division to separate some of the parameters of the phenomena. For this purpose a substantial extension of the Mawson detecting array has been proposed. Particular importance has been attached to high energy (mean integrated response 50 GeV) muon detectors. The location of the station has been fully exploited by taking advantage of both the latitude of observation and the local geomagnetic field to obtain the desired asymptotic direction of viewing.

The optimum geometrical parameters for the telescopes have been calculated by means of a computer program devised by Cooke (1971) which took into account the asymptotic cone of viewing and the differential coupling coefficients to calculate the telescope responses for the given geographic location and magnetic field vector.

To make the data intercomparable with other high energy cosmic ray detector installations, an equivalent depth of 35 m.w.e. for the high energy detector system was decided upon.

Several possible methods for attaining the required mass of absorber above the detector have been investigated. Some of those considered were:

(i) use of metal absorber plates, lead or steel, between or above the counter trays,

(ii) placement of the counter trays behind a suitable rocky outcrop with the appropriate dimensions in the mountain ranges south of Mawson,

(iii) underwater telescopes moored in Horseshoe Harbour,

(iv) excavation of an underground vault to house conventional muon detectors.

The first method was discounted due to the prohibitive cost of such an installation. Logistic problems of a remote installation proved impractical. Although an underwater detecting system would have had certain advantages, i.e. flexibility in the selection of the depth and the uniformity of the absorbing medium, service of the equipment, particularly in the winter season, would have presented great difficulties. The most practical method proved to be the excavation of an underground vault of suitable dimensions to house the detectors. The chosen depth for the underground observatory was 35 feet in the local rock. The charnockite rock of Mawson, composed predominantly of quartz, feldspar and hypersthene with an uniform density of 2.82 g/cm^3 gives an effective depth of approximately 32 m.w.e. for the excavated vault. Because of the permafrost conditions directly below the surface (the annual average temperature of Mawson being $-11^{\circ}C$) seasonal variation of the rock density due to moisture is not expected.

4.2 Location of the Observatory

Ideally, a high energy cosmic ray detector would have an uniform spectral response over its entire geometry of viewing. The absorber material therefore would be of equal thickness in all directions of the telescope aperture. For practical purposes the site of an underground observatory is chosen in such a way as to maintain a constant absorber thickness over the centre region of the direction of viewing. Any departure of the absorber thickness at the edge of the telescope cone from the nominal amount of absorber will have a reduced effect on the observed spectrum as the geometric sensitivity falls off at the periphery of the cone.

For the desired direction of viewing (geomagnetic North) the optimum site of the underground chamber at Mawson appeared to be the ridge running in the south-easterly direction, approximately 200 metres south-west from the station (see locality plan fig. 4-1). During 1970 the seasonal snow deposit of the area was observed and the actual siting of the new observatory took effect after selecting the section of the ridge with the least snow deposit. Over several years of observation it can now be concluded that the extra amount of absorber in the form of snow deposit over the surface area of the viewing cone of the underground telescopes is negligible and will not cause any observable seasonal variations at the present statistical accuracy of observation.

As the Mawson cosmic ray observatory building erected in 1955 reached the end of its servicability as an observatory, during the course of the design of the underground experiment it was decided to erect a new building to house all surface detectors.

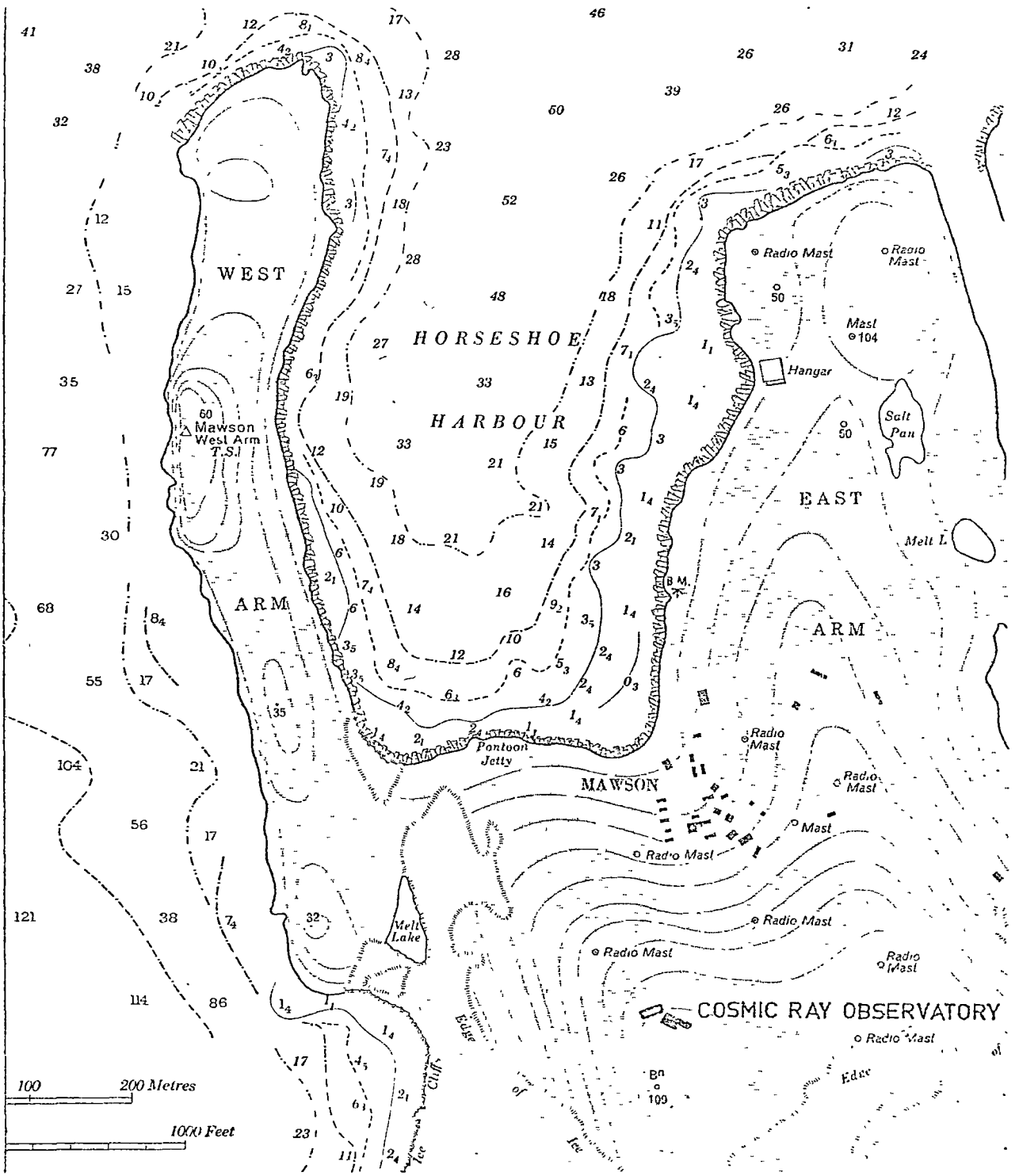

FIG.4-1 LOCALITY PLAN OF MAWSON
COSMIC RAY OBSERVATORY

Because of the simplified maintenance and the possibility of combining the recording apparatus common to both the underground and surface detectors it was an attractive proposition to integrate the two observatories. The underground vault would be connected to the surface building by a vertical access shaft. All detectors could be then connected by internal wiring to a central console eliminating the necessity of duplicated control and recording circuitry. The selected site for the underground vault has also fulfilled the requirements for the surface observatory imposed by the zenith angle of viewing of the high zenith angle telescopes. The maximum angular elevation of the antarctic plateau from the new site is 3.5°, below the viewing cone of the south pointing high zenith angle telescopes. Future development of the station in the south-westerly direction has been restricted to avoid interference to both of the underground and surface detector viewing cones by additional absorbers, e.g. buildings, parked vehicles, fuel storage etc.

4.3 Summary of the Muon Detectors

The installation consists of ten muon telescopes; five at surface level and five underground.

Telescopes M_1, M_2 and M_3 are three identical high zenith angle units. Construction and properties of these telescopes are described in chapter 3. Computer analysis of the telescope geometry has shown favourable trade-off between count rate and directional sensitivity by widening the zenith angle to a lower limit of 61° from the original zenith angle of 68°. To avoid problems associated with near horizontal cosmic ray particles the upper limit of the zenithal opening has been retained at 85.5°.

The change in the geometry is effected by modification of the selected pattern of counter pairs for 3-fold coincidence (Fig. 3-1).

M_4 and M_5 are counter telescopes of standard cubical design as recommended for the IGY network of cosmic ray recording stations. The telescopes are inclined 45° to the zenith and are mounted on turntables to allow programmable azimuth settings in any desired direction. In the present experiment alternate azimuth settings of geomagnetic east and west are employed, the telescopes pointing in the opposite azimuths with respect of each other and are being rotated 180° at the beginning of each GMT hour. This allows the absolute measurement of intensity difference in the two opposite directions using bi-hourly count totals from each of the telescopes. Description of the mechanical design is given elsewhere (Parsons, 1957). The associated electronic circuitry has been rebuilt using semiconductors.

As well as continuing measurements of the E/W asymmetry, the data obtained from the telescopes are used for investigation of the solar diurnal variation. Using the E-W difference in the diurnal analysis, spurious diurnal variations due to atmospheric effects will be eliminated (Jacklyn 1969).

The underground telescopes M_6, M_7 and M_8 are similar in design to the standard cube but have a modified geometry. Each telescope has a total sensitive area of 2 m^2 with 0.5 m between the extreme trays. Output pulses of two different geometries are recorded; for the narrow angle component the telescope is sub-divided into four sub-units and the output of all sub-units are OR-gated to a common output line. The wide angle component is the coincidence rate of the full tray. One unit (M_6) is connected in 3-fold coincidence, the

other two units are in 2-fold coincidence.

Mechanically, the telescopes are designed for fixed azimuth operation (geomagnetic North). The zenith angle is continuously adjustable between 15° and 30° by means of a threaded rod. Provision is made for zenith angle settings outside these limits. The steel framework carrying the counter trays is mounted on wheels and the telescope assembly can be moved laterally on angle iron rails. Due to the confined space in the underground vault this design feature was necessary to facilitate maintenance of the telescopes.

The purpose of the north pointing telescopes underground is the accurate determination of the asymptotic directions of anisotropies. Outside the magnetosphere the telescopes scan the celestial sphere at mid-latitude, viewing parallel to the terrestrial field lines; hence no deflection of the charged particles will occur due to the magnetic field. Geomagnetic displacement of the primary cosmic ray particles is at a minimum (averaging over the cone of acceptance of the telescope) and the observed time of intensity maximum will coincide with the direction of the primary cosmic ray anisotropy. At a zenith angle of 24° the average diurnal amplitude of response will be approximately 65% of the free space amplitude of a typical undirectional anisotropy for primary energies >50 GeV.

If a detector points in a fixed direction in space, no intensity variation will be observed due to spatial anisotropy. The underground telescopes M9 and M10 are designed for zero response to anisotropy. The results are used as a control value for comparison with data obtained from other telescopes which are expected to respond to anisotropies. Any residual daily periodic response

of telescopes M_9 and M_{10} will indicate effects of atmospheric origin.

Ideally, telescopes M_9 and M_{10} should point in a direction parallel to the rotational axis of the earth. Because of the finite solid angle of the telescopes and the difference in the asymptotic direction throughout the differential energy spectrum the fixed direction of viewing in space can only be approximated. The final zenith and azimuth settings for the telescopes has been obtained by integrating the contribution of each telescope element throughout the observed energy range and adjusting the direction of setting until the desired asymptotic direction centered at the pole has been attained. An effective lower primary rigidity of 35 GeV has been assumed for the given depth (see asymptotic directions in Appendix).

Mechanically and electronically the telescopes M_9 and M_{10} are similar to the underground north pointing telescopes. In addition to the zenith angle adjustment, setting of the azimuth of the telescopes is provided by mounting the framework on circular rails. Semi-cubical geometry of 1x1x0.5 m gives the optimum in count rate and direction of viewing.

The detectors in the new observatory are summarised in Table 4-1.

4.4 Installation of the Observatory

The excavation of the vault commenced during 1971. It was planned to erect the new observatory building and install all detectors in the Summer of 1971-71. Adverse weather conditions delayed the beginning of the building program until December 1971. Reconstruction of all electronic circuits of the detectors transferred from the old observatory caused further delay in the

TABLE 4-1. SUMMARY OF COSMIC RAY DETECTORS AT MAWSON OBSERVATORY

TELESCOPE	NUMBER OF UNITS/SUB-UNITS	GEOMETRY	ZENITH ANGLE	AZIMUTH ANGLE	TRAY ABSORBER	COINCIDENCE	COMBINED MEAN HOURLY COUNTRATE	OBSERVATIONAL FEATURE
MESON SURFACE:								
High Zenith Angle M1 M2 M3	3/29	(1x0.16)x1m	72°	0°	13cm Fe	3-fold	45 000	Equatorial viewing
	3/29	(1x0.16)x1m	72°	180°			45 000	Transverse to Earth's magnetic field
Inclined * rotatable M4 M5	2	(1x 1)x 1m	45°	60°	10cm Pb	3-fold	150 000	GM East E/W assymetry
				240°			150 000	GM West
MESON U/G.:								
North M6 M7 M8	3/4	(1x0.5)x0.5m	24°	330°	NIL	M6 3-fold M7 M8 2-fold	174 000	Parallel to Earth's magnetic field
	3	(1x 2)x0.5m	24°	330°			300 000	
South-West M9 M10	2	(1x 1)x0.5m	30°	200°	NIL	M9 2-fold M10 3-fold	78 000	Parallel to Earth's rotational axis
NEUTRON: 12 MN	3	12 counter pile (I.G.Y.)					40 000	Nucleonic component Solar flares etc.

* converted for Jupiter observation Mar.1974

completion of the installation. The new observatory has become operational in early 1973.

The excavation was carried out by conventional tunneling methods using explosives. The spoil from the excavation has been deposited on the surface above the vault, filling in natural depressions in the area. When all blasting operations were completed, work proceeded to erect the scaffolding to carry the floor beams of the building. To avoid deposit of snow drift around the building the floor has been elevated to allow free passage of drift snow, a common building practice at antarctic locations. After installation of the floor and casting of the concrete piers for the telescopes and the dwarf wall of the access shaft, the prefabricated building was erected (pictures 4-2, 4-3 and 4-4).

To prevent surface water reaching the underground detectors through the shaft, the roof and walls of the vault have been sealed with plastic sheeting. Then the vault was timber framed and lined with heat insulating material and fire resistant asbestos sheeting. Next the telescope rails were set in the rock and the vault completed by laying the floor boards. A sump was excavated at the bottom of the access shaft to collect seepage water in summer and an automatic sump pump installed to expell the accumulated water to the surface.

Signal and power lines to the telescopes are placed in cable ducts recessed in the floor of the building. To protect the connecting wires to the underground telescopes a cable duct was installed connecting the observatory building to the underground vault.

Temperature control of both the surface observatory and the

vault is effected by thermostatically controlled electric heaters. Although temperature control of the vault proved to be satisfactory with heaters alone, in addition, for the surface observatory, a cold air inlet system, similar to that installed in the old observatory, had to be added to overcome summer overheating problems.

Over the number of years the observatory has now been in operation the performance of the detectors appears to be satisfactory. Apart from routine testing and counter replacement in the telescopes the continuity of observation has been retained to date and no major breakdown in the circuitry has been reported.

Pictures 4-5, 4-6 and 4-7 show part of the underground detecting system, interior of the observatory building and the recording console.

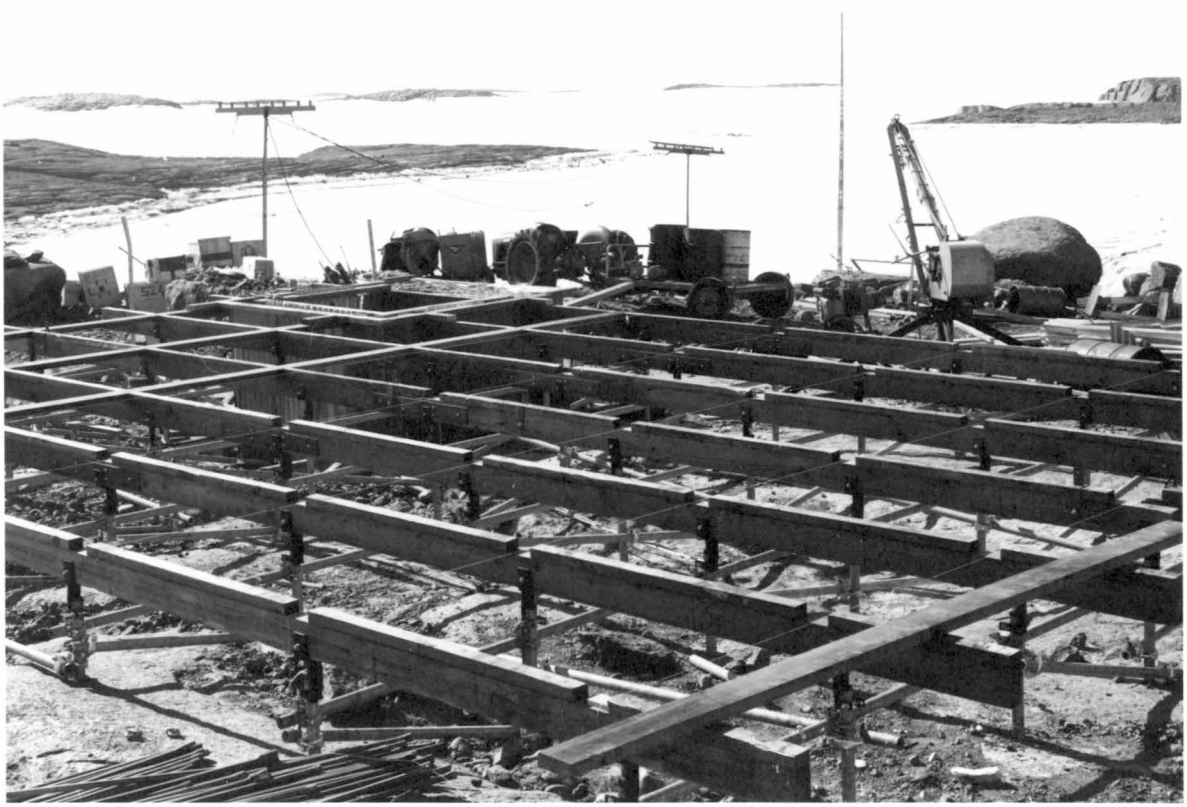

Fig.4-2 The elevated platform of the surface observatory under construction

Fig.4-3 Construction of the underground vault access shaft

Fig 4-4 Construction of the surface observatory

Fig.4-5 Underground telescopes

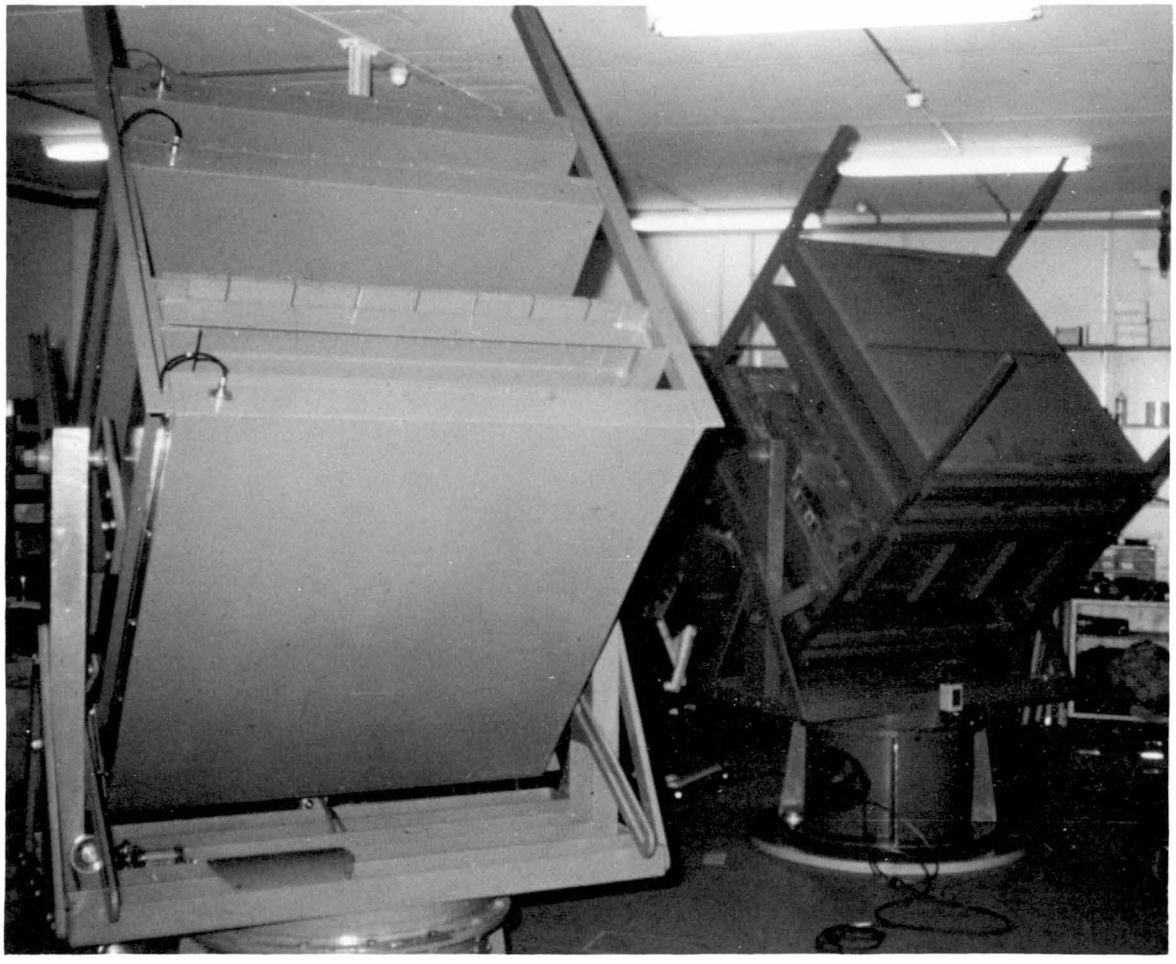

Fig.4-6 Interior of surface observatory

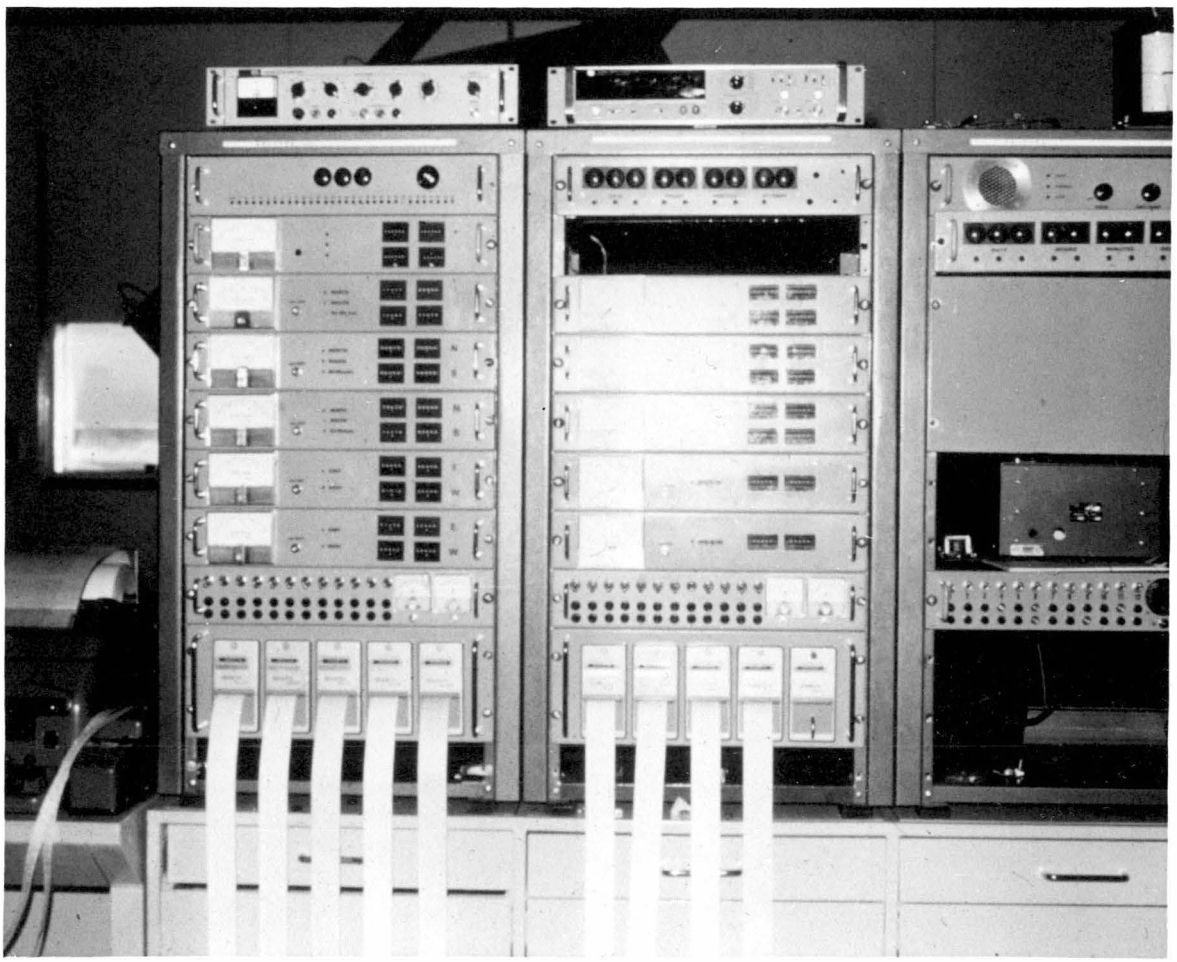

Fig 4-7 Data recording system

CHAPTER 5

ELECTRONIC CIRCUITRY

5.1 Design Philosophy

One of the objectives of the present work was to develop a battery operated solid state electronic recording system to replace the previously used vacuum tube electronics which relied on mains power for its operation. The shortcomings of mains operated equipment at remote stations with often unreliable power generating systems manifested itself in many hours of data lost. Solid state circuitry, on the other hand, offers the advantage of low power consumption and therefore capability of battery operation, together with increased reliability. Routine replacement of components e.g. valves is eliminated and therefore maintenance time during which the equipment is non-operational, is minimized.

In the early stages of the design work transistors were used as active elements in the electronic circuit design. With the rapid development of the integrated circuit technology it has become more convenient and economical to employ integrated circuits in the circuit design, reducing construction time and enhancing reliability. Integrated circuit compatibility has been a major aim in the design of the electronic recording circuitry of the new observatory and, next to new IC designs for some of the earlier transistor circuit units, the remaining transistor pulse circuits were modified for the now widely accepted TTL logic levels where practicable.

Another advantage of circuit design with IC components is the relative ease with which complex circuit functions can be realized in small space and good economy. It has thus become feasible to

automate the data recording section of the detectors relieving the operator of the task of manual data collection. This feature has become especially important with the increased number of detectors in the new observatory.

The block diagram in fig. 5-1 outlines the operation of the electronic circuitry. Following common practice in cosmic ray detecting systems each detector is provided with a separate and independent EHT supply. Any change in the counting efficiency of the counters due to drift in the high voltage supply therefore can be traced by intercomparison of the count ratios of different telescopes.

The electronic circuitry can be broadly divided into three groups, i.e. the telescope electronics, the recording electronics and the auxiliary electronic circuits. Other electric and electronic circuits not directly related to cosmic ray recording, such as observatory temperature control etc. have been described in Chapter 4 as part of the installation.

5.2 Telescope Electronics

The telescope electronic circuits consist of the geiger-pulse amplifying and shaping circuits (tray circuits) and the AND gates responsible for the selection of the appropriate coincidences between the various counters.

The pulse amplifier is a single stage inverting overdriven amplifier. The discharge current from the geiger counter rapidly activates the transistor and causes a fast rise-time positive going signal at the collector. The pulse at the collector output is differentiated and the leading positive edge is used to trigger

a monostable multivibrator.

Because of the large number of multivibrator circuits required in the telescopes M1 M2 and M3 a monostable multi with low standby current is employed. The circuit consists of a complementary pair of transistors (fig. 5-3). In the quiescent condition both transistors are biased off. Upon receiving the trigger pulse the npn transistor will turn on. The collector voltage goes negative hence turning the pnp transistor on. The collector of the pnp transistor is coupled to the base of the npn transistor via the timing capacitor thus holding the npn transistor on for the duration of the charging cycle. The time constant of the circuit can be adjusted with the trimpot between 0.5 µs and 5 µs. At the end of the pulse the timing capacitor will rapidly discharge through the collector resistor of the pnp transistor and the diode into the negative supply. Pulse recovery time of the circuit is less than 1 µs. The negative pulse of the collector of the npn transistor is fed to the coincidence circuit via an emitter follower.

The monostable multivibrators for telescopes M4...M10 (fig. 5-2) consist of cross coupled RTL NOR gates. The operating voltage of 3.9V is derived from a Zener diode shunt regulator from the -6V line. The pulse length is set at 1.8 µs by the 1 nF timing capacitor and the 2.7 k resistor. The negative output pulse is amplified and inverted to produce a positive tray circuit output pulse for the coincidence circuit.

The coincidence circuit is responsible for the selection of the appropriate counter output pulses corresponding to the passage of an ionising particle within the viewing cone of the telescope.

The original coincidence circuit of the high zenith angle telescopes M_1 M_2 and M_3 selected coincidences in the following configurations (see fig. 3-1):

$$N = N_1 + N_2 + \ldots + N_{30} = A_1 \cdot B_1 \cdot C_2 + \ldots + A_{30} \cdot B_{30} \cdot C_{31}$$

$$S = S_1 + S_2 + \ldots + S_{30} = A \cdot B \cdot C + \ldots + A_{32} \cdot B_{30} \cdot C_{30}$$

The recording of the off-line coincidence discussed in chapter 3.2 has been discontinued in 1969.

The coincidence gates are 3-input diode gates (Fig. 5-4). The input diodes are normally conducting, lifting the nodal point to ground. The first transistor is biased into conduction through its base resistor, hence cutting the second transistor off. Simultaneous negative pulses at the appropriate gate inputs will saturate the output transistor and a low impedance negative output pulse will result. As a measure of air shower particles the coincidences between the NORTH and SOUTH outputs are also measured.

The purpose of the local voltage regulator for the -6 V line is the elimination of electrical noise generated along the -12 V supply line connecting the telescope to the remote power supply.

The modified wide angle configuration of telescopes M_1 M_2 M_3 require the following gating of the counter pair pulses:

$$N' = N'_1 + N'_2 + \ldots + N'_{29} = (A_1 + A_2) \cdot (B_1 + B_2) \cdot C_3 + \ldots (A_{29} + A_{30}) \cdot (B_{29} + B_{30}) \cdot C_{31}$$

$$S' = S'_1 + S'_2 + \ldots + S'_{29} = A_4 \cdot (B + B) \cdot (C + C) + \ldots A_{32} \cdot (B_{29} + B_{30}) \cdot (C_{29} + C_{30})$$

The circuit is realized using integrated circuit DTL gates (fig. 5-5). Because of the negative output pulse of the geiger pulse amplifier circuits, input signals to the coincidence circuit have to be inverted. The OR-gating of the combined counter pair outputs for the three-fold coincidence inputs is achieved by using positive logic

NAND gates in a negative logic circuit function according to the relationship

$$\overline{\overline{A} \cdot \overline{B}} = A + B$$

Output pulses from the coincidence gates for each direction are added by tying together all output signals of the NORTH and SOUTH gates respectively. The negative coincidence pulses are amplified through the output emitter followers.

The coincidence circuits for M_4, M_5, M_9 and M_{10} are self explanatory. The fourth input to the diode AND-gates for the rotating telescopes M_4 and M_5 are held at -6 V for the first minute of every G.M.T. hour thereby inhibiting the recording of coincidence pulses during the rotation of the telescopes. Telescope M_9 operates in two-fold coincidence. The middle tray input is permanently enabled by connecting it to ground.

Each tray of the underground north pointing telescopes M_8, M_9 and M_{10} is sub-divided into four 12 counter sections A_1, A_2, A_3, A_4, B_1, B_2, etc. for coincidence purposes. The narrow angle coincidence is derived from the configuration.

$$N_{narrow} = A_1 \cdot B_1 \cdot C_1 + A_2 \cdot B_2 \cdot C_2 + A_3 \cdot B_3 \cdot C_3 + A_4 \cdot B_4 \cdot C_4$$

and the wide angle coincidence is

$$N_{wide} = (A_1 + A_2 + A_3 + A_4) \cdot (B_1 + B_2 + B_3 + B_4) \cdot (C_1 + C_2 + C_3 + C_4)$$

Telescopes M_7 and M_8 are operated in two-fold coincidence. The middle tray inputs are enabled for both the narrow angle and wide angle coincidence gates by grounding the input pins (fig. 5-7).

5.3 Recording Electronics

To obtain muon intensity values for analysis, the coincidence output pulses have to be counted and stored in a compatible form

for data analysis.

In the present system four-fold recording of the data is employed (see fig. 5-1). The primary data recorder has its data output in a perforated tape format, obtained from a Siemens teleprinter. For the operator's convenience a hard copy print-out of the data is also produced. The punched tape is directly compatible with the international telegraph code and can be transmitted by Telex without any further modification.

The teleprinter is controlled from the ADR (automatic data recorder) unit. The output contains all hourly section totals from all recorders. Sufficient number of spare recording channels are provided to record additional information such as hourly mean pressure, wind speed and direction, etc.

A set of Sodeco electro-mechanical printing registers provide back-up for the ADR. Outputs from telescopes recording from the same direction are added together and the directional hourly totals are recorded on individual printing registers. The data output from the printers are used mainly for manual data analysis at the station.

For day-to-day efficiency calculations of the detectors two master registers have been included for each telescope. Each register records the daily count totals on alternate days. During every GMT day, therefore, the count totals of the previous day are stored and accessible to the operator for daily assessment of the telescope efficiencies.

The fourth mode of data recording consists of an event recording chart recorder. On this, every n-th count from each recorder is recorded on a chart moving at a constant speed. Additional time

marks are recorded on the first channel. The scaling factor n is chosen for optimum chart readability of each telescope output.

The count rates of the muon detectors are in excess of the maximum pulse rate of electro-mechanical registers. An electronic scaler is therefore used to reduce the number of pulses to be counted. Suitable choice of the scale factor will have no detrimental effect on the counting statistic, as will be shown in chapter 6.

The scaling circuit for the muon telescopes consists of a number of cascaded bistable multivibrators (flip-flops), followed by a monostable multivibrator with an output pulse length of 50 ms. Dividers of the earlier design are collector-base coupled transistor multivibrators (fig. 5-8). The later design uses integrated circuit binary dividers as scaling units (fig. 5-9). The scale factor 2^n can be selected by inclusion of the appropriate number of FF units in the dividing chain, and its choice depends on the count rate of the detector. The 50 ms output pulse of the monostable multivibrator is amplified via the output buffer (fig. 5-11) to TTL levels before being distributed to the four independent recording systems.

The ADR unit consists of a number of temporary data storage registers (CSB 11) and read-out display (fig. 5-14), channel selector switch (fig. 5-16), the code converter and teleprinter control circuitry (fig. 5-15) and the 40 mA current source (fig.5-28) to operate the Siemens 100 type teleprinter.

The pre-scaled coincidence pulses from each buffer board outputs are registered in a three stage decade counter in BCD code. The most significant bit of the "hundreds" digit is not connected

to the output as the maximum hourly scaled count does not exceed 800 for any detector. It can be connected externally as an overflow indicator. The "hundreds" digit being a binary counter, it will extend the capacity of the register to 1600 for test purposes.

At the end of the hourly recording interval the content of the counting registers is stored in a 12 bit latch until readout of all information is completed. The transfer gate pulse, which locks the information into the latch circuit, also clears the counters on its leading edge and the counters are now ready to receive new information. The propagation delay times through gates G15 and G16 are sufficiently long to store the content of the counting register in the latch circuit before the former is reset.

The content of the appropriate latch circuit will appear on the common data bus when the "output enable" line for the data register being interrogated goes "low" and output gates G1...G12 are enabled. The read-out displays the momentary data appearing on the output bus line.

Outside print-out interval the data channel to be displayed is selected with the manual channel selector switch by grounding the appropriate "output enable" line. When print-out of information takes place, the manual channel selector switch is disabled and the 30 data register latches are sequentially interrogated by the data channel selector.

The data channel selector is a 32 position electronic switch, using two 1-of-16 decoders as switch elements (fig. 5-16). The two decoders are driven parallel by a 4 bit binary counter. A RS flip-flop comprising of gates G1 and G2 selects switch positions 1 ...16

and 17...32 respectively. Normally, the input of the inverter G3 is "high", both decoders are disabled through inputs E_1. The binary counter is held in the cleared state and FF G2 is "high". All decoder outputs are biassed off and the manual channel selector has effective control of selection of the data channel to appear on the visual read-out.

At the commencement of the print-out sequence input to G3 goes "low"; the binary counter and the first decoder (1...16) is enabled and clocking the binary counter, decoder outputs 1 to 16 will successively go "low" (active) and selection of data registers 1 to 15 will occur in sequence. On the trailing (negative) edge of the 16th clock pulse output D of the binary counter changes from "high" to "low" state. The negative transition coupled to the input of G1 will change state of FF G1G2 thus disabling the first decoder and enabling the second one. Further clock pulses will select data channels 16 to 30 to the data bus line. Switch position 1 and 16 are reserved for carriage return, line feed and figure shift operations, switch positions 2 to 15 and 17 to 32 correspond to data channels 1 to 30.

Code conversion and timing control of channel selector clock pulses take place in the code converter and teleprinter control circuit. The circuit operates in the following manner (fig. 5-15):

The active low 1.sec/h control pulse at pin 3 activates the teleprinter by delivering an approx. 20 ms starting pulse to the output amplifier driving the current source through gate G1 and inverters I4 and I3. Data transfers from the registers to the latch circuits are disabled through G7 and the following amplifier. The trailing edge of the hourly control pulse is synchronized with the

50 Hz clock pulse train at G2. When synchronization occurs, FF comprising of G3 and G4 is set and the circuit is activated by enabling the code converter at E_1 and the equivalent 8 bit shift register made up from the 4 bit binary counter 7493 and the 8 bit multiplexer T163. At the same time, the manual channel selector is disabled through transistor 2N3644 and the first character from the bus line is gated into the code converter via gates G13 to G16. Successive clock pulses in 20 ms intervals will now advance the shift register and the BAUDOT character present at the code converter output will be transmitted in serial form to the teleprinter current source. (for information concerning the International Telegraph Code No 2 see Instruction Manual for Model 100 S&H Teleprinter, Australian Post Office Engineering Instruction, 1963).

After transmission of all eight bits of the first character, the second character on gates G17 and G20 will be converted and transmitted, etc. For better readability of the typewritten page, a space character is included between each group of digits representing the content of one data channel. The space character is derived directly in BAUDOT code at the output of G6 in the appropriate sequence. The transmitted characters in the first and sixteenth position of the data selector switch comprise of "figure case", "carriage return" and "line feed" characters, the BCD equivalent of which are produced by the diode matrix circuit connected to the input gates G13 to G24.

After the sequential interrogation of all data channel buffers in use, FF G3 G4 will be reset through G8 by the trailing (positive) edge of the appropriate register enable pulse, provided the 1.min/H00

input of pin 1 is "low". If pin 1 is "high" (i.e. at hour 24) the reset pulse will be inhibited by G9 and 16 further "line feed" characters will be output. At the 16th character FF G11 G12 will be reset by the negative edge of the D output of the binary counter 7493. The differentiated output of G11 will reset FF G3 G4 via G9 and G8 and the system comes to rest.

The Sodeco printing registers add the individual count rate of similar telescopes and directions. The driving circuit is a true adder, i.e. input pulses of each of the three inputs are individually counted. Simultaneous pulses at 2 or 3 inputs will therefore be counted as 2 or 3 events and no data will be lost due to input dead-time.

The incoming pulses of the printer driver (fig. 5-12) are stored in the temporary latches of G1 G2, G3 G4 and G5 G6 for inputs 1, 2 and 3 respectively. The first multivibrator, receiving the input pulse through G9, will energize the count solenoid of the printer through the two stage transistor amplifier and then will be inhibited for a further 50 ms by the second monostable to ensure complete recovery of the counting mechanism. Selective resettings of the latch circuits occur through inverter I4 at the trailing edge of the first monostable pulse. If gates G1 and/or G3 are in the "high" state, the reset pulse to G5 G6 will be inhibited through G11. A similar condition will exist to latch G3 G4 with respect to G1. The three input latches therefore will be reset in succession, enabling the recording of all three inputs.

The count pulse is also inhibited during the print-out and reset operations through G8 and I5. The input latch circuits, however,

can still record one pulse each during these intervals. Counting of the stored pulses will occur immediately after reset.

The control circuit for the printing registers provides the appropriate pulses to the reset, paper advance and print solenoids with the specified intervals between the operations. Hourly printouts for each GMT day are separated by approximately one inch of blank tape by pulsing the "paper advance" solenoid only. Gating of the solenoid pulses can be derived on the basis of fig. 5-13.

The selection of the appropriate master registers by the selector circuit of fig. 5-10 is controlled by the chronometer. The transistor matrix, activating the register driver transistors, gates the count pulses to the appropriate registers corresponding to the day of recording (all telescopes) and the azimuth setting (M_4 M_5). The master registers are cleared manually each day by the operator after reading the daily totals for each telescope.

The event recorder provides a further back-up system to other recorders. A 20 channel Esterline Angus event recorder with mechanical chart drive is used. Driving circuit for the pen solenoids is given in fig. 5-27.

5.4 Auxiliary Electronic Circuits

5.4.1 Power Supplies

The +6 V and -12 V power supplies of fig. 5-21 and fig. 5-22 are conventional series regulated voltage sources featuring a current limiter as a safeguard against accidental short circuits. The -12 V supply, in addition, has an extra protection circuit, which turns the series element off in the case of unduly high mains voltage input, thereby avoiding thermal run-away of the power transistors.

The overvoltage protection circuit samples the unregulated DC voltage through a zener diode. If the rectified voltage rises to a value corresponding to 280 volts AC mains voltage, the control transistor will turn the regulator off until the mains voltage returns to normal. To ensure the fully charged state of the floating stand-by batteries, the voltage outputs are set to +6.6 V and -13.2 V for the two low voltage supplies respectively.

The HT supply produces the voltages necessary for the operation of the high voltage display tubes, the neon indicator lights and the E.A. event recorder pen solenoids. A simple DC-DC converter of symmetrical design operating at approx. 2kHz converts the low voltage to a series of high voltage outputs. The high frequency of operation and the rectangular waveform ensures small physical size and high efficiency of the converter. The +200 V output is both load and line regulated, the +100 V is line regulated and the -35 V line for the driving of the recorder pens is unregulated (fig. 5-24).

The converter section of the EHT supply for the geiger counters is similar to that of the HT supply (fig. 5-23). Bifilar winding of the transformer primary windings ensures reliable starting characteristic. The square wave output voltage of 1000 volts (for 12 V input) is voltage doubled and rectified. The error signal for the regulator is obtained from the high stability resistor chain and applied to the DC amplifier which in turn controls the input voltage to the converter through two emitter followers. A stable reference voltage is derived from a reference diode with zero temperature coefficient through which a constant current is passed.

5.4.2 Chronometer and Timing Unit

Timing of all control functions are governed by a crystal controlled chronometer. A 1 MHz square wave, produced by the crystal oscillator (fig. 5-17), is divided by a suitable divider chain to obtain the time code in BCD form (fig. 5-19). The time is displayed on a 9 digit numerical indicator (e.g. days, hours, minutes and seconds). Initial setting up of the time display occurs through individual setting of the digits by means of the "set time" microswitches. Depression and release of the debounced microswitch will advance the appropriate digit by one. The "seconds" digit is set by means of the variable frequency oscillator (fig. 5-18). The crystal oscillator is disconnected, and the third decade of the main divider receives its input from the manually adjustable VFO. When the chronometer is synchronised with the time signal (received from WWV), the divider is switched back to the crystal oscillator.

The time mark decoder (fig. 5-20) generates all necessary timing pulses for the recording electronics by appropriate decoding of the BCD time code of the chronometer. The correct voltage levels for the various control pulses are established in the pulse amplifiers.

The solid state motor switchgears (fig. 5-26) for rotation of telescopes M_4 and M_5 are also controlled by the time mark decoder. To avoid incorrect azimuth sequence for the rotating telescopes due to temporary rotation failure (e.g. power break-down), an azimuth position feed-back signal, the logic level of which is controlled by a microswitch on the telescope turntable, is EXCLUSIVE-OR gated with the "hour" information of the chronometer. The EXCLUSIVE-OR

gate for telescope M_4 is comprised of gates I12,G2,G3, for telescope M_5 those of I24,G4,G6. If either telescope is in the incorrect azimuth setting due to rotation failure, the rotation initiating pulse will be inhibited at the beginning of the next hour and therefore the telescope will resume its correct azimuth setting automatically.

A low power (5 Watts) 240 V AC power supply with stable frequency of 50 Hz is included for energising small synchronus motors such as wall clocks, chart recorders etc. The 50 Hz square wave is filtered through the twin-tee network (fig. 5-18) and amplified by a push-pull amplifier (fig. 5-25).

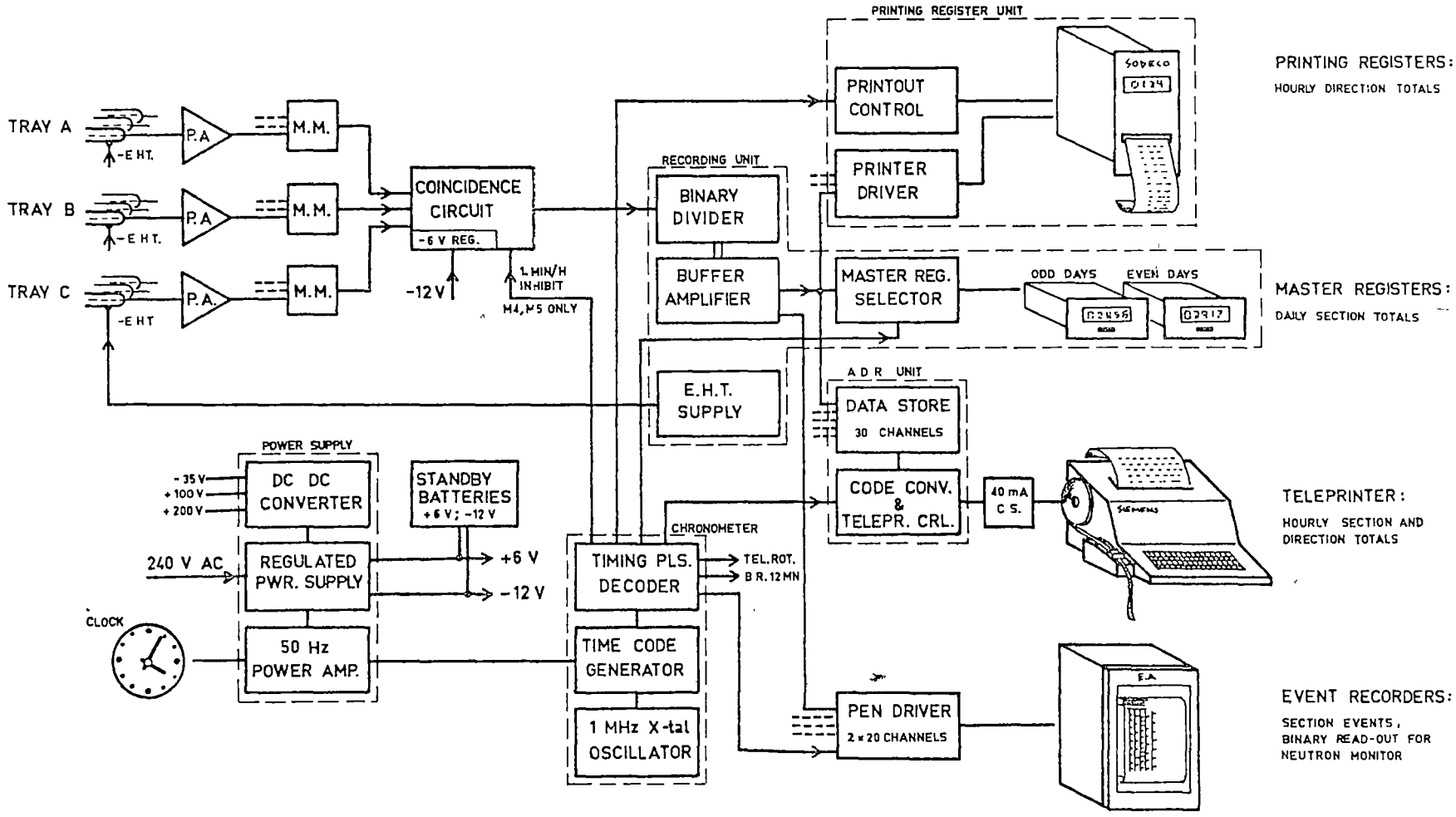

FIG. 5-1. RECORDING ELECTRONICS — BLOCK DIAGRAM.

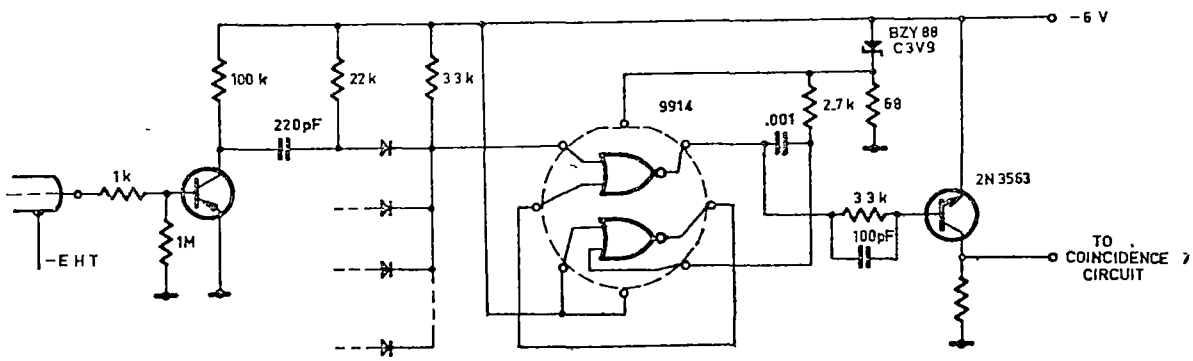

FIG. 5-2. GEIGER PULSE AMPLIFIER (TRAY CIRCUIT) FOR M4 . M10.

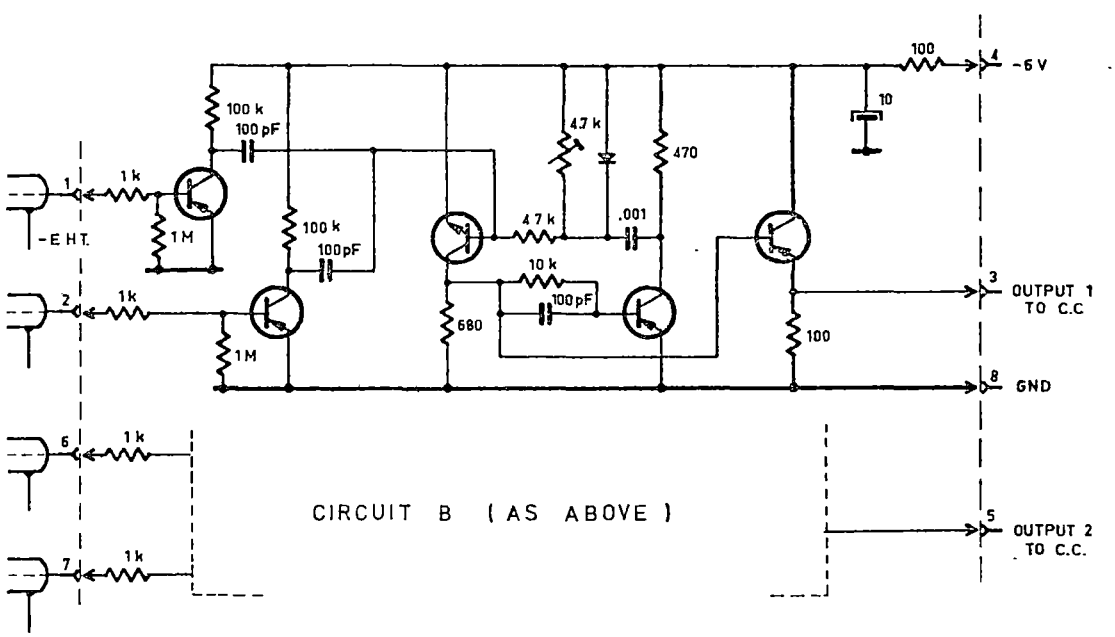

FIG 5-3 GEIGER PULSE AMPLIFIER G.P.1 FOR M1 .M3.

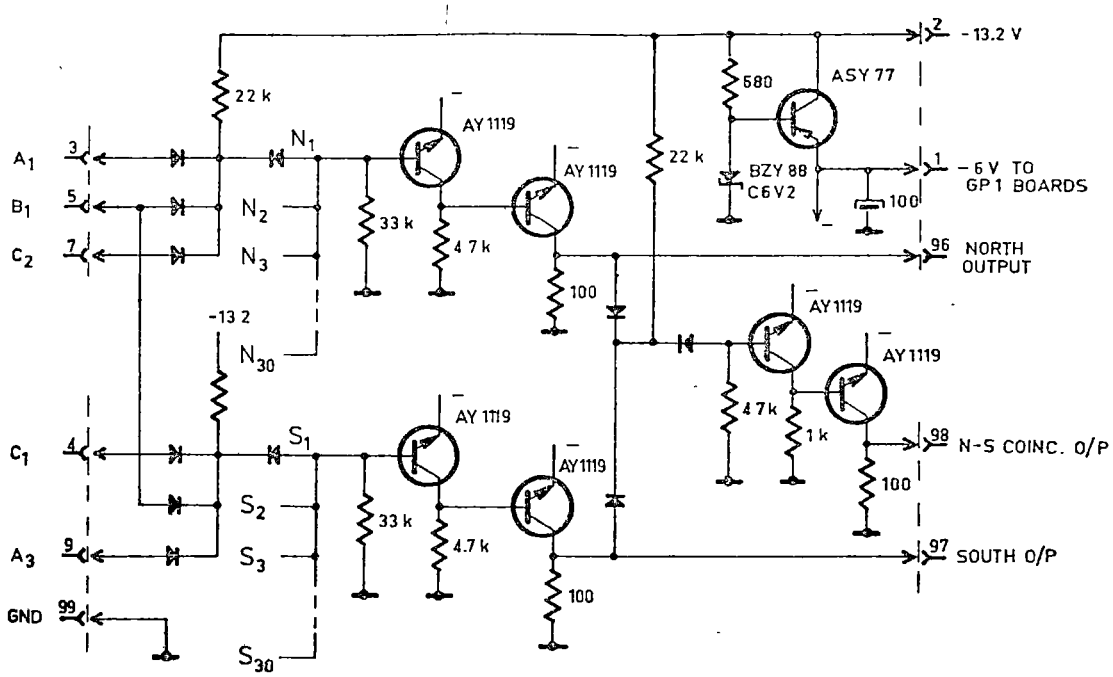

FIG. 5-4 COINCIDENCE CIRCUIT M1 .M3
NARROW ANGLE

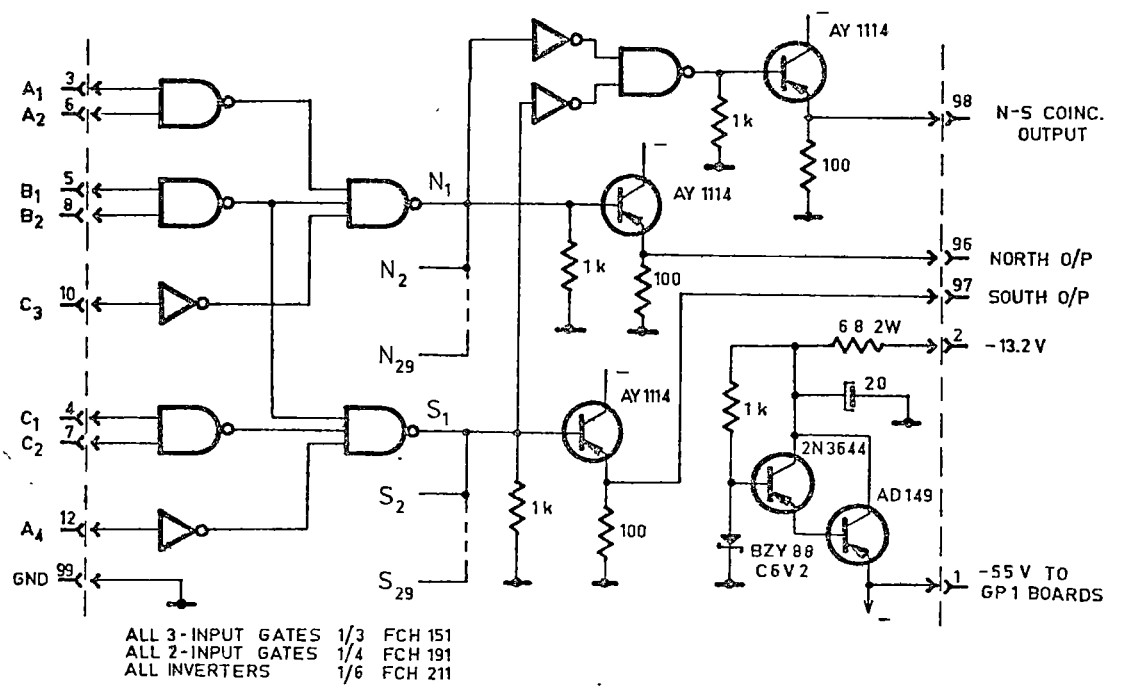

FIG 5-5 COINCIDENCE CIRCUIT M1... M3
WIDE ANGLE

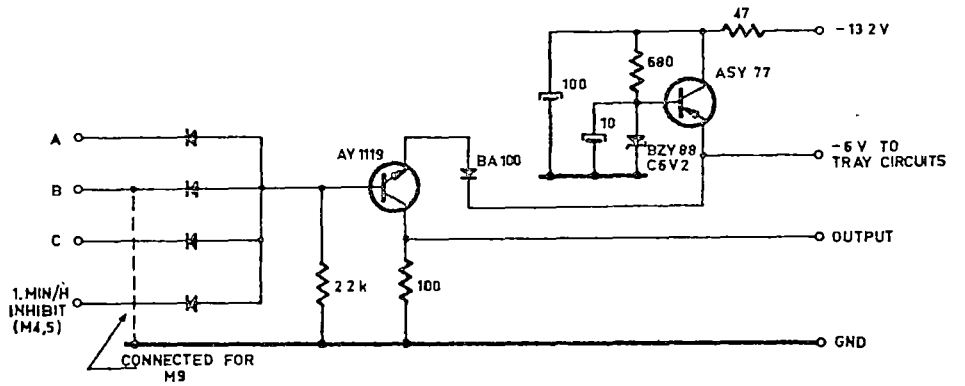

FIG. 5-6. COINCIDENCE CIRCUIT M4, M5, M9, M10.

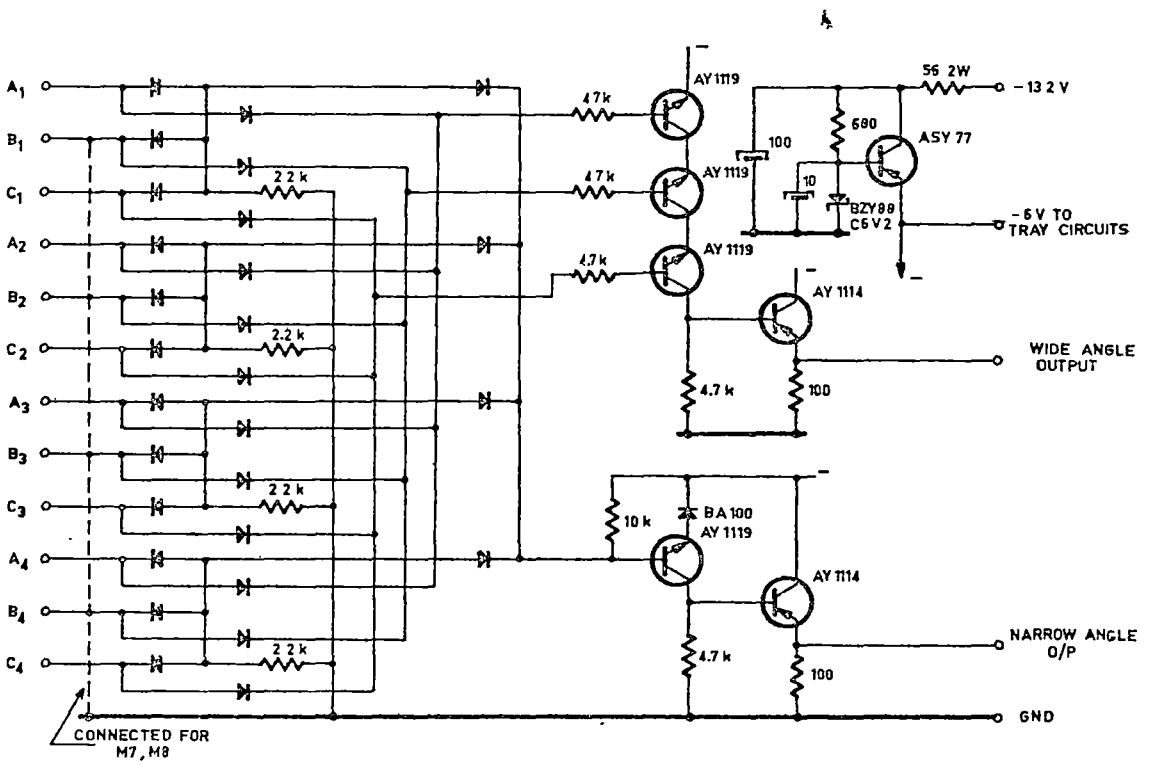

FIG 5-7. COINCIDENCE CIRCUIT M6 . M8.

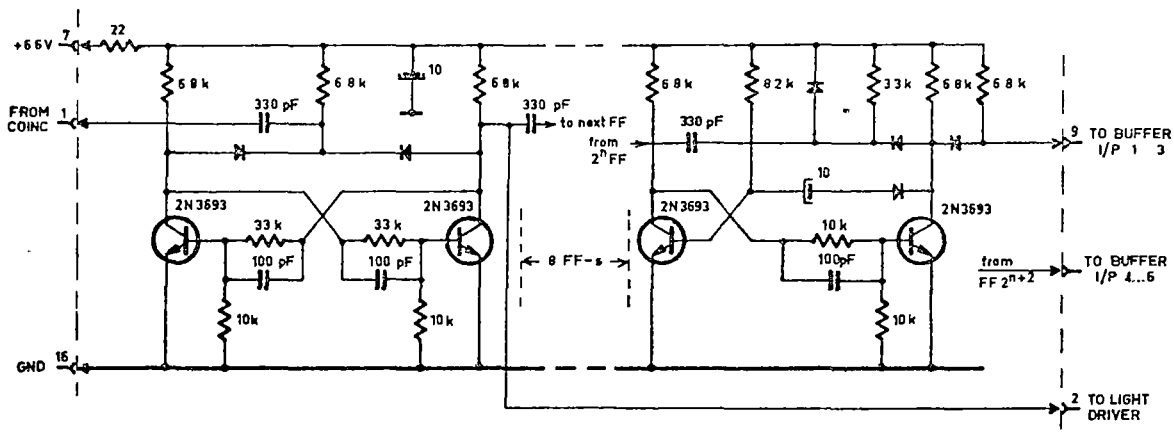

FIG 5-8. BINARY DIVIDER 1.

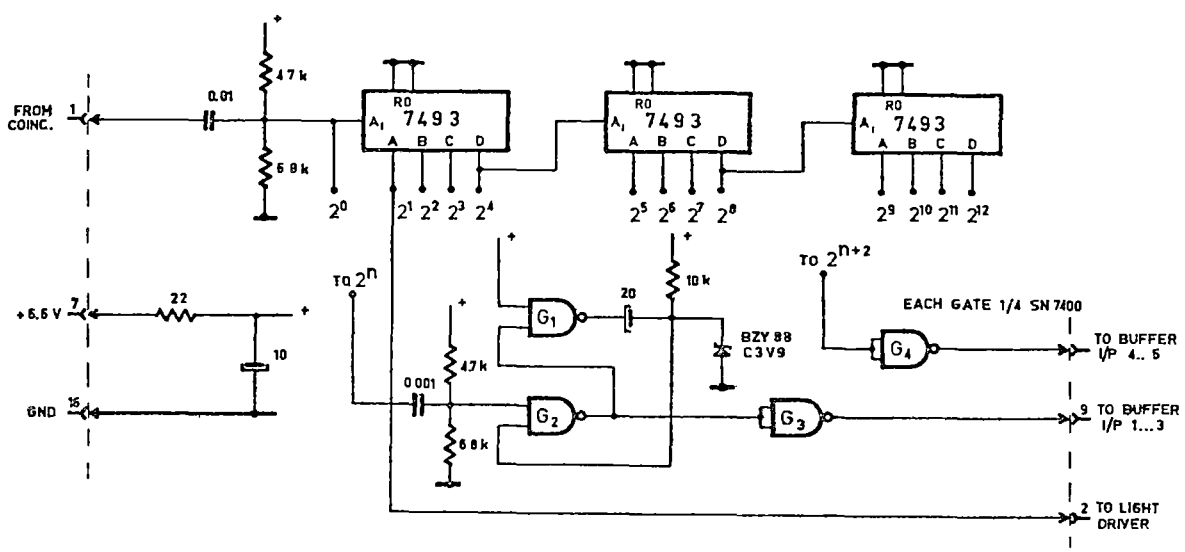

FIG. 5-9. BINARY DIVIDER 2

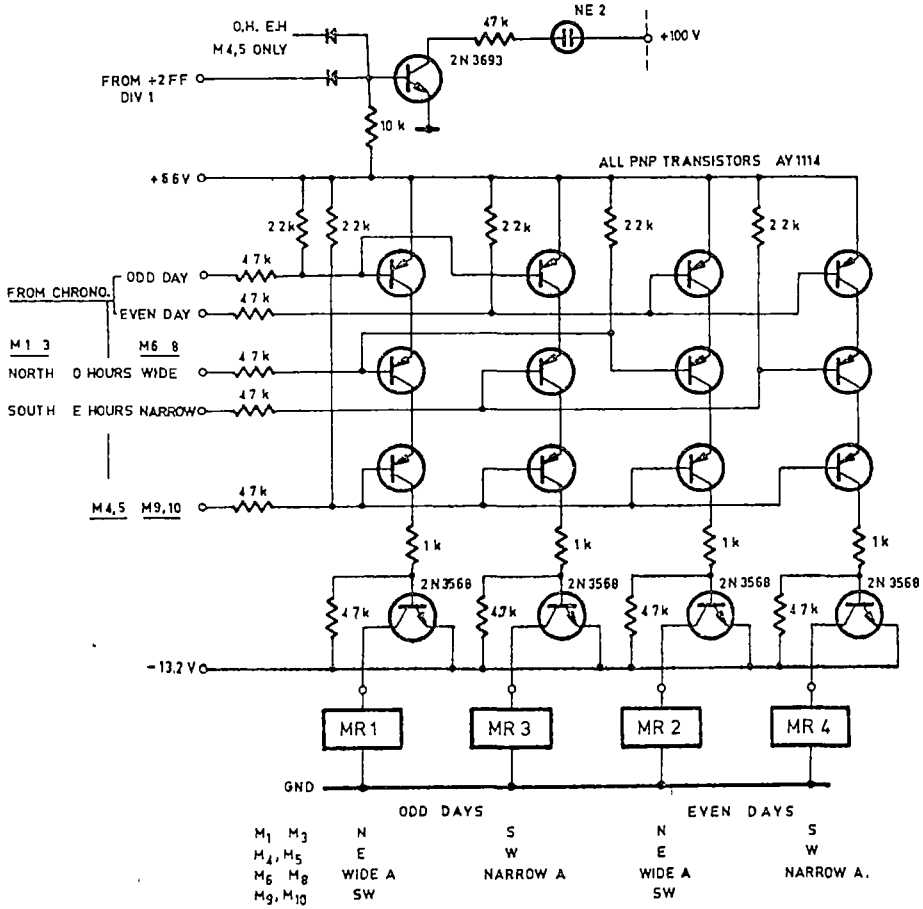

FIG 5-10 MASTER REGISTER SELECTOR AND INDICATOR LIGHT DRIVER

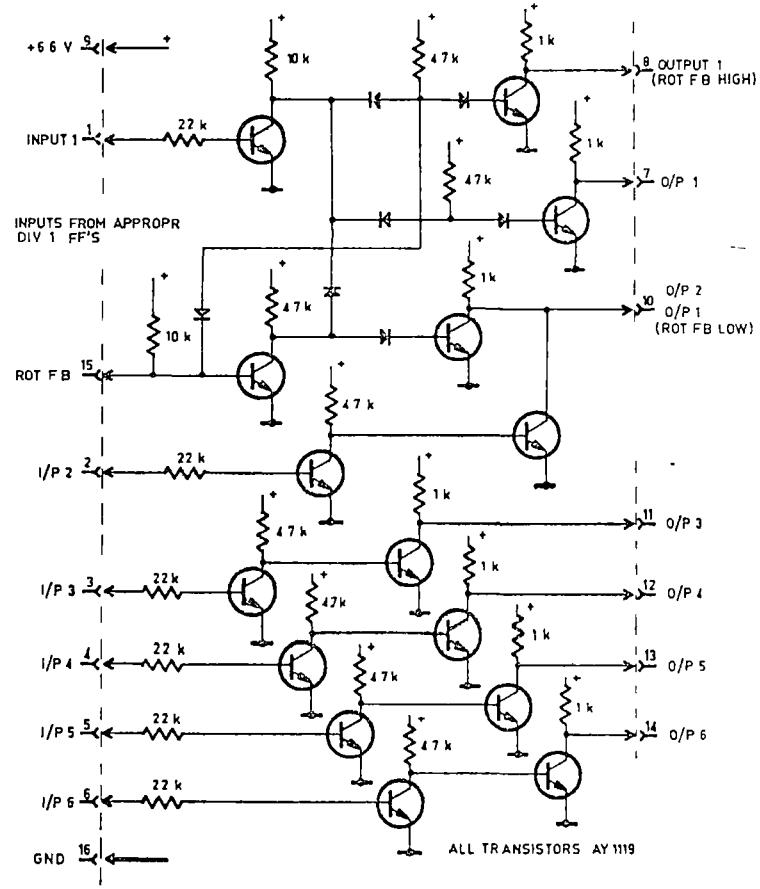

FIG. 5-11 OUTPUT BUFFER

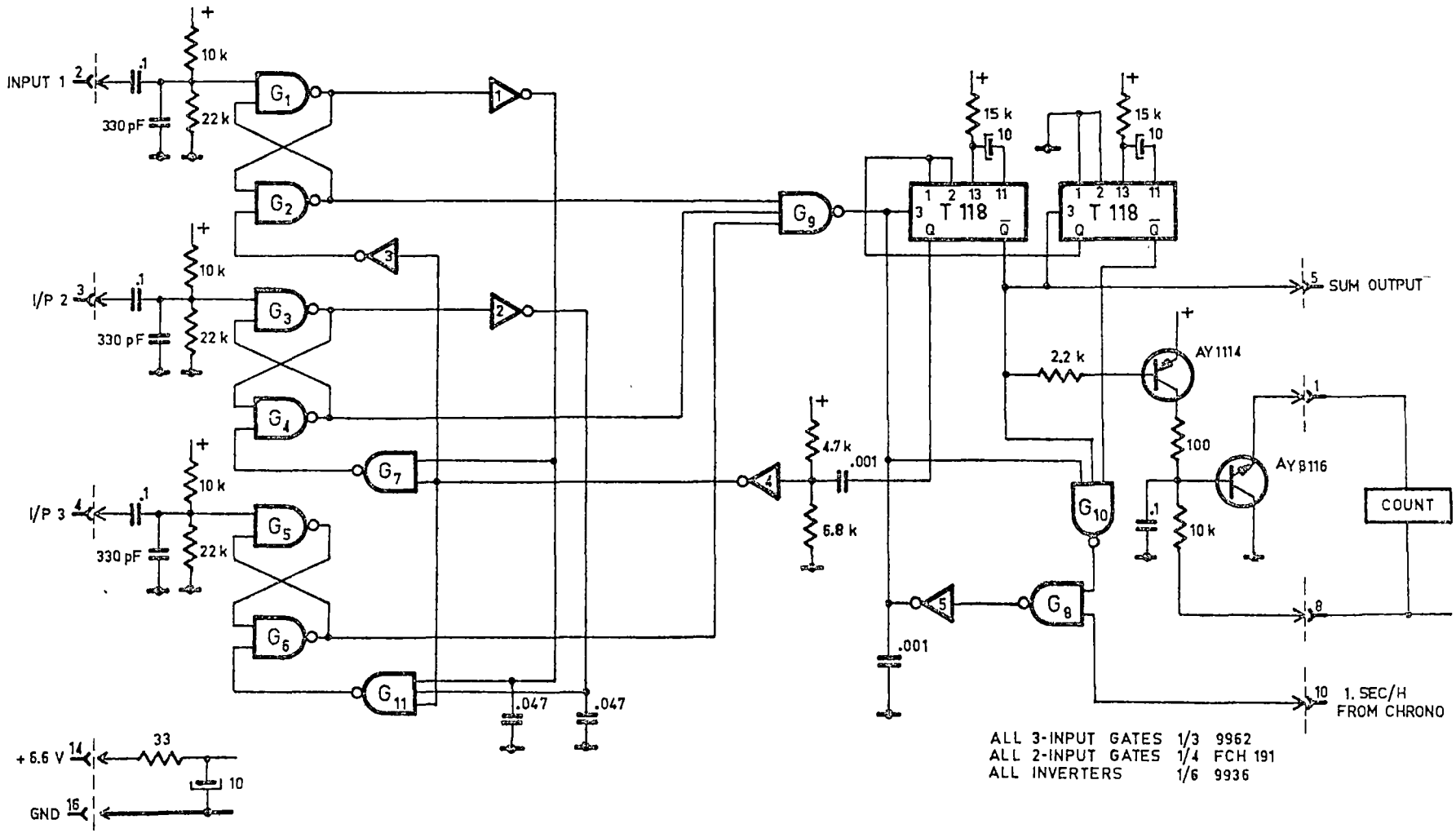

FIG.5-12. SODECO PRINTER DRIVER.

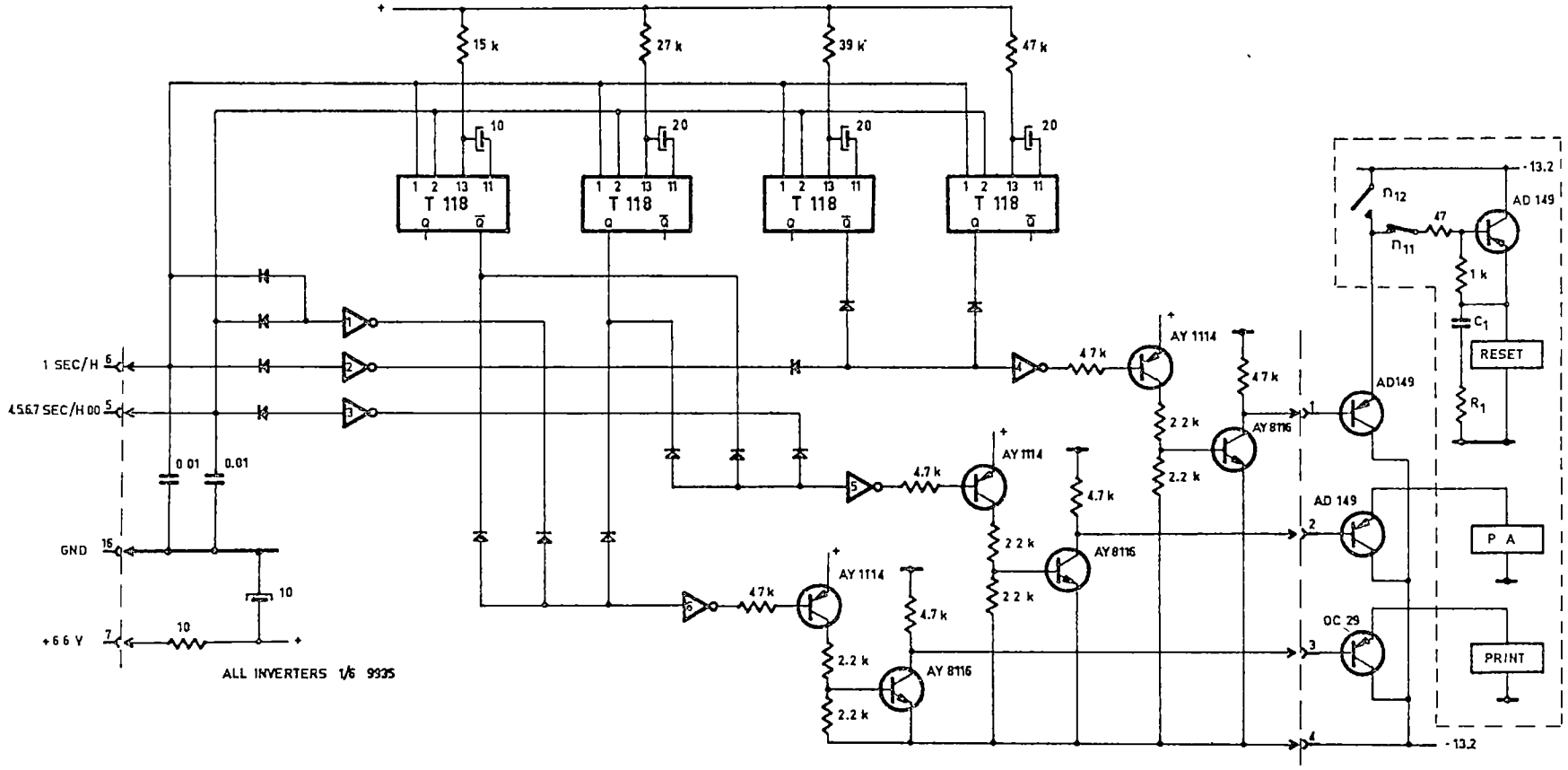

FIG 5-13 SODECO PRINTER CONTROL.

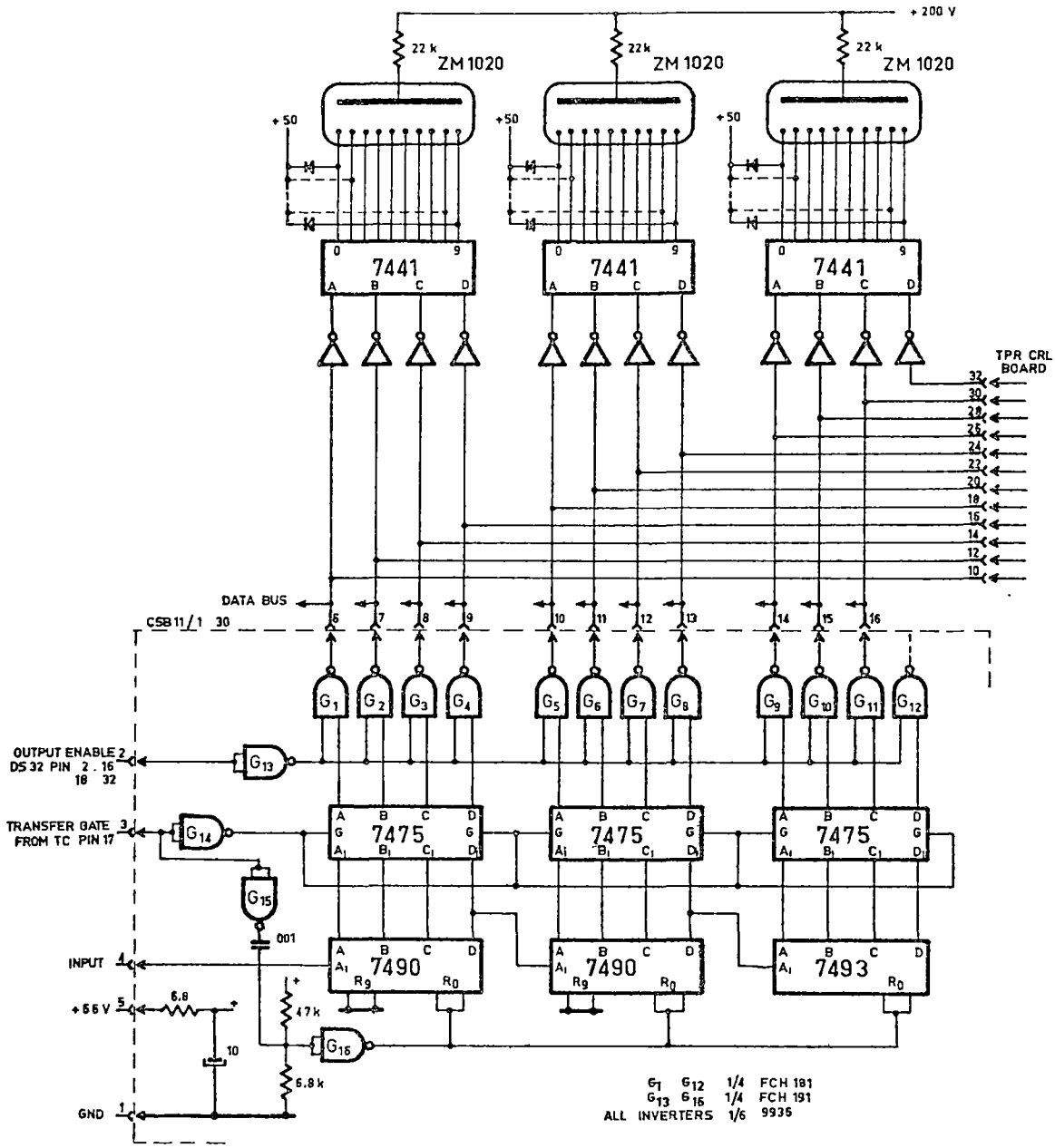

FIG 5-14 DATA REGISTER AND READ-OUT DISPLAY

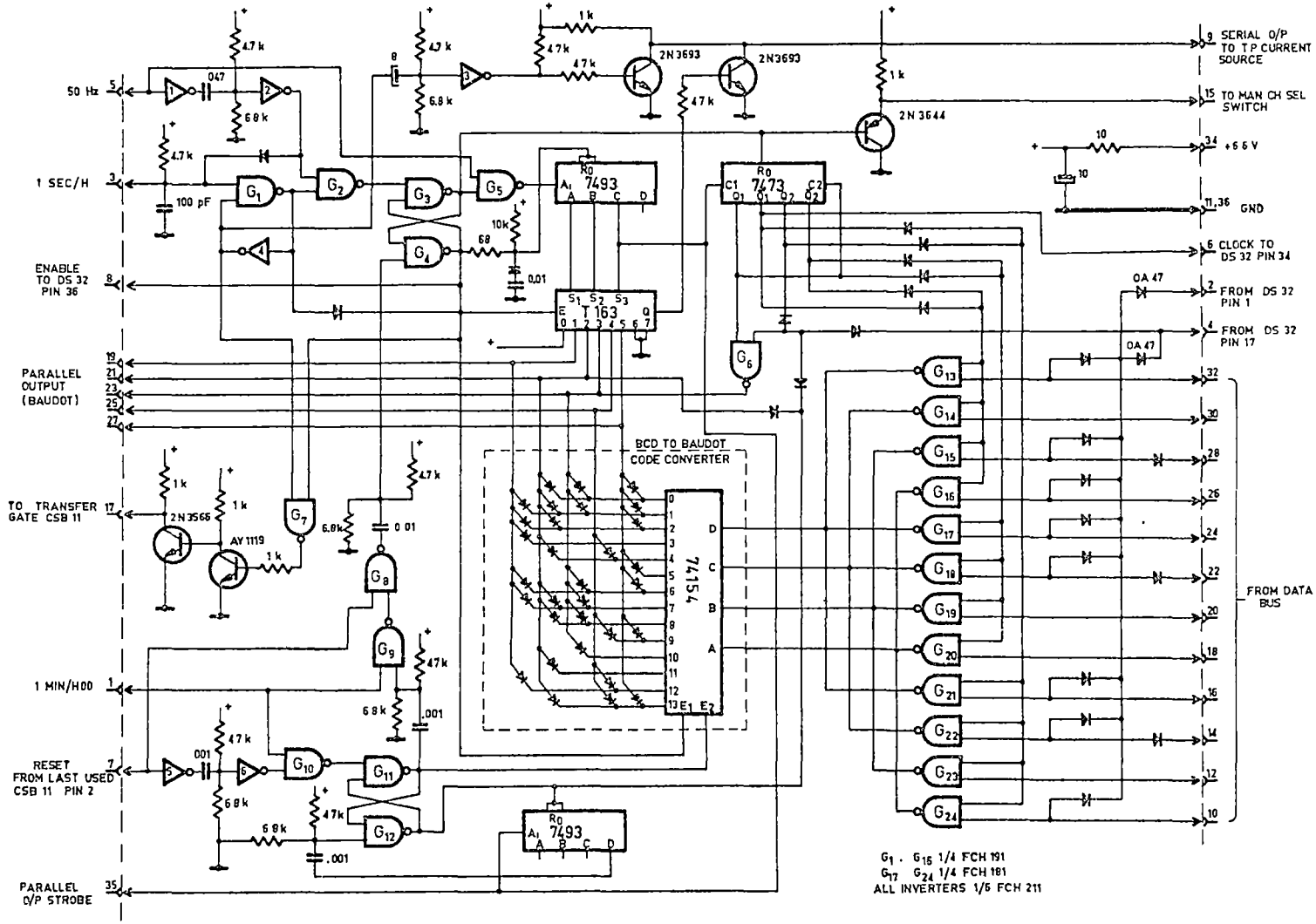

FIG 5-15 CODE CONVERTER AND TELEPRINTER CONTROL.

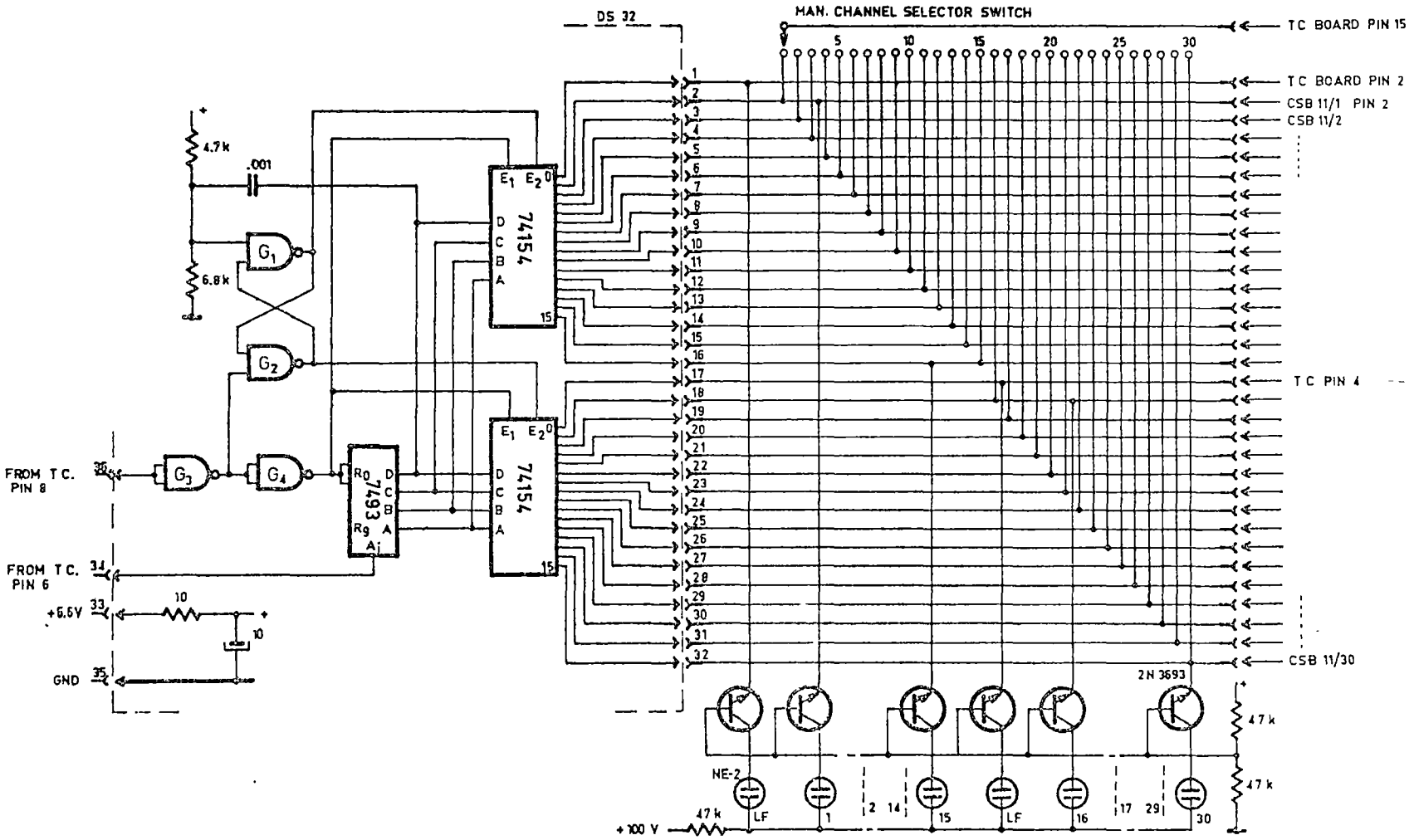

FIG. 5-16. DATA CHANNEL SELECTOR.

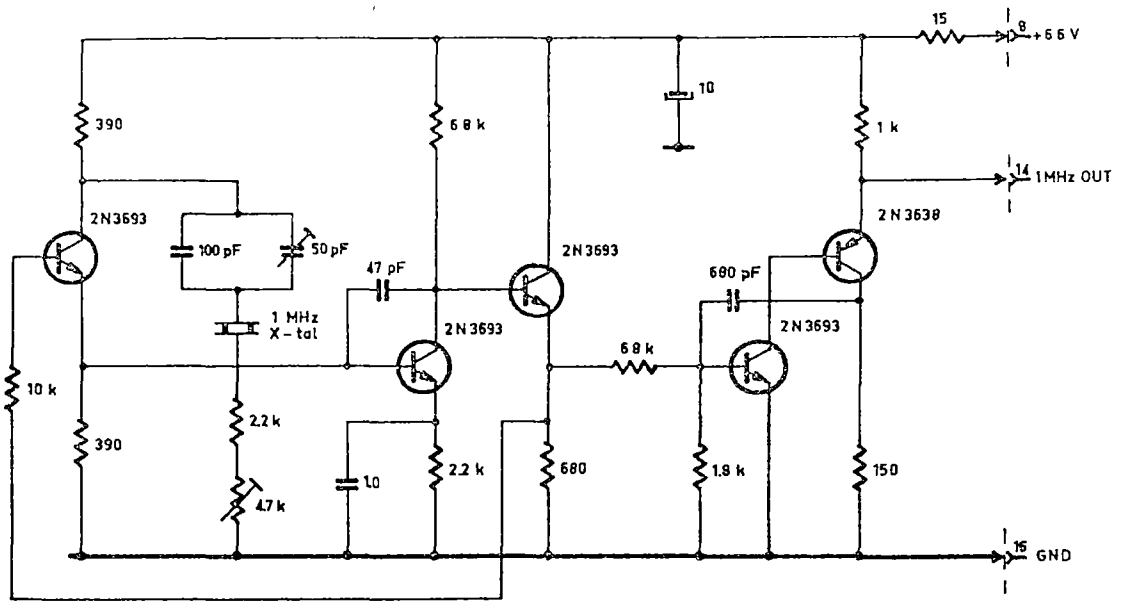

FIG.5-17 1 MHz X-TAL OSCILLATOR.

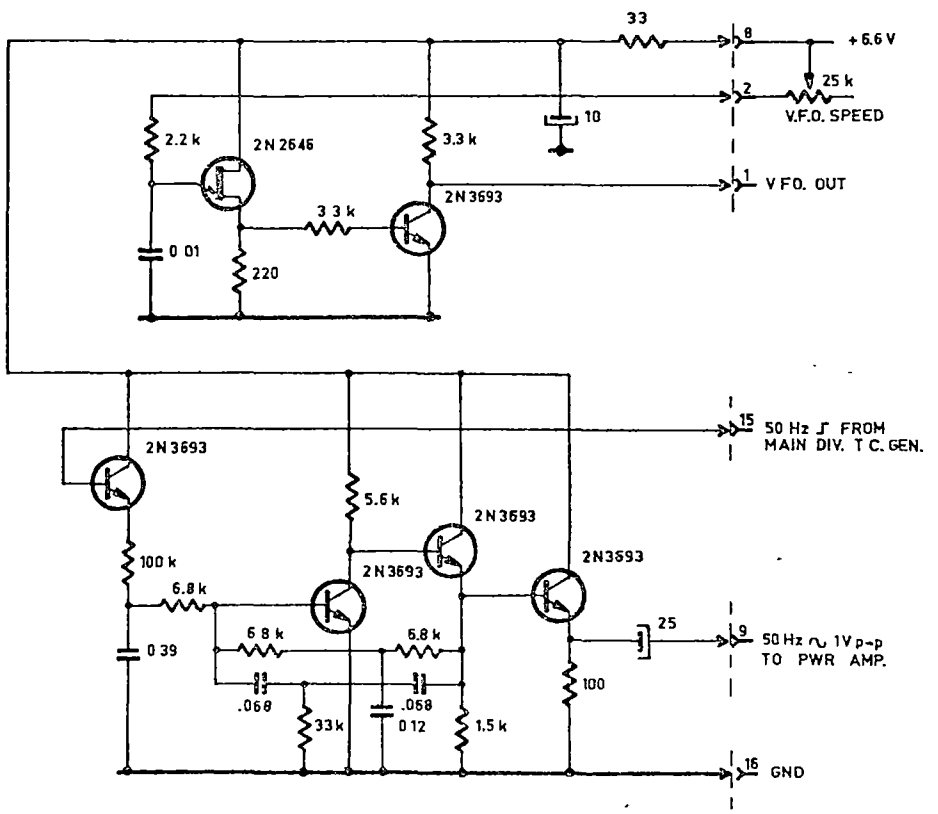

FIG 5-18 V FO. AND 50 Hz FILTER.

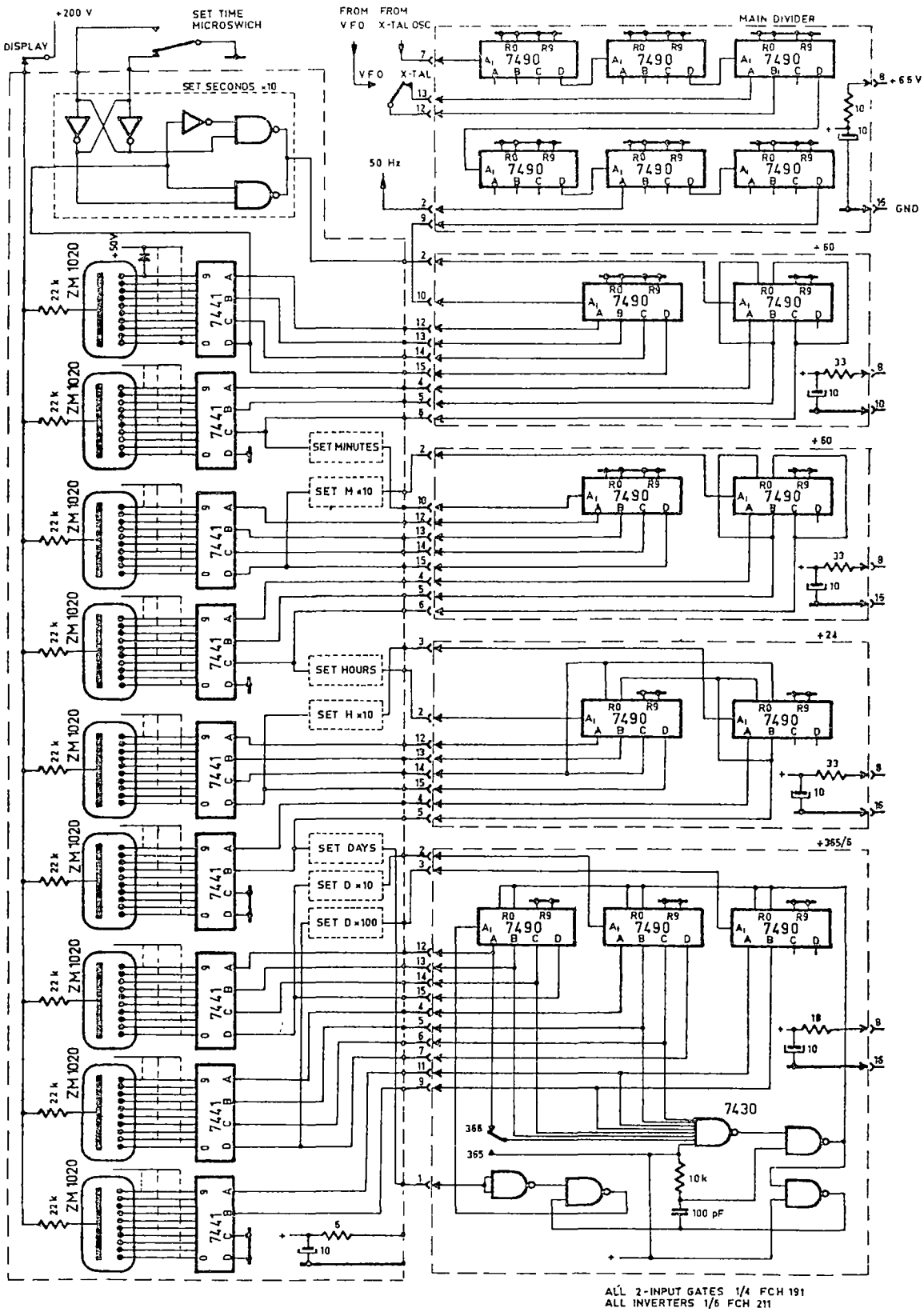

FIG 5-19 TIME CODE GENERATOR.

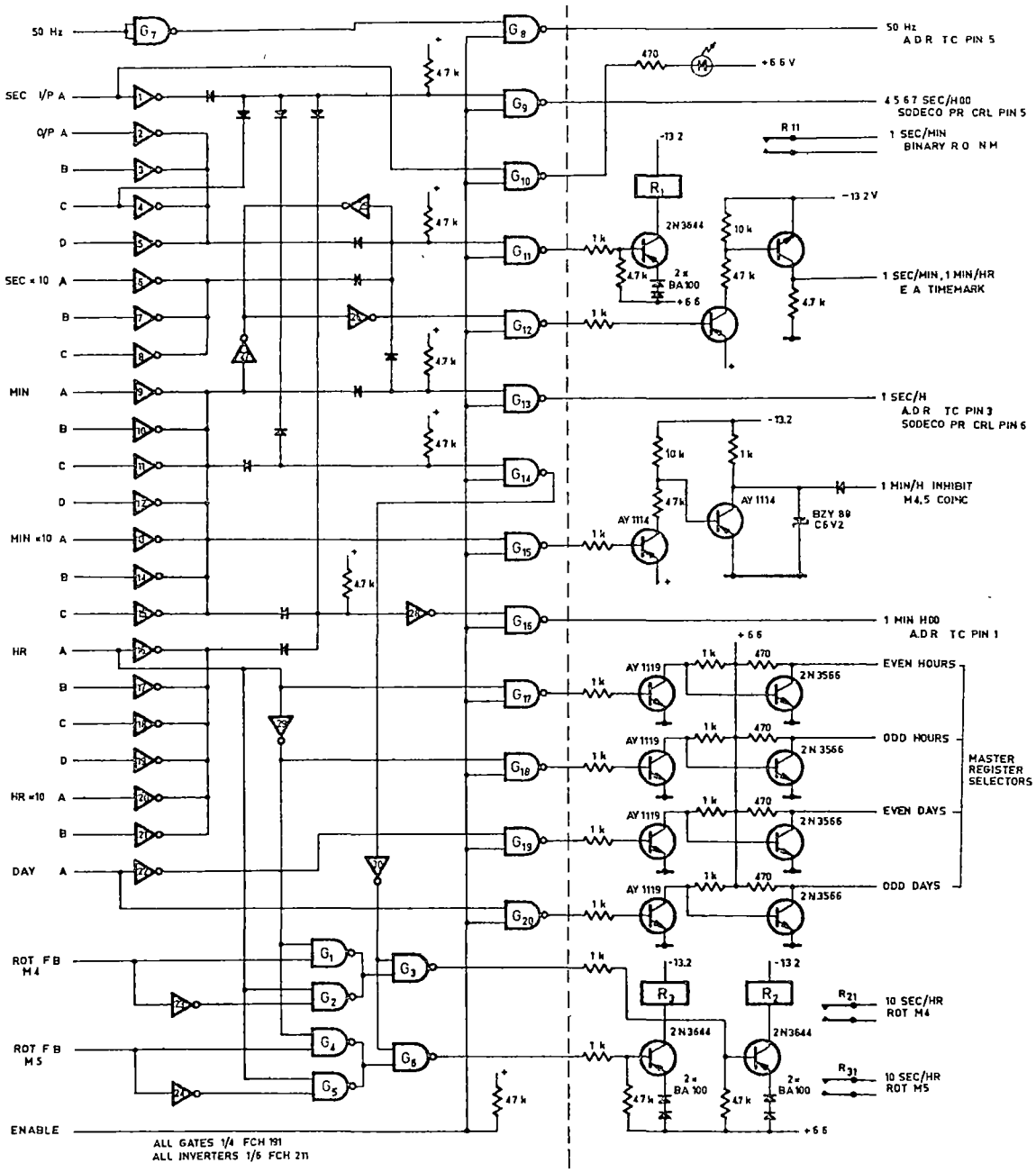

FIG 5-20 TIMEMARK DECODER

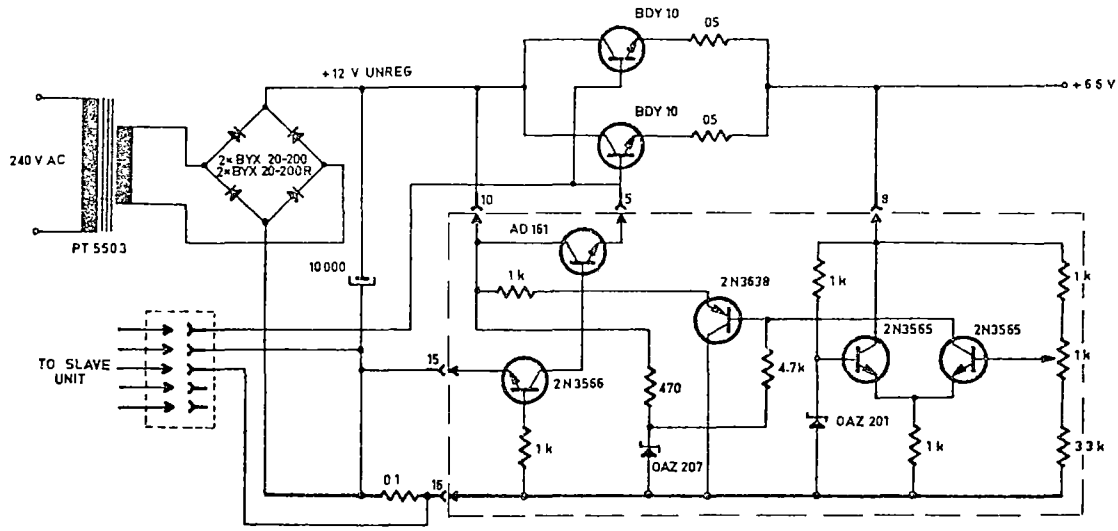

FIG 5-21 +6 V REGULATED POWER SUPPLY.

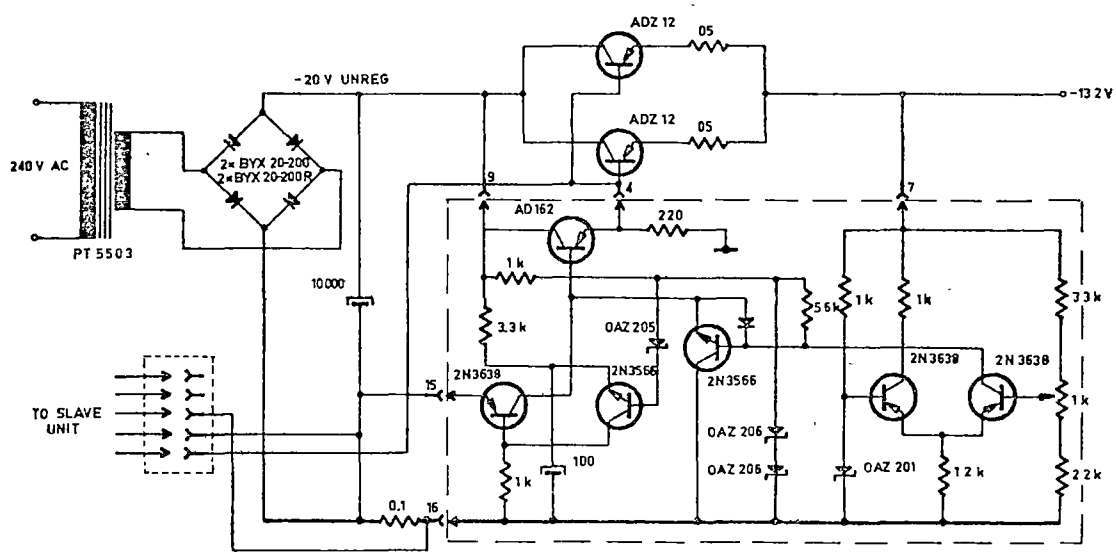

FIG 5-22. -12 V REGULATED POWER SUPPLY.

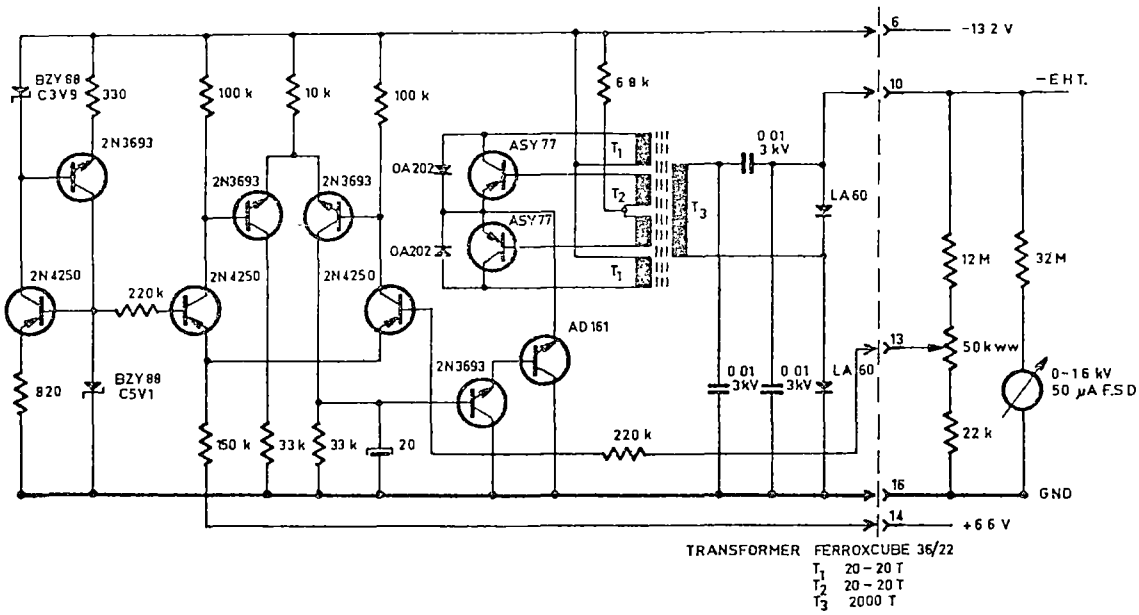

FIG 5-23 E HT SUPPLY

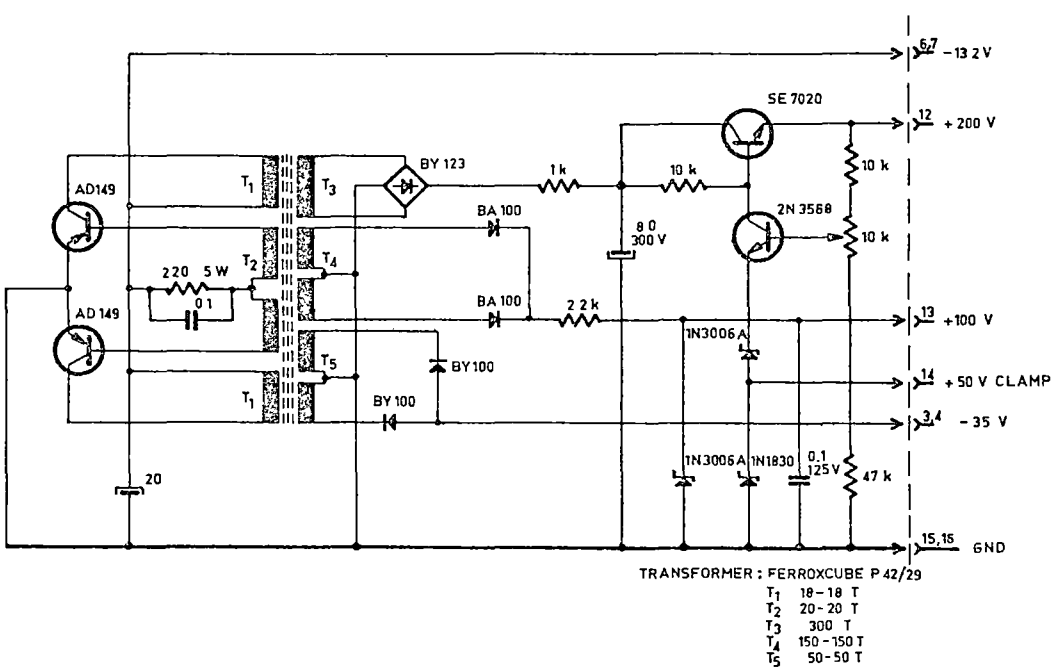

FIG 5-24 H T SUPPLY

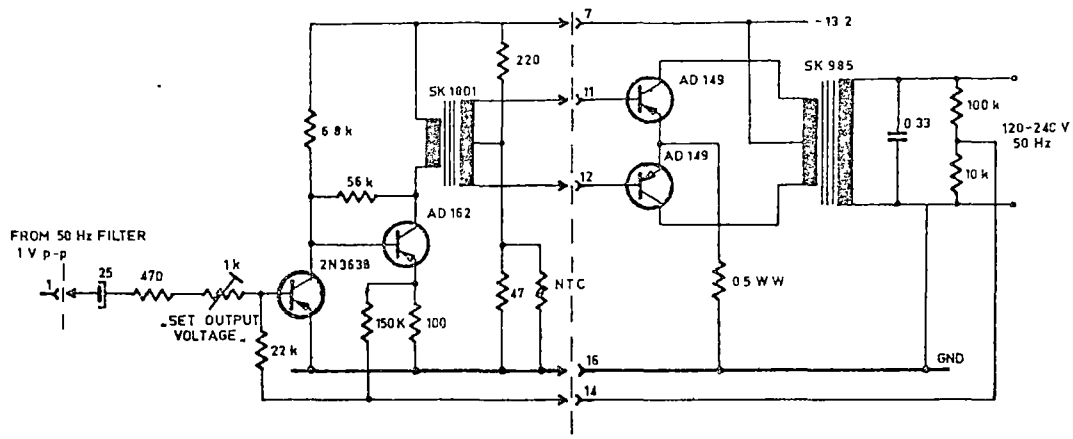

FIG 5-25. 50 Hz POWER AMPLIFIER

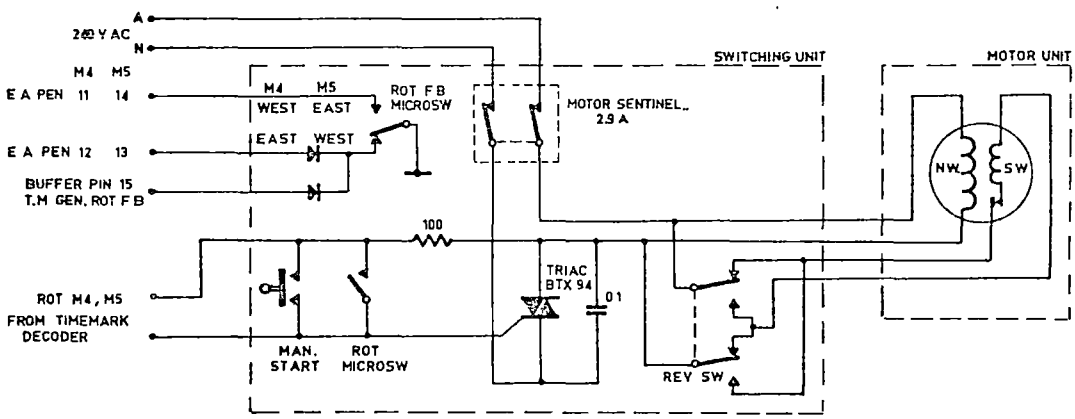

FIG. 5-26 TELESCOPE ROTATION SWITCHGEAR.

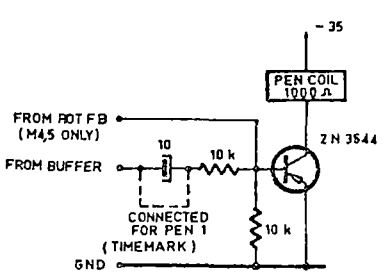

FIG 5-27 E A PEN DRIVER

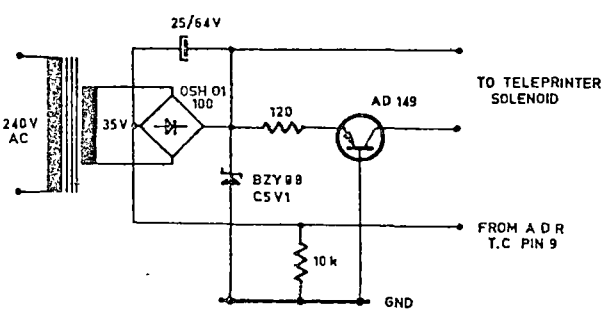

FIG 5-28 40 mA CURRENT SOURCE.

CHAPTER 6

STATISTICS OF COSMIC RAY OBSERVATIONS

6.1 Dispersion of Data

In the interpretation of cosmic ray data consideration has to be given to the statistical nature of particle counting. Fluctuations of the cosmic ray flux occur due to the random distribution of cosmic ray particles in space and time and obey the statistical law of random events. Superimposed on the random fluctuation one finds the systematic changes of the flux caused by various anisotropies and intensity changes caused by atmospheric, magnetic etc. influences. The relative magnitude of the random fluctuation of the measured intensity is a function of the count rate of the detector. To enable the detection of systematic changes of a given amplitude the cosmic ray detector must have a certain minimum count rate.

Because of the large number of samples and relatively low number of events in each interval the distribution of arrival of cosmic ray particles is a Poisson variable. The distribution is given by:

$$P(k,N\tau) = e^{-N\tau} \frac{(N\tau)^k}{k!} \qquad (6\text{-}1)$$

where $P(k,N\tau)$ is the probability of k events occuring during interval τ and N is the average count rate. (Feller, 1950).

In the case of the Poisson distribution the variance σ^2 equals the mean $\bar{N}$. The standard deviation σ is then given by

$$\sigma = \sqrt{\bar{N}} \qquad (6\text{-}2)$$

In the absence of systematic changes in the count rate it is expected that 68% of the observed values will be within $\pm\sigma$, 95% within $\pm 2\sigma$ and 99.7% within $\pm 3\sigma$ of the mean value $\bar{N}$.

Calculation of the standard deviation is important for the day to day test of detector efficiencies. Ratios of the daily count totals of similar detectors will contain no systematic changes of cosmic ray origin and will therefore give an indication of the detector's performance. By comparing the observed standard deviations of two telescopes A and B the expected standard deviation of the ratio of the daily means N_A/N_B will be

$$\sigma_{\text{ratio}A,B} = (N_A/N_B^2 + N_B/N_A^2)^{\frac{1}{2}} \qquad (6\text{-}3)$$

A consideration relating to the choice of scale factors follows from 6-2. To reduce wear and eliminate saturation of the electro-mechanical counters the coincidence pulses are scaled as described in chapter 5. The scale factor 2^n is selected so that the standard deviation σ of the scaled counts is >2, that is the content of the scaler at any time is less than the statistically expected fluctuation in the recording interval. Provided that no systematic errors are introduced due to the fractional content remaining in the scalers at the end of the recording interval, the data will not suffer in accuracy due to scaling.

6.2 Accidental Coincidences

A small portion of the observed count rate of the detector will be due to accidental coincidences unrelated to the passage of a single ionising particle through the three sets of counters connected in coincidence. Accidental coincidences occur through independent discharges of three counters in coincidence or through a two-fold coincidence occuring simultaneously with an independent discharge of the third counter. Independent discharges of counters are due to both

cosmic ray particles and local radioactive material e.g. radioactive isotopes in the glass counter wall.

In the knowledge of the mean count rate and the resolving time of the coincidence circuit the accidental coincidence rate can be estimated from equation 6-1 by putting k=1. For a very short resolving time τ the probability of one event occuring in τ is $N\tau$. The two-fold accidental coincidence rate will be then

$$\Delta N_2 = 2N_1N_2\tau \qquad (6\text{-}4)$$

where N_1 and N_2 are the number of pulses per second in the two group of counters in coincidence. For three-fold accidental coincidences of independent origin the rate is given by

$$\Delta N_3 = 3N_1N_2N_3\tau^2 \qquad (6\text{-}5)$$

From 6-4 the accidental rate had been estimated for the high zenith angle telescope. An average count rate of 25 p/sec for each counter pair and output pulse length of 2 μs gives an accidental count rate of 0.006 p/hour or 10^{-4}% of the total measured coincidence rate.

Accidental coincidences arising from genuine two-fold coincidences occuring simultaneously with an independent event in the third counter group have been calculated by Parsons (1957) for the standard cubical counter telescopes. Due to the reduced background counters now in use the accidental rates for the present telescopes M_4 and M_5 are considerably lower, e.g. about 0.4% of the total count rate.

The same consideration for the calculation of the three-fold

accidental rate involving genuine two-fold coincidences does not hold for the high zenith angle telescope. Because of the asymmetry of the geometry, accidental rates will be different for the two azimuth directions. The two-fold coincidence rates for trays A B and B C have not been measured. However they can be roughly estimated by considering the acceptance angle of the geometry. An upper limit of N and 2N is assumed for the two-fold coincidences between trays A B and trays B C respectively, where N is the observed three-fold coincidence rate. According to 6-4 the accidental coincidence rates are then 0.017% for the south azimuth and 0.008% for the north azimuth of the three-fold count rate.

6.3 Data Loss Due Recovery and Resolving Times

Immediately after discharge geiger counters will not respond to further ionising particles. The time taken for the recovery of the electrical field and dissipation of the ions collected at the anode is called the recovery time or dead time of the counter. Particles arriving during this time will not be recorded and therefore represent a loss of the number of particles counted. If the counter is unable to operate for C/τ second during one second, where C is the measured count rate and τ is the recovery time, the efficiency of the counter is given by

$$E_{\%} = e^{-C\tau}.100 \qquad (6\text{-}6)$$

For the counters in use at present (background $\sim$ 15 pps, $\tau \sim 300\mu s$) this will represent a loss of 0.45% of the total count rate.

Data loss due to the finite resolving time of the pulse shaping and coincidence circuits can be calculated likewise. C will be now

the recorded coincidence rate between counter trays. For a double pulse resolving time of 4 μs and the observed coincidence rates of detectors M1...M10 the loss is negligible.

No loss will occur in the scaling circuits at the maximum possible rate of coincidence pulses (250kHz).

To calculate the loss due to the resolving time (τ=100ms) of the electro-mechanical registers the probability of occurrence of $C > n$ number of pulses in interval τ has to be calculated where n is the scale factor of the scaling circuit. The formula derived by Blackman and Michiels (1948) based on the tabulated functions of Molina (1942) gives the efficiency as

$$E_{\%} = \left(1 - e^{-C\tau} \frac{(C\tau)^n}{n!}\right) 100 \qquad (6\text{-}7)$$

provided the condition $C\tau/n << 1$ is satisfied. Again, in the present case no observable efficiency loss will occur.

CONCLUSION

The design and construction of the high zenith angle telescope has been described. On the basis of the obtained results the performance of the telescopes is satisfactory and the data seem to be free of spurious effects. Discussion of the results of the first year of operation appears elsewhere (Jacklyn and Vrana, 1969). Unfortunately only limited results from the new observatory complex are available due to the long hold-up in computer processing.

Routine testing of counters by the present method is a time consuming operation due to the large number of geiger counters (over 1200) employed in the installation. It is planned to replace the routine of periodic manual counter test procedure by a sampling ratemeter which will continuously cycle the individual counter outputs. The presence of faulty counters in any of the detectors will be automatically indicated.

The yearly despatch and transport of replacement counters without damage is a recurring problem, therefore rejuvenation of the counters at Mawson would be desirable. Satisfactory cleaning and refilling of the counter envelopes at the station would require a modified counter envelope design.

A final comment is made regarding the temperature control of the observatory in summer; at the present the air cooling system for the interior of the observatory is at the limit of its thermal capacity in controlling summer overheating. It is proposed to paint the building exterior white to reduce heat absorption of the roof and walls.

APPENDIX

The diagrams contained in the following pages represent the asymptotic cone of acceptance of the telescopes M1 ... M10 for the momenta 18 GV, 25 GV, 50 GV, 100 GV, 300 GV and 1000 GV. (Cooke, 1970)

The drawings are perspective views of the asymptotic cones projected onto a sphere representing the earth. The equator, the position of Mawson (M) and the South Pole are indicated.

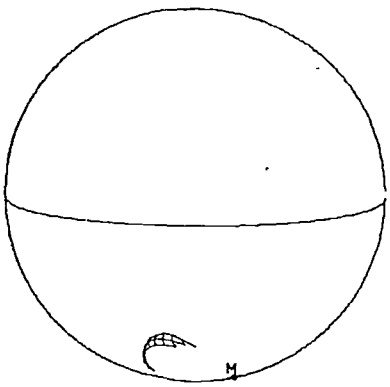

18 GV

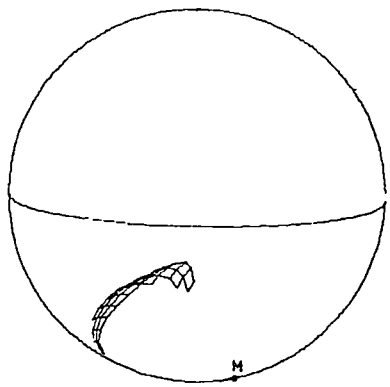

25 GV

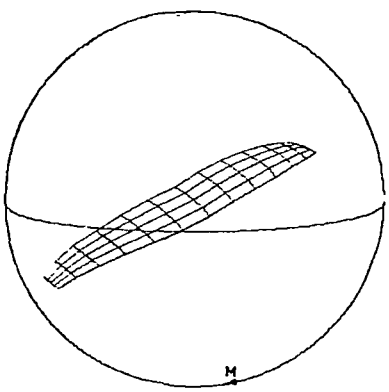

50 GV

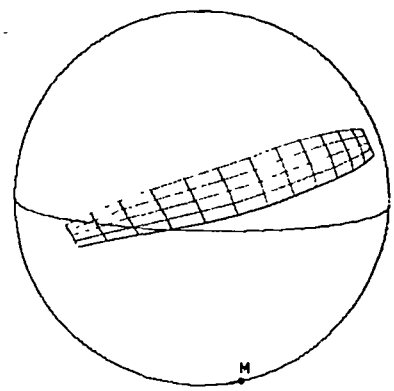

100 GV

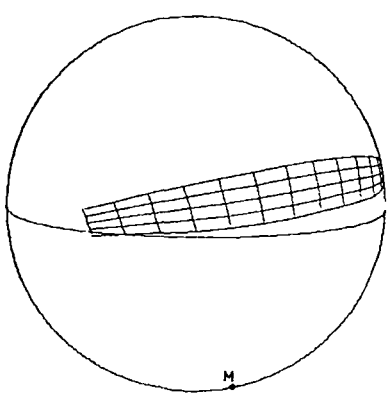

300 GV

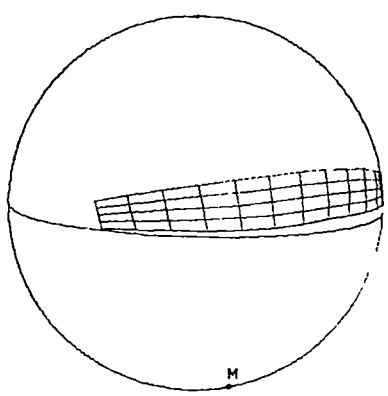

1000 GV

ASYMPTOTIC CONE OF ACCEPTANCE FOR TELESCOPES M1 ... M3
ZENITH ANGLE : 76,5° (NARROW ANGLE)
AZIMUTH : NORTH (0°)

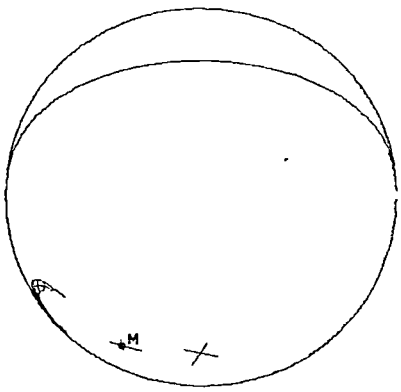

18 GV

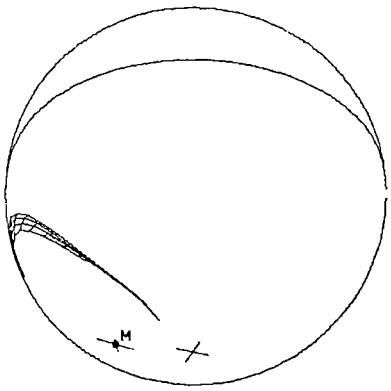

25 GV

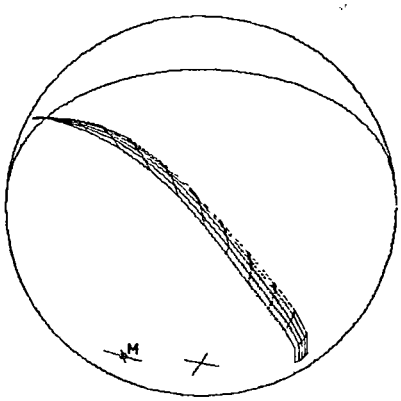

50 GV

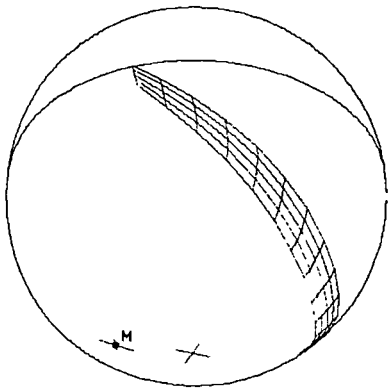

100 GV

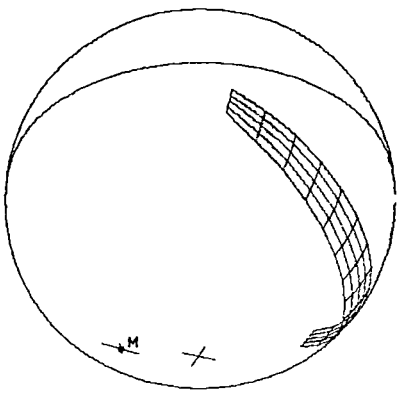

300 GV

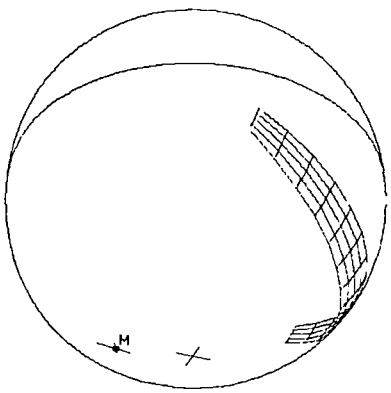

1000 GV

ASYMPTOTIC CONE OF ACCEPTANCE FOR TELESCOPES M1 ... M3
ZENITH ANGLE : 76.5° (NARROW ANGLE)
AZIMUTH : SOUTH (180°)

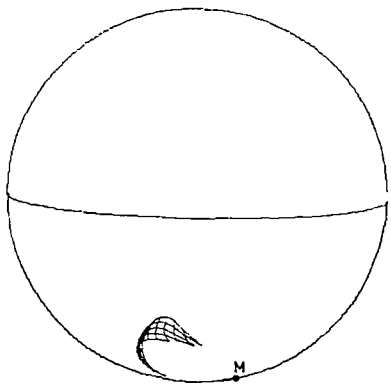

18 GV

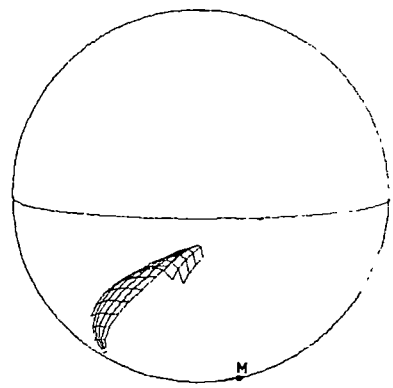

25 GV

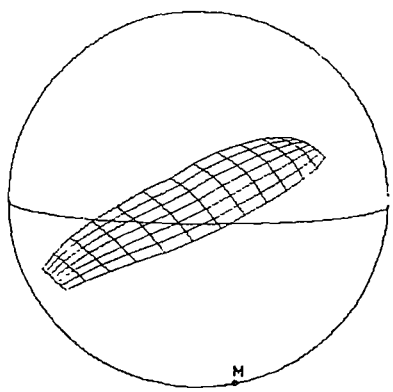

50 GV

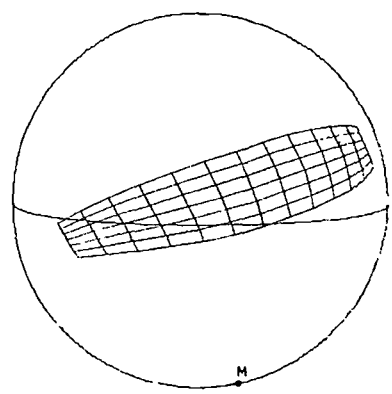

100 GV

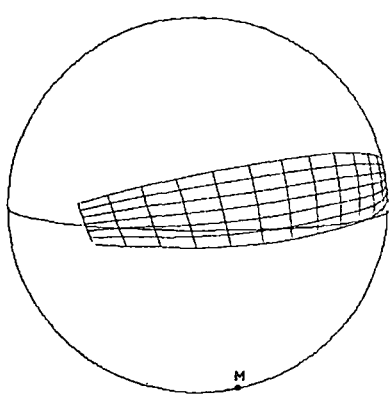

300 GV

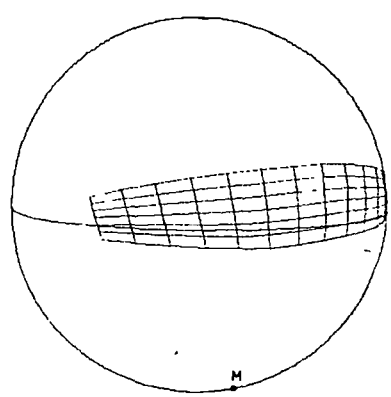

1000 GV

ASYMPTOTIC CONE OF ACCEPTANCE FOR TELESCOPES M1 ... M3
ZENITH ANGLE : 72° (WIDE ANGLE)
AZIMUTH : NORTH (0°)

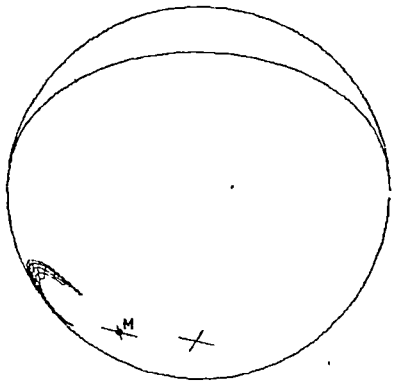

18 GV

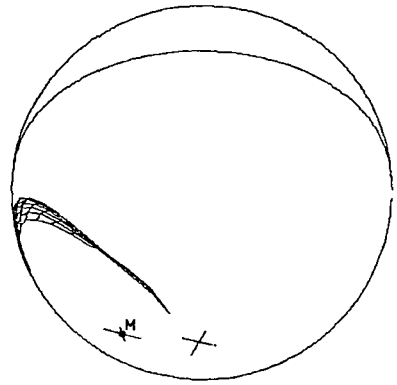

25 GV

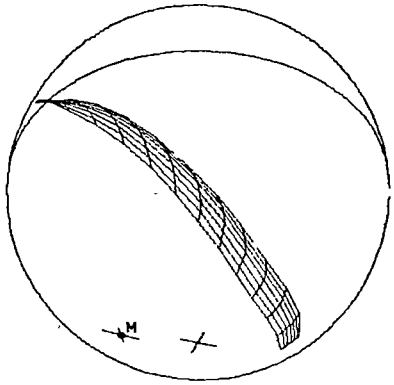

50 GV

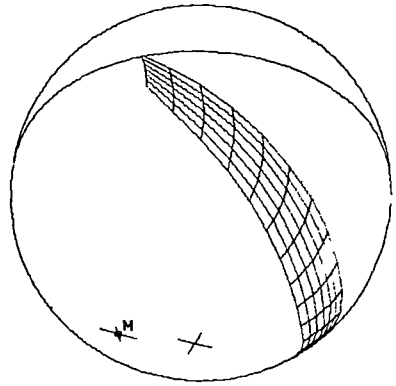

100 GV

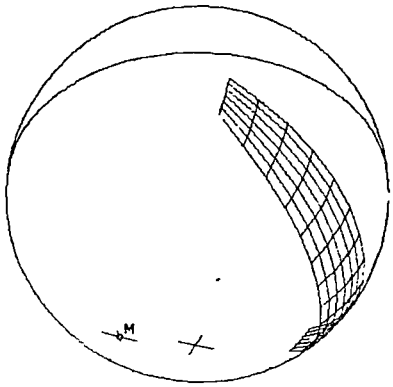

300 GV

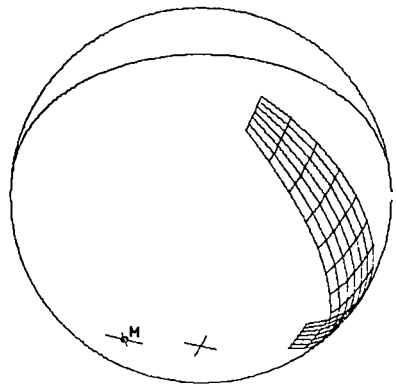

1000 GV

ASYMPTOTIC CONE OF ACCEPTANCE FOR TELESCOPES M1 ... M3
ZENITH ANGLE : 72° (WIDE ANGLE)
AZIMUTH : SOUTH (180°)

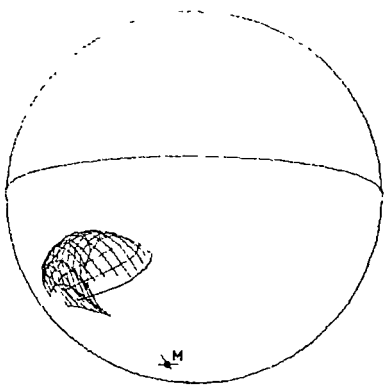

18 GV

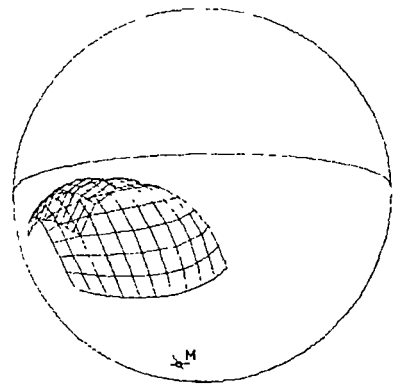

25 GV

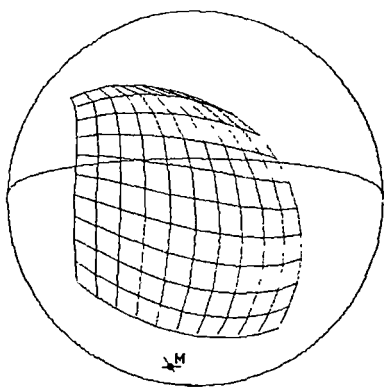

50 GV

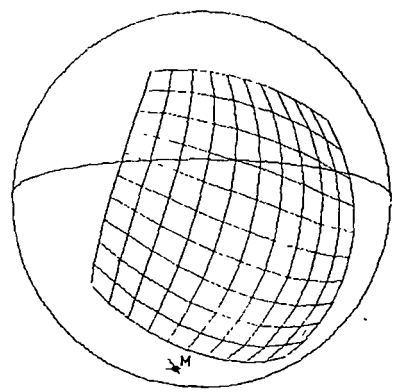

100 GV

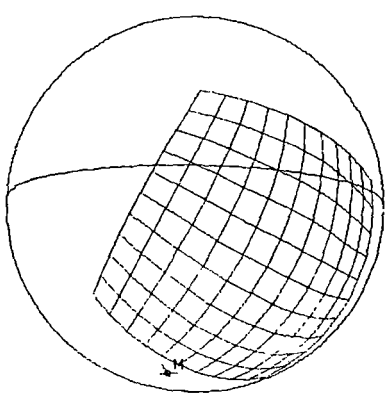

300 GV

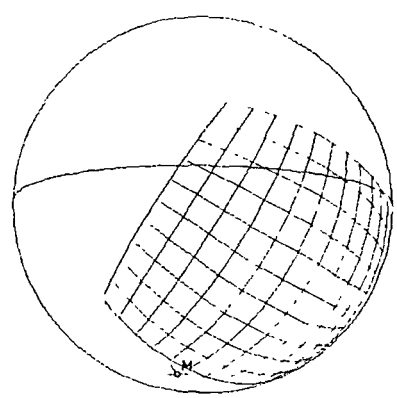

1000 GV

ASYMPTOTIC CONE OF ACCEPTANCE FOR TELESCOPES M4,M5
ZENITH ANGLE : 45°
AZIMUTH : GEOMAGNETIC EAST (60°)

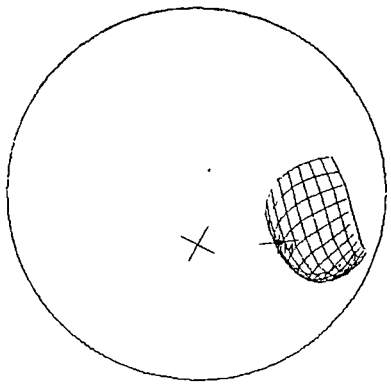

18 GV

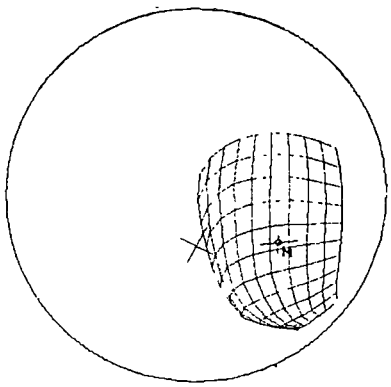

25 GV

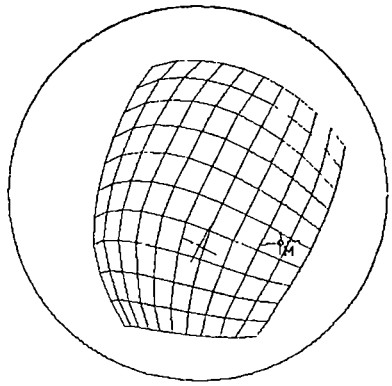

50 GV

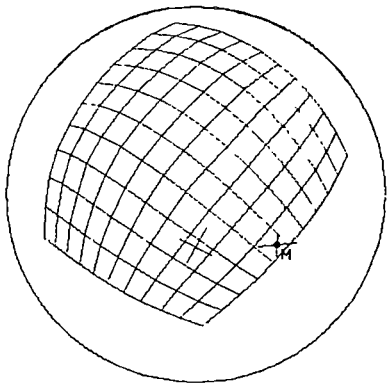

100 GV

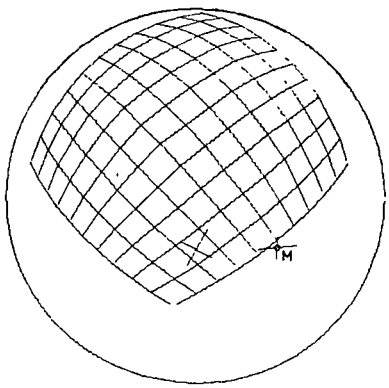

300 GV

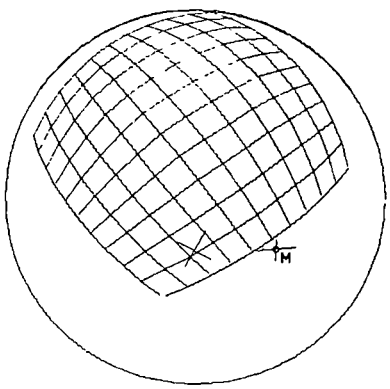

1000 GV

ASYMPTOTIC CONE OF ACCEPTANCE FOR TELESCOPES M4,M5
ZENITH ANGLE : 45°
AZIMUTH : GEOMAGNETIC WEST (240°)

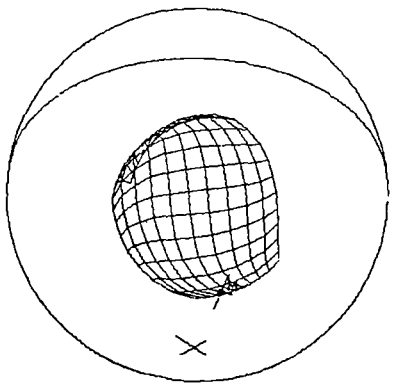

18 GV

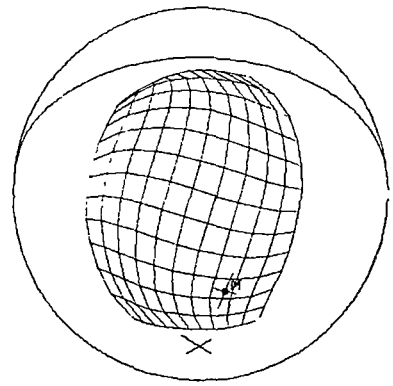

25 GV

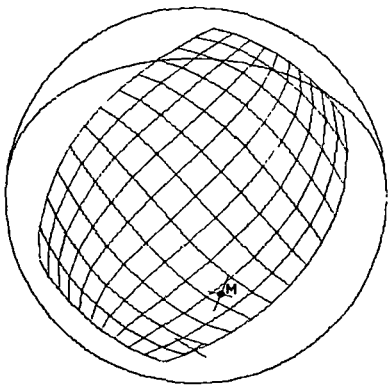

50 GV

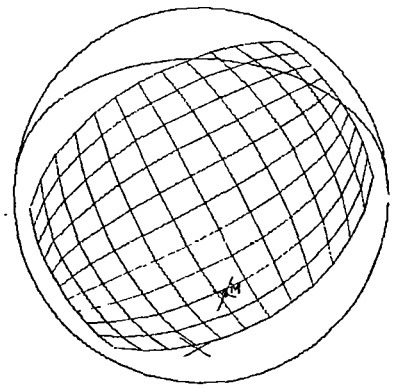

100 GV

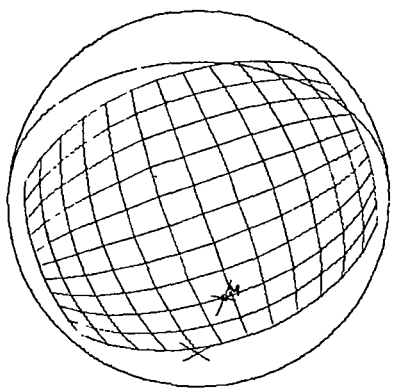

300 GV

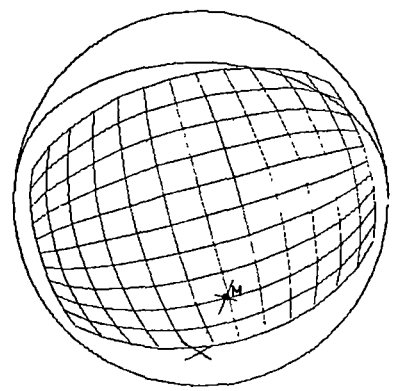

1000 GV

ASYMPTOTIC CONE OF ACCEPTANCE FOR TELESCOPES M6 ... M8
ZENITH ANGLE : 24° (NARROW ANGLE)
AZIMUTH : GEOMAGNETIC NORTH (330°)

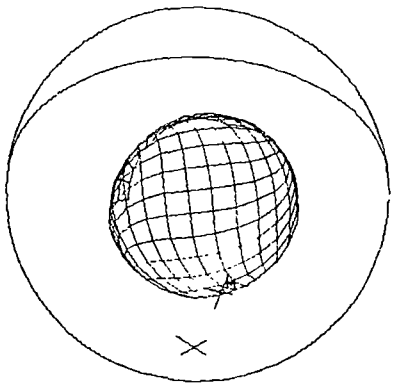

18 GV

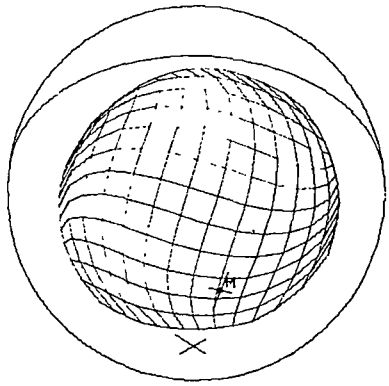

25 GV

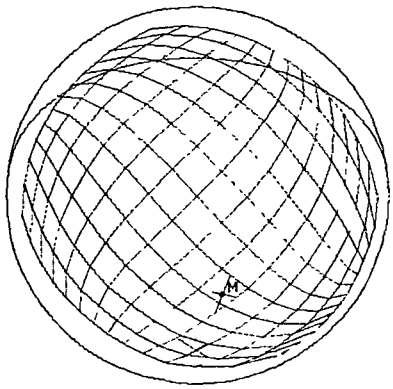

50 GV

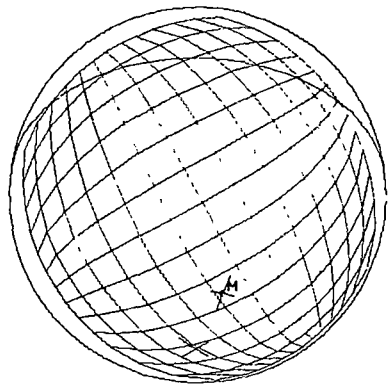

100 GV

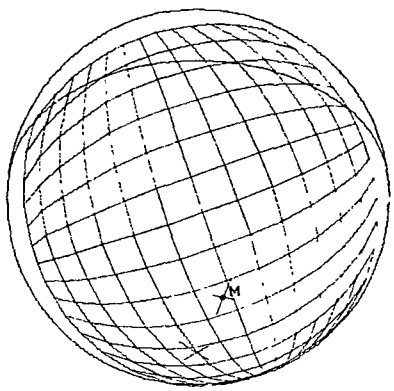

300 GV

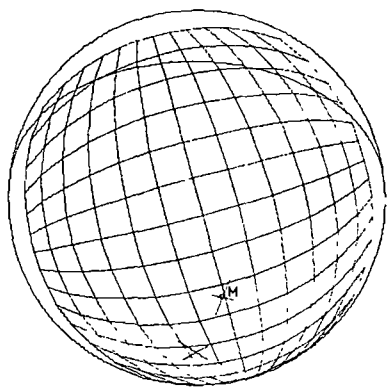

1000 GV

ASYMPTOTIC CONE OF ACCEPTANCE FOR TELESCOPES M6... M8
ZENITH ANGLE : 24° (WIDE ANGLE)
AZIMUTH : GEOMAGNETIC NORTH (330°)

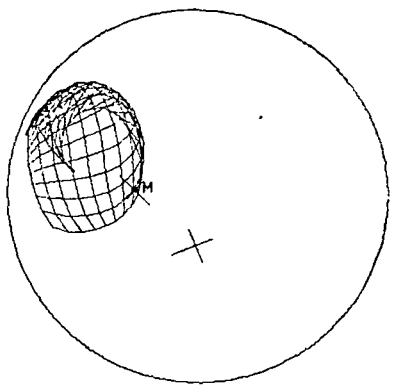

18 GV

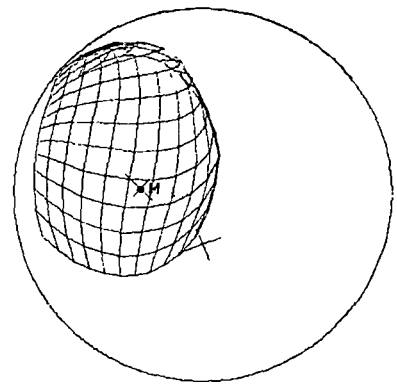

25 GV

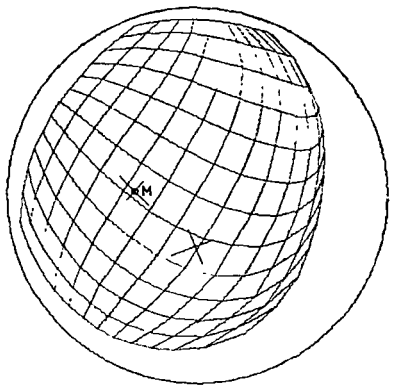

50 GV

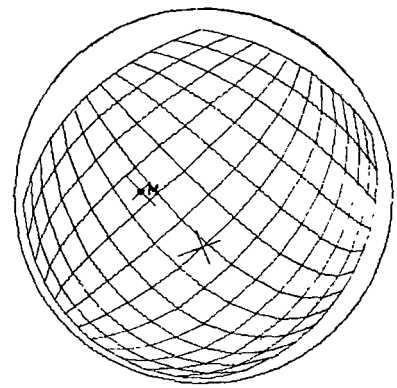

100 GV

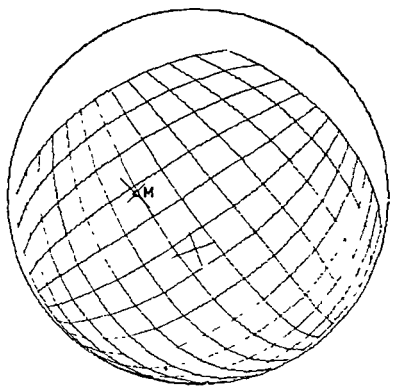

300 GV

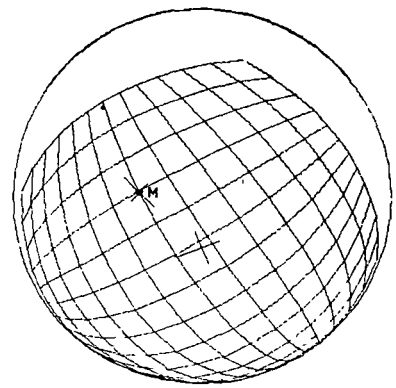

1000 GV

ASYMPTOTIC CONE OF ACCEPTANCE FOR TELESCOPES M9,M10
ZENITH ANGLE : 30°
AZIMUTH : SSW (200°)

REFERENCES

BASSI,P., CLARK,G. and ROSSI,B. (1953) Phys. Rev., 92, 441.

BLACKMAN,M. and MICHIELS,J.L. (1948) Proc. Phys. Soc., 60, 549.

CINI-CASTAGNOLI,D. (1973) Proc. 13th Int. Cosmic Ray Conf., Denver, 5, 3706.

CINI-CASTAGNOLI,D. and DODERO,M.A. (1975) Proc. 14th Int. Cosmic Ray Conf., Munich, 4, 1460.

COMPTON, A.H. and GETTING,I.A. (1935) Phys. Rev. 47, 817.

CONFORTO,A.M. and SIMPSON,J.A. (1957) Nuovo Cimento 6, 1052.

COOKE,D.J. (1971) PhD. Thesis, University of Tasmania.

DAVIS,L. (1954) Phys. Rev. 96, 743.

DUPERIER,A. (1949) Proc. Phys. Soc. (A) 62, 684.

ELLIOTT,H. and DOLBEAR,D.W.N. (1951) J.Atmos. Terr. Phys. 27, 349.

FARLEY,F.J.M. and STOREY,J.R. (1954) Proc. Phys. Soc. (A) 67, 996.

FELLER,W. (1950) "An Introduction to Probability Theory and Its Applications" Vol.1 (Wiley International Edition).

FENTON,A.G. and FENTON,K.B. (1975) Proc. 14th Int. Cosmic Ray Conf., Munich, 4, 1482.

FORMAN,M.A. and GLEESON,L.G. (1970) Preprint.

HUMBLE,J.E., FENTON,A.G., SPELLER,R.D., OTAOLA,J.A., THAMBYAHPILLAI,T., DUTT,J.C., MATHEWS,T., MIYAZAKI,T. and PEACOCK,D.S., Proc. 13th Int. Cosmic Ray Conf., Denver, 2, 976.

JACKLYN,R.M. (1962) Nuovo Cimento, 24, 1034.

JACKLYN,R.M. (1965) Nuovo Cimento 37, 1135.

JACKLYN,R.M. (1966) Nature 211, 690.

JACKLYN,R.M. (1969) Nature 223, 601.

JACKLYN,R.M. and VRANA,A. (1969) Proc. A.S.A. 1 (6), 278.

JACKLYN,R.M. (1970) ANARE Sci. Rep. Series C(11) Cosmic Rays Pub. No.114.

KASHA,H., HAWKINS,C.B.J. and STEFANSKI,R.J. (1967) Can. J. Phys. 46, 5306.

KASTEN,R.R. (1962) PhD. Thesis, University of Missouri.

KRAYBILL,H.L. (1954) Phys. Rev. 93, 1362.

MAEDA,K. (1964) J. Geophys. Res. 69, 1725.

McCRACKEN,K.G., RAO,U.R. and BUKATA,R.P. (1968) Can. J. Phys. 46, S844.

NAGASHIMA,K. (1971) Rep. Ion. Space Res. Japan 25, 189.

NAGASHIMA,K., UENO,H., FUJIMOTO,K., FUJII,Z. and KONDO,I. (1972) Rep. Ion. Space Res. Japan 26, 31.

NAGASHIMA,K., UENO,H. (1971) Rep. Ion. Space Res. Japan 25, 212.

NASH,W.F. and JUDGE,R.J.R. (1965) Nuovo Cimento 35, 999.

PARKER,E.N. (1964) Plan. Space Sci. 12, 735.

PARKER,E.N. (1958) Phys. Rev. 110, 1445.

PARSONS,N.R. (1957) ANARE Interim Reports No.17.

PARSONS,N.R. (1959) PhD. Thesis, University of Tasmania.

RAO,U.R., ANATH,A.G. and AGRAWAL,S.P. (1972) Plan. Space Sci. 20, 1799.

ROSSI,B. (1952) "High Energy Particles" (Prentice Hall : New York).

SANDSTRÖM,A.E. (1965) "Cosmic Ray Physics" (North Holland Pub. Co. : Amsterdam).

SARABHAI,V., PAI,G.L. and WADA,M. (1965) Nature 206, 703.

SWINSON,D. (1969) J. Geophys. Res. 74, 5591.

SWINSON,D. (1971) Proc. 12th Int. Cosmic Ray Conf., Hobart, 1, 284.

SWINSON,D. (1971) J. Geophys. Res. 76, 4217.

VAN ALLEN,J.A. Proc. 13th Int. Cosmic Ray Conf., Denver, 2, 750.

WADA,M. (1960) Sci. Papers. I.P.C.R. 54, 335.

WHITTACKER, E.T. and ROBINSON,G. (1944) "The Calculus of Observations" (Blackie : Glasgow)

WINCKLER,J.R. and STROUD,W.G. (1949) Phys. Rev. 76, 1012.